BRIDGE DAMAGE DETECTION UNDER TRAFFIC LOADING AND ENVIRONMENTAL VARIABILITY USING MACHINE LEARNING

A MASTER'S THESIS

BY

SARDORBEK A. NIYOZOV

MASTER OF SCIENCE
IN CIVIL ENGINEERING

STRUCTURES AND INFRASTRUCTURES

March 2022

BRIDGE DAMAGE DETECTION UNDER TRAFFIC LOADING AND ENVIRONMENTAL VARIABILITY USING MACHINE LEARNING

A MASTER'S THESIS

Presented

by

Sardorbek A. Niyozov

Supervised by:

Prof. DOMANESCHI MARCO

And

Prof. CASAS RIUS JUAN RAMON

DEDICATION

I dedicate this thesis to my family and friends. Their continued support and love made this work possible.

ACKNOWLEDGMENTS

Foremost, I would like to express my deepest gratitude to both of my supervisors Dr. Marco Domaneschi and Dr. Joan Ramon Casas Rius for the continuous support of my master's thesis and research, for their patience, motivation, enthusiasm, and immense knowledge. Their guidance helped me in all the time of research and writing this thesis.

Besides my supervisors, I would like to thank Fernando Josue Tenelema Muñoz, master's degree graduate of Universitat Politècnica De Catalunya onia-BarcelonaTech, for sharing his experience and knowledge, and assisting in the technical part of the research work. I really appreciated his kindness and goodwill.

Furthermore, I would like to thank Politecnico di Torino for giving me an opportunity to work on my master's thesis abroad. And I would also like to express my acknowledgement to Universitat Politècnica De Catalunya for their help during my work.

Last but not the least, I would like to express my gratitude and respect to all the teachers and lecturers at Politecnico di Torino.

ABSTRACT

BRIDGE DAMAGE DETECTION UNDER TRAFFIC LOADING AND ENVIRONMENTAL VARIABILITY USING MACHINE LEARNING

MARCH 2022

SARDORBEK ABBOS ÖĞLI NIYOZOV, B. Sc, POLITECNICO DI TORINO

M. Sc., POLITECNICO DI TORINO

Supervised by: Prof. DOMANESCHI MARCO and Prof. CASAS RIUS JUAN RAMON

Bridges are vital components of the civil infrastructure. They must continue to operate safely and reliably. And the traditional methods of assessing the health of structures are based on the idea that a change in the structure's dynamic response might indicate possible structural damage. However, in the case of bridges, operational (traffic load effects) and environmental (temperature and humidity) variability can both contribute to these changes. Indeed, this makes damage detection more difficult since the bridge might remain safe while still experiencing changes in the dynamic response if the impacts of traffic and the environment are not appropriately removed from the dynamic response. As a result, a false positive alert would be set off.

This thesis proposes and tests a methodology for detecting and localizing damage in bridges under traffic loads and environmental variability. Due to the difficulty in obtaining real data on undamaged and later damaged bridges that are simultaneously influenced by traffic and temperature changes, the proposed method is validated using an original numerical benchmark bridge developed as part of COST Action TU1402 on Quantifying the Value of Information, and it is updated to better simulate a real bridge. A two-span reinforced concrete girder bridge with different damage scenarios serves as the benchmark model. The vertical acceleration response is derived from a time-history study of the numerical bridge subjected to moving load, which is performed using open-source Python code accessible on the GitHub platform.

The state of the bridge is determined by evaluating the accelerations recorded by sensors at different ambient temperatures. Due to the non-transient nature of recorded data, the Fast Fourier Transform (FFT) is not applicable. Instead, one of the more modern approaches, such as Vibrational Mode Decomposition (VMD) is used to decompose the signal into Intrinsic Mode Functions (IMF). The Hilbert Transform is then used to extract instantaneous frequencies, which in this case represent the damage-sensitive features.

Furthermore, the environmental effects were removed from damage-sensitive features using Principal Component Analysis (PCA). It is a method for reducing the dimensionality of datasets while preserving interpretability and avoiding data loss.

Finally, the damage is detected and localized using clustering technique (K-means Machine Learning (ML) algorithm). Using symbolic objects to reduce the amount of data a technique of moving the time window, it is applied to damage-sensitive features.

The suggested approach is efficient and accurate in identifying and finding damage under transient vibrational loads in different temperature conditions, according to the results. The accuracy of these damage detection technologies supports their use in structural health monitoring of more complex and real structures.

Keywords: Structural Health Monitoring (SHM), Bridge damage identification, Numerical benchmark, Hilbert Huang Transform (HHT), Vibrational Mode Decomposition (VMD), Principal Component Analysis (PCA), Operational and Environmental Variability (OEV), Clustering algorithm, Machine Learning (ML), Unsupervised Learning, K-means.

TABLE OF CONTENTS

LIST OF TABLES

Table Page

LIST OF FIGURES

Figure Page

1. INTRODUCTION

1.1 Introduction

Civil infrastructures play an important role in countries social-economic life. Development of the cities, well-being of businesses and the safety of human lives depends on the state of the heath of the civil infrastructures. For example, bridges serve millions of people on the span on their lifetime. As a result, given the importance of bridges in our society, their condition evaluation is an important topic to research. To assure the building of safer and more lasting bridges, a well-designed bridge management system is necessary, with the understanding that their health condition is altered from its design as soon as they are put into operation.

The structural performance of a bridge is dictated by several factors: on the age of construction, level of deterioration (involving fatigue, structural deficiencies, and corrosion) and in-service loading. The collapse of a bridges can be result of natural or manmade hazards, i.e., in earthquakes, mud slides, floods, and accidents, and some other construction site related errors, such as early removal of support structures [1]. However, most of the bridges fail while in-service, and during their normal operational settings.

Figure 1.1 *Bridge failures, from left to right: Pittsburgh Bridge [2], and Nanfang'ao Bridge [3]*

Figure 1.1 shows an example of the brigde failures. On January 28, 2022, Pittsburgh Bridge collapsed hours before President Biden infrastructure visit to the city. 10 people were injured, 7 vehicles were stranded inlcuding a Port Authority bus, on the wrecked structure that spans a ravine in Frick Park [4]. Fortunately, there were no fatalities. The 52-year-old steel rigid frame bridge was consistently determined to be in poor condition during inspections from 2011 to 2017 and was repaired with estimated costing $1.5 million. However, according to a state-wide study, the bridge was last examined in September 2021 and was still found in a bad condition [4].

Furthermore, Nanfang'ao Bridge is an example of inspection and maintenance failures. The 20-year-old single-arch steel bridge in Taiwan, collapsed in October 2019, injuring 12 people, and killing six. Even though the reason for the failure is yet unknown, Sung Yuchi, dean of the Taipei Technology College of Engineering, believes corrosion in the bridge's suspension cables might be a cause. According to the New Civil Engineer magazine [5], Simon Bourne, proactive maintenance could have been essential to prevent cables from corrosion, wear, and strain. Such maintenance is preferable to reactive maintenance since it emphasizes preserving rather than merely repairing the entire bridge and its components, extending the bridge's lifespan. According to the Taiwan International Ports Corporation (TIPC) in charge of bridge maintenance, the standard yearly inspection went well, and the cables cords were examined as documented in the 2016 report. The bridge, however, collapsed one year before the next inspection, which was slated for 2020, raising doubts on the efficiency of its repair work. As a result, the Taiwanese government has calculated that the cost of replacing the bridge will be around $17 million.

Figure 1.2 *Morandi Genoa Bridge failure*

Finally, Morandi Genoa Bridge is an example of extreme catastrophic event. (**Figure 1.2**) On August 14, 2018, the fall of a large section of the 51-year-old bridge killed 43 people. The bridge was one of the busiest highways in Europe as a part of European route E80 linking Italian A10 highway to French A8 motorway.

In 1979, Riccardo Morandi, the structural designer of the bridge, recommended some measures to protect the bridge against pollution and salty sea air, as it was located 2.4 km away from the Mediterranean Sea. However, the measures were neglected as a maintenance of the bridge was not a high priority at that time. Consequently, by 1992 the prestressed concrete cables were highly corroded.

Just four months before the collapse, a management company Autostrade per l'Italia finally decided to react and launched a public offer to repair the bridge, but it was already too late. This incident known worldwide caused Genoa companies €422 million in direct and indirect damages immediately after the collapse [6]. Morgese et al. [1] performed a post-collapse analysis of the Morandi Bridge and suggested that a real-time structural health monitoring would have provided data for maintenance and warned of impending failure.

In view of these diverse examples of the bridge failures, one can see that traffic demand has been constantly increasing in most bridges, resulting in higher loads, under harsher environments. These conditions, along with the inadequate government funding for maintenance, have accelerated deterioration processes of great part of bridges, in particular, older bridges. Moreover, it has been shown that a bridge failure has a tremendous impact on the economic, environmental, and social sustainability as they depend on the long-term durability performance of structures. Therefore, future deterioration must be prevented from irretrievable and catastrophic consequences by improving and sustaining their condition.

Periodical examination of the identified structure though visual inspection, radiographic testing, ultrasonic testing, etc. could be a solution to prevent the structure from single local damages. In addition, these traditional testing methods based on the concept of Nondestructive Evaluation (NDE) are expensive and sometimes they might not be effective enough in revealing suitable safety concerns, as controlled conditions in the laboratory do not always mimic actual field conditions. Moreover, a structure can reach a critical level before the next scheduled inspection is performed as in the case of the Nanfang'ao bridge. Therefore, more reliable, and effective diagnosis tool is required to detect deterioration processes during the life cycle of a bridge. This is where Structural Health Monitoring (SMH) comes into play as an adequate tool for monitoring of civil structures such as bridges during their service life through sensors permanently attached to the structure. The SHM process can help to detect, locate, quantify and ins some cases even prognose damage to the structure, thus reducing the probability of failures, financial losses and negative environmental impacts, as well as ensuring safety.

Another consideration is that various external factors, such as environmental and operational conditions, have an impact on the performance of SHM systems. There are numerous works in the SHM literature dedicated to address this issue using machine and statistical learning tools. For example, João P. Santos et al. [7] proposed online unsupervised detection technique for early damage detection. Moreover, W. Soo et al [8] suggested a methodology for separation damage from environmental effects for near-real time using Principal Component Analysis. However, they do not provide comprehensive solution for the bridges under traffic loading and temperature variation. This thesis attempts to address this issue by proposing and testing an approach for bridge SHM system.

1.2 Objectives

The main objective of this thesis is to proposes and tests a SHM methodology for detecting and localizing damage in bridges under traffic loads and environmental variability. The TU102 numerical benchmark selected as a case study is accessible from the GitHub platform [9].

To accomplish the main objective, some specific objectives are fulfilled:

- To study the contribution related to the Hilbert-Huang Transform (HTT). For a better understanding of this method, the mathematical formulation of Vibrational Mode Decomposition and Hilbert Transform are presented.
- To define the geometric and mechanical properties, as well as the damage and boundary conditions of the two-dimensional Finite Element (FE) bridge model.
- To study the fundamental modes and damping of the numerical bridge.
- To perform a time history analysis for the undamaged and damaged configurations of the bridge using a Python code wrapped with a Graphical User Interface (GUI).
- To create a MATLAB® script aimed to apply the HHT-based damage detection method in the numerical bridge.
- To study the application of PCA to separate the environmental effects from structural damages by using novel damage features such as the natural frequencies and Instantaneous Frequency (IF).
- To study the application of K-means and Instantaneous Frequency (IF) as the temperature effects were removed.

1.3 Scope

The scope of this thesis has been constrained in the following ways for the sake of simplicity and time constraints:

- Damage is modelled with a decrease in stiffness. This thesis does not attempt to determine the exact relationship between damage and stiffness variation.
- Proportional damping is used for this structural system with large degrees of freedom.
- In the time-history analysis, only the structure's significant bending modes are considered. Furthermore, for damage analysis, only vertical accelerations are considered.
- This thesis is focused on detection and localization of a damage. The determination of the remaining life of the numerical bridge due to damage is not considered.
- The TU102 numerical benchmark has been calibrated to represent in a better way the behaviour of a real structure. However, some assumption has been made to save time and focus on the maid idea of the study. Bridge was modelled as 2D beam and effect of the shear locking was neglected.

1.5 Outline of the thesis

The thesis is organized as follows:

Chapter 1 starts with introduction to the research topic, determines specific objectives, and ends with outlining the scope of the work.

Chapter 2 gives depth introduction to the state of the art in SHM, following different approaches used in practice and presents the proposed methodology.

Chapter 3 explains HHT which consist of VMD and HT. Both mathematical formulation and application in SHM are presented.

Chapter 4 presents PCA with mathematical formulation for dimensionality reduction.

Chapter 5 introduces clustering algorithm and their application in SHM. Moreover, it discusses K-means and describes moving window methodology for damage identification.

Chapter 6 starts with introduction of Numerical benchmark. Later, Modal analysis, Time history analysis are carried out. Finally proposed methodology tested and applied to the signals, and results are discussed.

Chapter 7 presents the final conclusions and suggestions for future research.

2. STATE OF THE ART

2.1 Structural Health Monitoring

Regardless of date of construction every structure is subjected to aging from the moment they are built. Constant deterioration, fatigue and corrosion are one of the few reasons structures lose their performance. They can sometimes cause structures to fail unexpectedly. The research in this area [10] increased after the major disaster have occurred worldwide [11] resulting to the death of considerable number of people. In this regards, SHM systems are becoming important tool to prevent human and economic losses a structural failure could result.

SHM is a damage detection strategy which can be deployed to the structure using network of devices to monitor any changes in displacement, acceleration, temperature, strain etc. Following the continuous measurements, the damage sensitive features can be extracted for further statistical analysis and assessment of current performance of the structure [12]. In **Figure 2.1**, the typical components od SHM are illustrated.

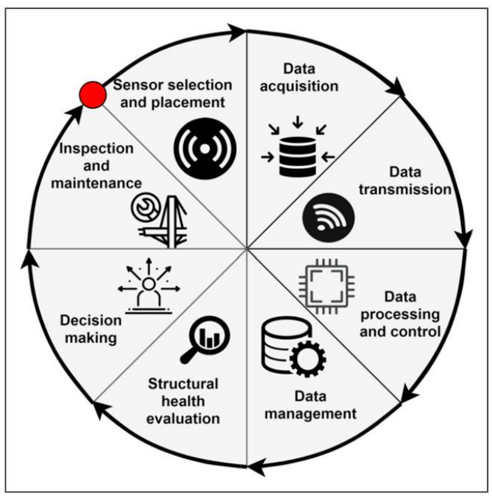

Figure 2.1 *Typical Components of SHM [12]*

A useful classification of SHM is proposed by Rytter [13], who categorized four levels of damage assessment depending on the characteristics of damage that particular SHM system can achieve.

- Level 1. A qualitative indication of damage existence (Detection)
- Level 2. A probable location of the damage (Localization)
- Level 3. An information about the extent of the damage (Assessment)
- Level 4 A prognosis of the damage (Consequence)

With the advancement of the ML algorithms, a new level that corresponds to the type of the damage, can be introduced above [12]. This new level stands between Level 2 and 3.

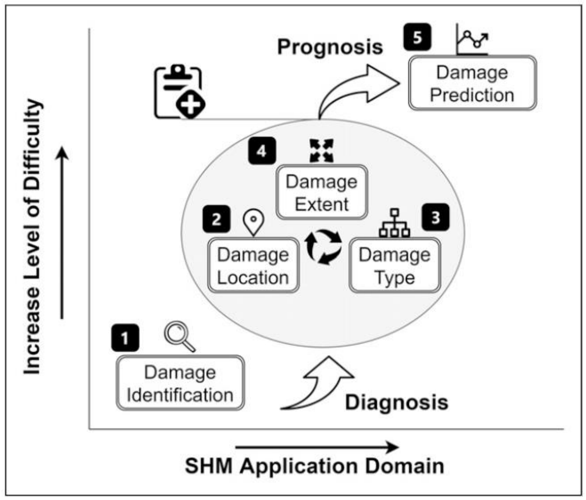

Figure 2.2 *Five-step hierarchical damage identification scheme [12]*

2.2 Model driven SHM

Model-driven techniques usually consist of construction of a high-fidelity model of the structure, for which health decisions are to be made. Most typically a Finite Element Analysis (FEA) model is used as a baseline.

The procedure for Model-driven SHM is often a two-step process. At the first stage the model is calibrated to ensure that it appropriately represents the structure under concern. This is usually done by updating the model using in-service data of the undamaged conditions. The second stage involves obtaining in-service monitoring data, for which the heath state is unknown. Then the model us updated again based on this in-service data and changes in the inferred model parameters from the baseline calibration are used to perform damage identification [14] .

There are numerous works related to model driven SHM. To name a few, Cao et al [15] developed a piezoelectric impedance measurement for structural damage identification through an inverse analysis. Similarly, Moore et al. [16] identified cracks in a thin plate by model updating.

Generally, it is hard to come up with an accurate model. Model discrepancies, especially complex structures are inevitable with little no information about joints and bonds. Such problem is not well-posed and requires regularization and simplification. Moreover, the number and the type of the parameters must be set. This creates huge problems when the damage location and type is unknown. Parametrization becomes increasingly challenging as the model fidelity increases, where there are large number of parameter sets.

2.3 Data Driven SHM

Instead of having an FEM and updating the model late, the sensing devices' data from the structures are used more conveniently in the undamaged state and under few circumstances in the damaged case. In case insufficient data exist augmentation of data driven SHM systems with the FEM can generate labelled dataset for training and validation.

However, it is crucial to highlight that physical model are computationally intensive and need validation with experimental results. On the other hand, not every ML algorithm is capable of damage prognosis, meaning data-driven approaches are not always predictive models. Therefore, the decision between employing model-driven or data-driven SHM systems or both ultimately boils down to realizing (1) the proposed system's requirements, (2) the complexity of the application where the system is deployed, and (3) if the existing data and models can support and provide valuable inferences about the health state of the structure.

2.3.1 Damage detection using machine learning and statistical methods

According to their objective use, machine learning and statistical algorithms can be categorized into three main groups:

In *Supervised Learning* (SL), the model is trained based on the given input and its expected output, i.e., the label of the input. Generally, in SHM, SL is performed on extracted features for training classifier to differentiate structural damage from environmental effects. A supervised learning algorithm can effectively go through all five damage detection stages listed above if both damaged and undamaged information is provided. As stated previously, this requires the availability of a large amount of data through sensing systems, physical-based models, or experiments. However, in many circumstances, this is not possible, and current damage state information is limited, if not unavailable [12].

In *Unsupervised Learning* (UL), the model is trained only on the inputs, without their explicitly provided labels. It classifies the input data into classes that have similar features. Compared to supervised learning, the UL method provides clear advantage as it no longer requires prior information about the state of the structure (damaged or undamaged). This learning approach, on the other hand, can only be used to detect and, in certain cases, locate damage. Furthermore, many of the deployed UL machine learning algorithms for damage identification ignore environmental and operational factors (EOFs) and depend solely on severe structural damage. Temperature effect and traffic loading are two examples of neglected variables that have a substantial impact on the response of the structures. As a result, an unsupervised technique cannot be used effectively by itself, and external factors' dependencies must be considered when determining damage.

In *Reinforcement Learning* (RL), the model tries to maximize the total profit by getting feedback on its past outcomes. RL uses rewards and penalties for the actions the autonomous agent performs.

The **Figure 2.3** shows common categories of Machine Learning algorithms and their use in the framework of SHM. Furthermore, **Table 1.1** presents most common ML algorithms in SHM are used today.

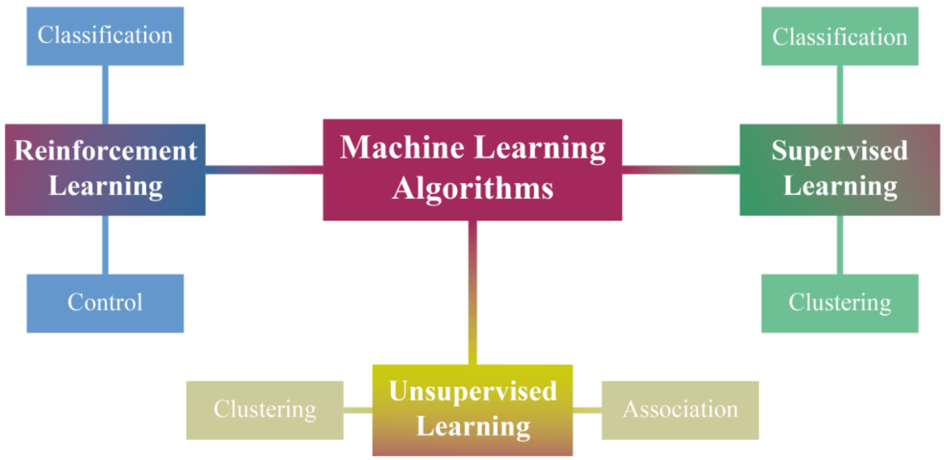

Figure 2.3 *Three main categories of ML algorithms*

Table 1.1 *Most common ML algorithms in SHM*

Supervised Learning	**Unsupervised Learning**	**Reinforcement Learning**
Random Forest	K-means	Genetic Algorithms
Decision Tree	Gaussian Mixture	Q-learning
Support Vector Machine	Association analysis	State-Action-Reward-State-Action
k-nearest Neighbor	Blind Source Separation	
Bayesian	Neural Network	
Neural Network		

2.4 Proposed methodology

There are numerous works in the literature, where machine learning and statistical methods have been implemented in SHM of bridges under traffic loading. For example, Fernando Tenelema Muñoz [17] showed that PCA is efficient for differentiating environmental effects from selected data. He used phase differences as damage-sensitive features on a steel bridge and demonstrated that 1st Principal Component (PC) is purely related to temperature effects. Even though temperature effect was clearly shown, the bridge FEM model did not accurately represent a real structure. Moreover, the damage detection was based on the variance changes in 2nd PC of PCA, which cannot guarantee certainty in real cases because of excess noise.

Meanwhile, Rick M. Delgadillo [18] demonstrated on real steel truss bridge that instantaneous frequencies are reliable damage sensitive features. He applied Hilbert-Huang Transform to process the vibration data and performed unsupervised cluster-based machine learning (K-means) on symbolic data. As a result, K-means was proved to be efficient to detect and localize the damage. However, the environmental effects were not considered because of insufficient data available for both healthy and damaged bridge at different temperatures.

The objective of this thesis is to propose a SHM methodology for a bridge under traffic loading and different temperatures. Based on the 2 previous works by Fernando and Rick, which do not deal completely with all environmental and operational effects, this study treats them in a comprehensive way. **Figure 2.4** below shows a flow chart of proposed methodology.

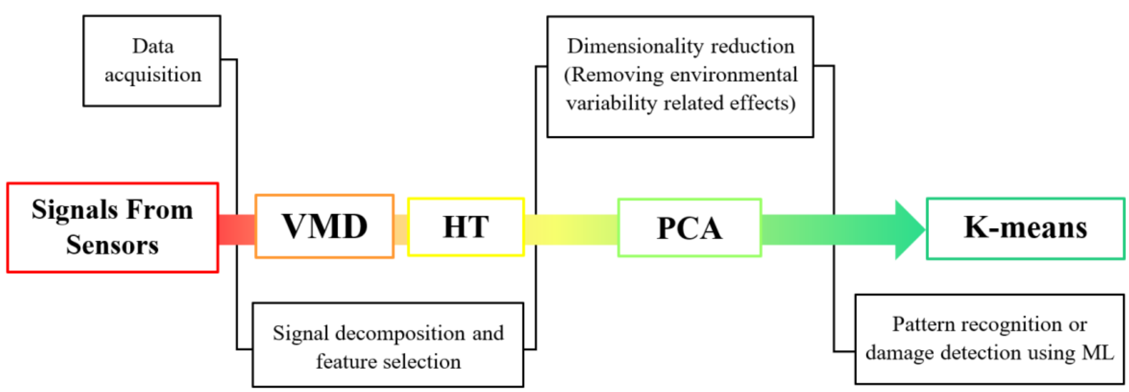

Figure 2.4 *Flow chart of the proposed SHM methodology*

1. Signals under traffic loads and at different ambient temperatures are collected from sensors.
2. Hilbert-Huang Transform (HHT) which consist of Vibrational Mode Decomposition (VMD) and Hilbert Transform (HT) is applied to recorded data. The goal of this step is to decompose the signal into Intrinsic Mode Functions and select damage-sensitive feature for the next step. In this study, instantaneous frequencies are considered.

3. Principal Component Analysis is performed to reconstruct the data using Principal Components (PC) which are not affected by the environmental changes (temperature).
4. Symbolic data analysis is performed, and cluster based moving window K-means algorithm is applied to selected undamaged and damaged scenarios to detect and localize the damage.

3. HILBERT HUANG TRANSFORM - HHT

3.1 VMD method

Variational Mode Decomposition (VMD) has been widely used in different applications since it was proposed by Dragomiretskiy and Zosso in 2014 [19]. They proposed an entirely non-recursive variational mode decomposition model by extracting modes concurrently. The model was developed to overcome Empirical Mode Decomposition (EMD) limitations of sensitivity to noise and sampling.

The VMD is widely used in structural identification of modal properties of engineering structures based on dynamic response. For example, Bagheri et al. [20] demonstrated the efficiency of VMD algorithm by series of numerical, laboratory and field case studies. The vibration response of a three-story shear frame was used in laboratory case, whereas a field study covered the ambient vibration response of a pedestrian bridge. Moreover, the modal properties of the of the shear frame were computed using analytical approach for the comparison with experimental modal frequencies. As a result, the VMD-based system identification was proven to be robust against noise and sampling frequency with respect to traditional signal decomposition such as EMD.

The main "drawback" of this method is that the number of modes *K* must be set in advance [21]. If the selected mode number is not accurate, the VMD will cause the loss of important modes. In order to determine the number of IMFs different methods have been proposed correlation coefficient method [22], the normalized mutual information method [23], and, the most common, the center frequency observation method [24].

The goal of VMD is to decompose a real valued input signal f into a discrete number of quasi-orthogonal band-limited sub-signals u_k (modes). Each mode is compact around the center pulsation ω_k and the bandwidth is estimated using H^1 Gaussian smoothness of the shifted signal [24]. The VMD is written as a constrained variational problem:

$$\min_{\{u_k\},\{\omega_k\}} \left\{ \sum_{k=1}^{K} \left\| \partial_t \left[\left(\delta(t) + \frac{j}{\pi t} \right) * u_k(t) \right] e^{-j\omega_k t} \right\|_2^2 \right\}$$

$$s.t. \sum_{k=1}^{K} u_k = f$$

where u_k and ω_k are the *k*th intrinsic mode function and it is center frequency, respectively.

$$\mathcal{L}(\{u_k\},\{\omega_k\},\lambda) = \alpha \sum_{k} \left\| \partial_t \left[\left(\delta(t) + \frac{j}{\pi t} \right) * u_k(t) \right] e^{-j\omega_k t} \right\|_2^2$$

$$+\left\|f(t)-\sum_k u_k(t)\right\|_2^2+\langle\lambda(t), f(t)-\sum_k u_k(t)\rangle$$

where α denotes the balancing parameter of the data-fidelity constraint, which is also penalty factor.
The equation above can be solved with alternate direction method of multipliers (ADMM). All the modes gained from the solutions in spectral domain are written as:

$$\hat{u}_k^{n+1}(\omega)=\frac{\hat{f}(\omega)-\sum_{i\neq k}\hat{u}_i(\omega)+\left(\frac{\hat{\lambda}(\omega)t}{2}\right)}{1+2\alpha(\omega-\omega_k)^2}$$

which is identified as a Winer filtering residual, with signal prior $1/(\omega-\omega_k)^2$. Thus, making VMD algorithm much more robust to sampling and noise. The update equation for the center frequency is expressed as

$$\omega_k^{n+1}=\frac{\int_0^\infty \omega|\hat{u}_k(\omega)|^2\,d\omega}{\int_0^\infty|\hat{u}_k(\omega)|^2\,d\omega}$$

Complete algorithm is extracted from [19]:

Initialize $\{\hat{u}_k^1\}$, $\{\hat{\omega}_k^1\}$, $\hat{\lambda}^1$, $n\leftarrow 0$

repeat

$n\leftarrow n+1$

for $k=1{:}K$ **do**

Update $\hat{u}_k$ for all $\omega\geq 0$:

$$\hat{u}_k^{n+1}(\omega)\leftarrow\frac{\hat{f}(\omega)-\sum_{i<k}\hat{u}_i^{n+1}(\omega)-\sum_{i>k}\hat{u}_i^{n}(\omega)+\left(\frac{\hat{\lambda}^n(\omega)}{2}\right)}{1+2\alpha(\omega-\hat{\omega}_k^n)^2}$$

Update ω_k:

$$\omega_k^{n+1}\leftarrow\frac{\int_0^\infty \omega|\hat{u}_k^{n+1}(\omega)|^2\,d\omega}{\int_0^\infty\left|\hat{u}_k^{n+1}(\omega)\right|^2\,d\omega}$$

end for

Dual ascent for all $\omega\geq 0$:

$$\hat{\lambda}^{n+1}(\omega) \leftarrow \hat{\lambda}^{n}(\omega) + \tau\left(\hat{f}(\omega) - \sum_{k} \hat{u}_k^{n+1}(\omega)\right)$$

until convergence: $\sum_k \|\hat{u}_k^{n+1} - \hat{u}_k^{n}\|_2^2 / \|\hat{u}_k^{n}\|_2^2 < \varepsilon_r$.

The stopping criterion of the algorithm is mainly based on relative tolerance ε_r. However, in the MATLAB implementation of VMD, two additional criteria are considered:
1. Maximum number of optimization iterations *O*
2. Absolute tolerance ε_a

$$\sum_{k} \|\hat{u}_k^{n+1} - \hat{u}_k^{n}\|_2^2 < \varepsilon_a$$

In this case, optimization stops either when the number if iterations is greater than *O* or ε_a and ε_r are satisfied.

The purpose of VMD for signals is to obtain meaningful IMFs. The flow of the VMD algorithm presented by Wu et al. [24] is shown in Figure.

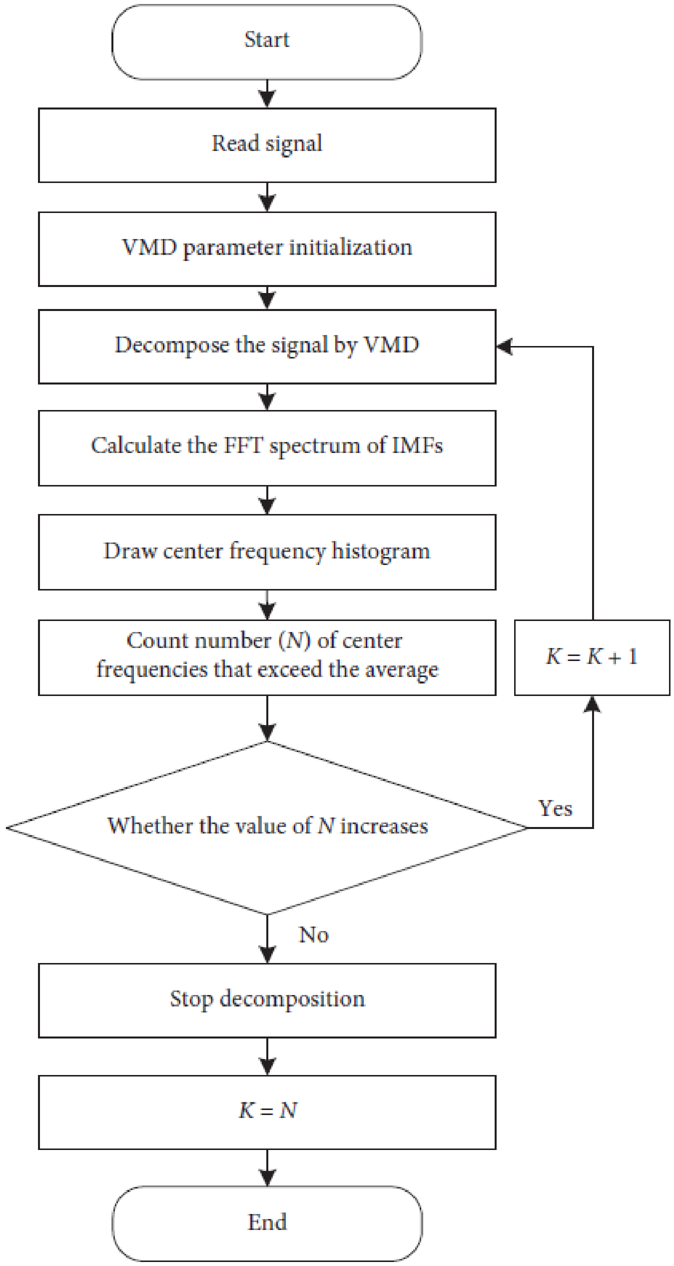

Figure 3.1 *Flow diagram of the VMD algorithm using the centre frequency statistical analysis to find the number of IMFs K required, extracted from [24]*

3.2 Hilbert Spectral Analysis

3.2.1 Hilbert Spectrum

The Hilbert transform is a linear operator that transforms a real signal $x(t)$ into another real signal, indicated by $H[x(t)]$. It is defined as the convolution of $x(t)$ with the function $1/(\pi t)$:

$$H[x_k(t)] = \frac{1}{\pi} P.V \int_{-\infty}^{+\infty} \frac{x_k(\tau)}{t-\tau} d\tau$$

$P.V$ denotes the Cauchy principal value of the integral and $x_k(t)$ corresponds to the *kth* IMF component obtained from the mode decomposition technique. For the simplicity purposes, the notation $x_k(t)$ is used instead of $IMF_k(t)$ in all equations below. The HT allows us to define the complex analytic signal $z_k(t)$, from which instantaneous amplitude and phase can be calculates from it. An analytic signal represents rotation in the complex plane with the rotation radius $a_k(t)$ and the instantaneous function $\theta_k(t)$ [21]. This implies that analytic signal becomes:

$$z_k(t) = x_k(t) + i\, H[x_k(t)] = a_k(t) e^{i\theta_k(t)}$$

$H[x_k(t)]$ – represent Hilbert transform of the $IMF_k(t)$
$a_k(t)$ – instantaneous amplitude
$\theta_k(t)$ – instantaneous phase function
And the formulas of amplitude and phase are taken from [21].

$$a_k(t) = \sqrt{\{x_k(t)\}^2 + \{H[x_k(t)]\}^2}$$

$$\theta_k(t) = \arctan\left(\frac{H[x_k(t)]}{x_k(t)}\right)$$

The instantaneous amplitude $a_k(t)$ describes the envelope of the denoised $IMF_k(t)$, while $\theta_k(t)$ is describes the number of the rotations.

The concept of the frequency and phase carry significant importance when applying IMFs [25]. If the IMFs can be considered local, then the instantaneous angular frequency $\omega_k(t)$ can be defined as:

$$\omega_k(t) = \frac{d\theta_k(t)}{dt} = 2\pi f_k(t)$$

Cohen stated that each IMF is a mono-component signal with a monotonically increasing phase and a positive instantaneous frequency. Therefore, each selected IMF can be defined as:

$$x_k(t) = Re(z_k(t) = Re\left(a_k(t)e^{i\theta_k(t)}\right) = a_k(t)\cos\left[\theta_k(t)\right]$$

The total instantaneous frequency phase for the selected $\theta(t)$ can be obtained by the sum of the instantaneous phases for the selected IMFs:

$$\theta(t) = \sum_k \theta_k(t) = \sum_k arctan\left(\frac{H[x_k(t)]}{x_k(t)}\right)$$

where:
$x_k(t)$ – physically meaningful IMFs selected for spectral analysis
$\theta(t)$ – the total number of rotations of a significant part of the original measured signal $x(t)$ in the complex plane in radians (rad)

3.2.2 Limitations of the Hilbert Transform

Hilbert Transform can be applied to any arbitrary signal to compute instantaneous amplitude, phase, and frequency. However, they have a clear physical meaning only if $x(t)$ is an oscillatory signal with narrow band of frequency [26]. In this case, the amplitude $A(t)$ coincides with the envelope of $x(t)$ and the frequency $\omega_k(t)$ coincides with the frequency of the maximum power spectrum computed in a running window.

In real world situations, signals are superpositions of oscillating components with different time scales. The instantaneous amplitude, phase, and frequency lack clear physical meaning. However, they can be helpful for understanding and characterizing the dynamical system that generates the signal.

A well-known method to overcome Hilbert Transform limitations was proposed by Huang [ref] A well-established method is the empirical mode decomposition, that breaks down the original signal into a set of intrinsic mode functions. Each one of these functions admits a “well-behaved” Hilbert transform and is fully characterised by instantaneous amplitude and phase with the physical meaning of a rotation

4. PRINCIPAL COMPONENT ANALYSIS

4.1 Overview

PCA is a multivariate statistical approach that analyses patterns in a data set to highlight similarities and differences. It's mostly used to reduce the original data set's dimensions without losing too much information [27]. It creates new non-correlated variables (latent variables) to represent termed 'principal components' to represent the different factors affecting the data set [8].

4.2 Mathematical formulation

4.2.1 Data collection

Let **Z** denote a $n \times m$ data set if damage sensitivity features collected from m observations with a $n < m$. For each observation, n numbers of damage sensitivity features are collected [27].

$$\mathbf{Z} = \begin{pmatrix} x_{1,1} & \cdots & x_{1,m} \\ \vdots & \ddots & \vdots \\ x_{n,1} & \cdots & x_{n,m} \end{pmatrix} = (v_1 | \cdots | v_j | \cdots | v_m)$$

To perform PCA on the damage sensitivity features data set, mean cantering of the data set is first required. It is achieved by subtracting the mean of each row of the data set to each measurement in that row. The resulting matrix **X** after the mean centring will have the same dimensions $n \times m$ as the original data set **Z** [27].

4.2.2 Covariance matrix and PCA objective

The covariance matrix of the mean centred matrix **X** is defined as:

$$\mathrm{C_X} = \frac{1}{n-1}\mathbf{X^T X} = \frac{1}{n-1}\begin{pmatrix} v_1^T v_1 & \cdots & v_1^T v_m \\ \vdots & \ddots & \vdots \\ v_m^T v_1 & \cdots & v_m^T v_m \end{pmatrix}$$

It is squared symmetric $m \times m$ matrix that measures the degree of linearity within data set [ref] The diagonal terms are the variances of the corresponding variables:

$$\sigma_{v_j}^2 = \frac{1}{n-1} v_j^T v_j = \frac{1}{n-1} \sum_{i=1}^{n} x_{ij}^2$$

The off-diagonal terms are the covariance between pairs of variables:

$$\sigma_{v_j, v_k}^2 = \frac{1}{n-1} v_j^T v_k = \frac{1}{n-1} \sum_{i=1}^{n} x_{ij} x_{ik}$$

Large covariance values correspond to high redundancy and small values to low redundancy.

4.2.3 Transforming the data matrix

PCA transforms the data set **X** into new data set **T** with smaller dimensions which characterizes most of the variances in the original data set [28]. **P** is a linear transformation matrix with dimension $m \times n$.

$$\mathbf{T} = \mathbf{XP}$$

To have the minimal redundancy, transformation matrix **P** should be such that the covariance of the new data matrix **T** is diagonal

$$\mathbf{C_T} = \frac{1}{n-1} \mathbf{T}^{\mathrm{T}} \mathbf{T} = diagonal$$

Substituting into the following

$$\mathbf{C_T} = \frac{1}{n-1} \mathbf{P}^{\mathrm{T}} \mathbf{X}^{\mathrm{T}} \mathbf{XP} = \mathbf{P}^{\mathrm{T}} \mathbf{C_X} \mathbf{P}$$

$\mathbf{C_X}$ is symmetric matrix. It has m real eigenvalues λ_j, and m orthonormal eigenvectors $\boldsymbol{p_j}$, which form a basis in the m - dimensional space. Then the transformation matrix is chosen having the eigenvectors in their columns, that is

$$\mathbf{P} = (p_1 | \cdots | p_j | \cdots | p_m)$$

And the following property must be satisfied

$$\mathbf{C_X P} = \mathbf{P} \Lambda$$

where $\Lambda = (\lambda_1, \lambda_2, \cdots, \lambda_m)$
Substituting the equation above into $\mathbf{C_T}$, the condition below is met:

$$\mathbf{C_T} = \mathbf{P}^{\mathrm{T}}\mathbf{P}\Lambda = \Lambda$$

In detail:

$$(t_1|\cdots|t_j|\cdots|t_m) = \begin{pmatrix} x_{1,1} & \cdots & x_{1,m} \\ \vdots & \ddots & \vdots \\ x_{n,1} & \cdots & x_{n,m} \end{pmatrix} \times (p_1|\cdots|p_j|\cdots|p_m)$$

Each column vector in matrix T can be expressed as

$$\boldsymbol{t}_j = \mathbf{X}\boldsymbol{p}_j$$

Then the variances of these vectors can be computed in the form

$$\sigma_{t_j}^2 = \frac{1}{n-1}\boldsymbol{t}_j^T\boldsymbol{t}_j = \frac{1}{n-1}\left(\mathbf{X}\boldsymbol{p}_j\right)^T\left(\mathbf{X}\boldsymbol{p}_j\right) = \boldsymbol{p}_j{}^T\mathbf{C_X}\boldsymbol{p}_j = \lambda_j$$

While covariances are null

$$\sigma_{t_j,t_k}^2 = \frac{1}{n-1}\boldsymbol{t}_j^T\boldsymbol{t}_j = \frac{1}{n-1}\left(\mathbf{X}\boldsymbol{p}_j\right)^T\left(\mathbf{X}\boldsymbol{p}_k\right) = \boldsymbol{p}_j{}^T\mathbf{C_X}\boldsymbol{p}_k = \lambda_j\boldsymbol{p}_j{}^T\boldsymbol{p}_k = 0$$

4.2.4 Reducing the dimension

It is possible to reduce the dimensionality of the data of the matrix **X** by choosing only reduced number r of principal components, as the eigenvalues are ordered according to the amount of the information.

The definition of the reduced transformation $m \times r$ matrix

$$\mathbf{P} = (p_1|p_2|\cdots|p_r)$$

The original data can be projected on the space by this matrix as before:

$$\mathbf{T} = \mathbf{XP}$$

In the full dimension case, this projection is invertible) and the original data can be recovered as $\mathbf{X}(\mathbf{PP}^{\mathrm{T}})$. Now, with the given T, it is not possible to fully recover X, but T can be projected back onto the original m-dimensional space and obtain another data matrix as follows:

$$\widehat{\mathbf{X}} = \mathbf{T}\mathbf{P}^{\mathrm{T}} = \mathbf{X}(\mathbf{P}\mathbf{P}^{\mathrm{T}})$$

By simple manipulations (adding and subtracting) in expression above, the following decomposition of the original data matrix X can be written:

$$\mathbf{X} = \widehat{\mathbf{X}} + \widetilde{\mathbf{X}}$$

$$\widehat{\mathbf{X}} = \mathbf{X}(\mathbf{P}\mathbf{P}^{\mathrm{T}})$$

$$\widetilde{\mathbf{X}} = \mathbf{X}(\mathbf{I} - \mathbf{P}\mathbf{P}^{\mathrm{T}})$$

where $\widehat{\mathbf{X}}$ is the projection of the data matrix $\mathbf{X}$ onto the selected r principal components and $\widetilde{\mathbf{X}}$ is the projection onto the residual left components.

5. CLUSTERING ALGORITHM

5.1 A Survey of Clustering Algorithms

Cluster analysis is the study of the methods and algorithms of grouping, or clustering, objects according to measured or perceived intrinsic characteristics or similarity. The absence of category information distinguishes data clustering (unsupervised learning) from classification or discriminant analysis (supervised learning). Unlike supervised algorithms, clustering algorithms do not require the definition of reference/training data. They can ‘understand’ a data set’s structure by attempting to find the most compact and separates set of clusters [7].

The main goal of the clustering algorithms is to find a structure in the data. Mathematically speaking, it is an attempt to minimize the dissimilarity between data objects within same cluster and, meanwhile, to maximize the dissimilarity between objects assigned to different clusters [7].However, there is no agreement for the complete definition of clustering, and a classical one is given below [29]:
1. Instances, in the same cluster, must be similar as much as possible.
2. Instances, in the different clusters, must be different as much as possible.
3. Measurement for similarity and dissimilarity must be clear and have the practical meaning.

As it was mentioned above, the distance (dissimilarity) and similarity are the basis for constructing clustering algorithms. Depending on data features, quantitative or qualitative, distance or similarity functions are applied respectfully. The Table 5.1 and 5.2 show common functions used for quantitative and qualitative data.

Table 5.1 *Distance functions [29]*

Name	Formula	Explanation
Minkowski distance	$\left(\sum_{l=1}^{d} \lvert x_{il} - x_{jl} \rvert^{n}\right)^{1/n}$	A set of definitions for distance: 1. City-block distance when n = 1 2. Euclidean distance when n = 2 3. Chebyshev distance when n→ ∞
Standardized Euclidean distance	$\left(\sum_{l=1}^{d} \left\lvert \frac{x_{il} - x_{jl}}{s_l} \right\rvert^{2}\right)^{1/2}$	1. S stands for the standard deviation 2. A weighted Euclidean distance based on the deviation

Cosine distance	$1 - cos\alpha = \frac{x_i^T x_j}{\|x_i\| \|x_j\|}$	1. Stay the same in face of the rotation change of data 2. The most commonly used distance in document area
Pearson correlation distance	$1 - \frac{Cov(x_i, x_j)}{\sqrt{D(x_i)}\sqrt{D(x_j)}}$	1. Cov stands for the covariance for and D stands for the variance 2. Measure the distance based on linear correlation
Mahalanobis distance	$\sqrt{(x_i - x_j)^T S^{-1}(x_i - x_j)}$	1. S is the covariance matrix inside the cluster 2. With high computation complexity

Table 5.2 *Similarity functions [29]*

Name	**Function formula or measure method**	**Explanation**
Jaccard similarity	$J(A, B) = \left\|\frac{A \cap B}{A \cup B}\right\|$	1. Measure the similarity of two sets 2. |X| Stands for the number of elements of set X 3. Jaccard distance = 1 − Jaccard similarity
Hamming similarity	The minimum number of substitutions needed to change one data point into the other	The number is smaller, the similarity is more Hamming distance is the opposite of Hamming similarity Especially for the data of string

For data of mixed type	Map the feature into (0, 1) Transform the feature into dichotomous one $S_{ij} = \frac{1}{d}\sum_{l=1}^{d} S_{ijl}$ $S_{ij} = (\sum_{l=1}^{d} \eta_{ijl} S_{ijl})/(\sum_{l=1}^{d} \eta_{ijl})$

The traditional clustering algorithms can be divided into 9 categories, which mainly contain 26 commonly used. The summary is given below in the table.

Table 5.3 *Traditional algorithms*

Category	Typical algorithm
Clustering algorithm based on partition	K-means, K-medoids, PAM, CLARA, CLARANS
Clustering algorithm based on hierarchy	BIRCH, CURE, ROCK, Chameleon
Clustering algorithm based on fuzzy theory	FCM, FCS, MM
Clustering algorithm based on distribution	DBCLASD, GMM
Clustering algorithm based on density	DBSCAN, OPTICS, Mean-shift
Clustering algorithm based on graph theory	CLICK, MST
Clustering algorithm based on grid	STING, CLIQUE
Clustering algorithm based on fractal theory	FC
Clustering algorithm based on model	COBWEB, GMM, SOM, ART

As it can be seen from the **Table 5.3**, there are numerous categories and types of algorithms. In this thesis, K-means is taken into consideration. It is a clustering algorithm based on partition. The basic idea behind this type of algorithms is to regards the center of data points as the center of the corresponding cluster [29].

5.2 K-means

Let $P_K = \{C_{K,} \dots , C_K\}$ be partitioned into K clusters. Then, the overall within-cluster $W(P_K)$ dissimilarity can be defined as [7]

$$W(P_K) = \frac{1}{2}\sum_{k=1}^{K}\sum_{c(i)=k}\sum_{c(j)=k} d_{ij}$$

where $c(i)$ is many-to-one allocation rule that assigns object i to cluster $k,$ based in a dissimilarity measure, d_{ij}, defined between each pair of data objects, i and j.

The overall dissimilarity of a data set, OD, is given below.

$$OD = \frac{1}{2}\sum_{i=1}^{N}\sum_{j=1}^{N} d_{ij}$$

where, N is the total number of objects. The between-cluster dissimilarity is obtained by subtracting the previous two equations, $B(P_K) = OD - W(P_K)$.

The goal of the K-means is to minimize the overall within-cluster dissimilarity, $W(P_K)$, of a given partition, P_K, by iterative optimization scheme. The K-means requires that the number of K<N clusters be initially defined [7] with randomly defined set of K clusters' prototypes from the same type of data. This step is called initialization as shown **Figure 5.1a**. Bigger blue dots represent randomly defined prototypes, while smaller dots represent the data that being clustered. Following the initialization, each iteration starts by assigning objects to clusters by allocating rule, $c(i)$, **Figure 5.1b.** The second step of the K-means algorithms is to find the best prototypes that represent clusters defined before. It is called representation step and illustrated in **Figure 5.1c**. K-means represents the clusters by finding their centroids. Further allocation and representation are repeated (**Figure 5.1d, e**) until an objective function, which depends on cluster compactness and separation, reaches its global minimum value [7].

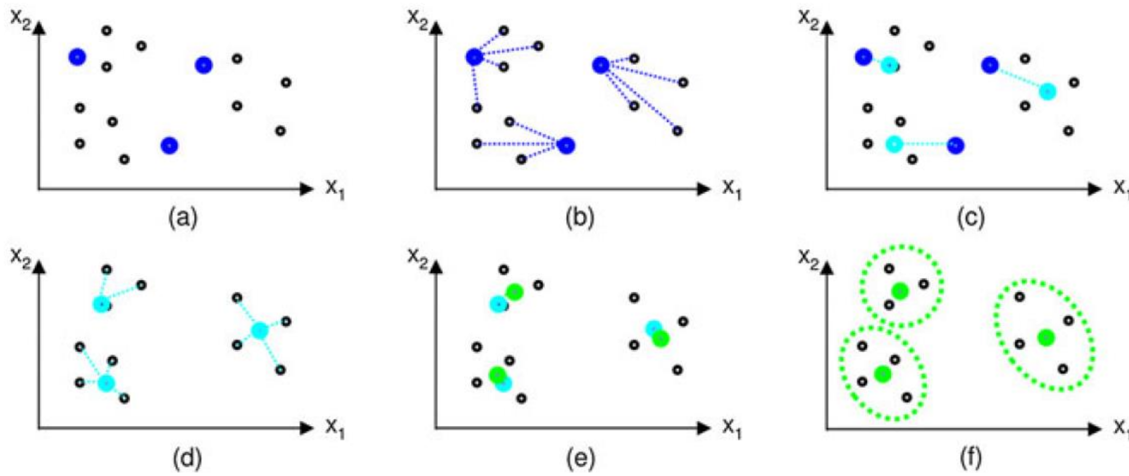

Figure 5.1 *K-means clustering algorithm:* ***(a)*** *initialization (three cluster prototypes to describe 11 objects);* ***(b)*** *iteration 1, allocation;* ***(c)*** *iteration 1, representation;* ***(d)*** *iteration 2, allocation;* ***(e)*** *iteration 2, representation; and* ***(f)*** *final set of clusters' prototypes. [7]*

The K-means uses squared within-cluster dissimilarity measured across the K clusters as objective function [29]. They are usually based on distance metrics. The most used one is Euclidean distance (square root of the sum-of-squares). However, in the application of SHM it leads to computational complexity and large incidents of false detection [7]. To overcome these difficulties, the Gowda-Diday distance measure is used.

5.3 A methodology for damage identification

The k-means algorithm demands the initial definition of the number of $K \leq N$ of clusters as well as a randomly defined set of cluster prototypes, which are objects of the same type as those being clustered. The representation step of each k-means iteration is the process of determining which set of prototypes best represents the clusters defined during the allocation phase. This number is supposed to be the same as the number of unique structural conditions determined on site, and there is no means of knowing it advance. Without determining which of the partitions best represents the data's structure, clear conclusions cannot be drawn. The global silhouette index is employed in this study since it performed better in prior investigations when its formulation was thoroughly discussed [30] [31] The construction of silhouette statistic consists in assigning a fixed number of clusters K to the ith observation, with the following value [18]:

$$s(x_i) = \frac{b(x_i) - a(x_i)}{\max\{a(x_i),\ b(x_i)\}} \in [-1,1]$$

Where $b(x_i)$is the distance to nearest neighbouring cluster's centre and $a(x_i)$ is the average distance between the ith object of cluster C and the remaining j objects. The silhouette index of clusters and the average of silhouette widths for all samples are respectively given below. Where $(1 \leq M_k \leq N)$, N = set of objects, K = clustering partitions and the value of silhouette coefficient varies from 0 to 1.

$$s(x) = \frac{1}{M_k} \sum_{i=1}^{M_k} s(x_i)$$

$$SIL = \frac{1}{K} \sum_{k=1}^{K} s(x)$$

For the present work, it is important to note that the partition that, among the K tested, generates the highest SIL value is the one that best describes the analysed data set, and thus which should be considered for SHM purposes.

Cluster analysis is capable automatically distinguishing between structural conditions without any assumption regarding prior the structural condition on site. However, the user intervention is required to assess the output whether they are compact or mixed over time. It creates several difficulties to implement the method near real time application. To overcome this issue Santos et al [7] proposed robust strategy for damage detection using cluster-based algorithm with moving time windows method. It relies on the average difference between cluster rather relying on the allocation of data objects to cluster over time [7].

$$DC = \frac{1}{K(K-1)} \sum_{k=1}^{K} \sum_{\substack{c=1 \\ c \neq 1}}^{K} d_{ck}$$

where K is the number of clusters from the partition with highest SIL, c and k are two of the K clusters and d_{ck} is Gowda-Diday dissimilarity measured between their centroids. If there is no damage and structural behaviour is stable, the clusters generated by the k-means are similar and will generate small values of DC. Consequently, if they damage is observed, the k-means algorithm will create dissimilar and separate clusters and large values of the DC. Moreover, Santos et al [7] argues that DC if highly sensitive to early damage and capable of performing significant data fusion, as the data acquired from multiple sensors are described as single-value index.

Ideally, TRUE/FALSE binary information should be provided by the detection strategy. The time windows are defined with fixed length equal *SL*, where *L* is the time length of each data sample and *S* is the number of samples per window. As the value of DC is not informative (it does not provide TRUE/FALSE information), by itself, Santos et al [7] proposes statistical testing the DC values obtained withing each time window's length. The statistical testing of the DC values results in the definition of the confidence boundary (CB), which should be exceed only in case structural system exhibits changes.

The CB is defined each time window, by statistically testing DCs distribution, under the assumption that the only the random effects influence on the residual errors obtained from unchained structures. Generally, Normal statistical distribution is used SHM works related to the damage detection. However, the small number of the DC values contained in each time window has motivated to use t-student distribution, which is more appropriate for describing small samples extracted from Gaussian population [7].

The confidence boundary at each time window is obtained as follows:

$$CB = E[DC] + t_{s-1,\frac{1}{2}+\frac{\beta}{2}} \times E\big[DC - E[DC]\big]/\sqrt{S}$$

where $t_{s-1,\frac{1}{2}+\frac{\beta}{2}}$ is the $\frac{1}{2}+\frac{\beta}{2}$ percentile of a t-student distribution with S-1 degrees of freedom and β is the confidence level, taken 99.9%.
$E[DC]$ and $E\big[DC - E[DC]\big]$ are expected value and variability estimates of the DC sample within analysed time window, respectively.

Finally, using DC and CB values, Santos et al [7] proposed an original detection index, DI. It is defined such that (i) its positive values indicate damage detection ("TRUE") and negative or null values stand for unchanged structural response ("FALSE"); (ii) it is dimensionless; and (iii) it has unsupervised and window-wise character by using only information related to a single time window.

$$DI = \frac{max_i(DC_i - CB)}{med_i(DC_i)}; \quad i = 1, \dots, S$$

6. CASE STUDY

6.1 Introduction

The objective of this chapter is to test the methodology that was proposed above for damage detection and localization. Initially, the chapter begins with the introduction of the numerical benchmark along with the material and geometry of the bridge that is considered in this work. Next, the modal analysis is performed to determine the natural frequencies and effective mass participation factor (EMPF). Furthermore, the time history analysis is performed to extract the acceleration data. The relationship between temperature and the modulus of elasticity of the bridge material is introduced along the way. Finally, the section of results and discussion is presented, where the effectiveness of the proposed methodology is shown.

6.2 Benchmark description.

The TU102 is a numerical benchmark model with open-source code for generation of simulated data. It represents the superstructure component of a two-span continuous beam bridge subjected to changing environmental and operational conditions. The model was developed by Tatsis and Chatzi as part of COST Action TU1402 on Quantifying the Value of Information and is to serve as a reference case study for validation of decision-making tools relying on the Value of Information [9].

The numerical model represents a structural dynamics benchmark problem. The superstructure consists of a single rectangular-shaped beam considered as the primary longitudinal support member for carrying the deck and transferring the load to the piers and down to the foundation. The bridge superstructure modelling was developed by Tatsis and Chatzi via open-source Python scripts which are made available through GitHub [9]. Note that the International System (SI) of units (m, kg, s) is assumed to provide consistent results. In this section, the geometry and mechanical properties of the two-span continuous beam is firstly presented as well as an estimate of the stiffness for the elastic supports. Then, a finite element (FE) analysis is presented. Lastly, different damage scenarios and sensing points are shown.

6.2.1 Geometry and material properties

The bridge superstructure consists of a two-span continuous beam with equal length (L_1= L_2=10m). The cross section of the beam is rectangular with constant width 10m and height 0.6m

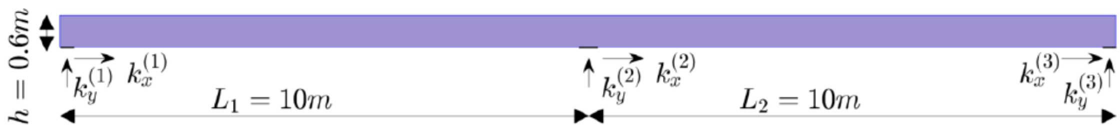

Figure 6.1 *Geometry of the two-span bridge in the longitudinal direction with elastic boundaries.*

The bridge is assumed to be made from reinforced concrete with $E = 35\,GPa$. It is linear elastic material with density ρ = 2400 kg/m^3 at ambient temperature $T = 20°\,C$ and Poisson's ratio ν = 0.2. **Table 6. 1** below summarizes the geometry and the mechanical properties.

Table 6. 1 *Geometry and mechanical properties of the numerical bridge superstructure*

Geometry (units)	Symbol	Value
Left-span length (m)	L_1	10
Right-span length (m)	L_2	10
Total bridge length (m)	L	20
Bridge height (m)	h	0.6
Bridge width (m)	t	10
Material properties at $T = 20°\,C$		
Mass density (kg/m^3)	ρ	2400
Young's Modulus (GPa)	E	35
Poisson's ratio	ν	0.2
Shear Modulus (GPa)	G	14.6

For homogeneous isotropic linear elastic materials, the shear modulus G is calculated as follows

$$G = \frac{E}{2(1+\upsilon)}$$

6.2.2 Elastic bearings

Bridge bearings are required to transfer load from the superstructure to the substructure, which includes abutments, piers, and foundation, in a proper and safe manner. The primary goal of bearings is to provide flexibility to bridges while also ensuring proper load distribution on the substructure. They also enable the superstructure to adjust longitudinal movement in response to changes in temperature or moving loads. Because of this, bearings' vertical stiffness must be substantially greater than their lateral stiffness. 9 elastic bearings are modelled as a three evenly spaced elastic supports and put on the bottommost edge of the bridge superstructure in this case study.

Two elastic supports are located at both ends in a width of 0.3m and one intermediate support is located at the middle of the beam in a width of 0.4m. All three supports are modelled as point spring supports, each with two degrees of freedom acting at the corresponding mesh element nodes. **Table 6.2** summarizes the horizontal stiffness, k_x, and vertical stiffness, k_y, adopted for the three spring supports to avoid the "mixing" of longitudinal and bending mode shapes as much as possible.

Table 6.2 *Horizontal stiffness, kx, and vertical stiffness, ky, adopted for the three spring supports.*

Stiffness (units)	Left support	Mid support	Right support
k_x (N/m)	10714200	19285500	10714200
k_y (N/m)	10^{15}	10^{20}	10^{15}

6.2.3 FE Analysis

A two-dimensional (2D) FE model is constructed for the plane stress problem using isoparametric quadrilateral elements whose formulation is characterized by using the same shape functions to interpolate the displacement field and nodal coordinates (geometry), as explained by Oñate [32]. There are two degrees of freedom (DOFs) per node in these elements, which correspond to vertical and horizontal displacements. Although isoparametric elements take up more CPU time, they are preferable to estimate displacement fields for complex and simple planar elements like beams, making them ideal for our research case: a regular-shaped beam with minimum distortion. In addition, when integrating the stiffness and mass matrices of these elements, the Gaussian quadrature (GQ) is used to approximate the definite integrals of the shape functions over the element domain by a weighted sum of functional evaluations at a specified number of sample points (Gauss points), resulting in the desired degree of accuracy in the results.

FIG shows the three isoparametric quadrilateral elements, using either full or reduced integration, whose mathematical formulation are implemented in the benchmark's python scripts.

1) A four-node bilinear quadrilateral element (QUAD4: 4-Node, 8-DOFs).
2) An eight-node Serendipity quadrilateral element (QUAD8: 8-Node, 16-DOFs).
3) A nine-node Lagrangian quadrilateral element (QUAD9: 9-Node, 18-DOFs).

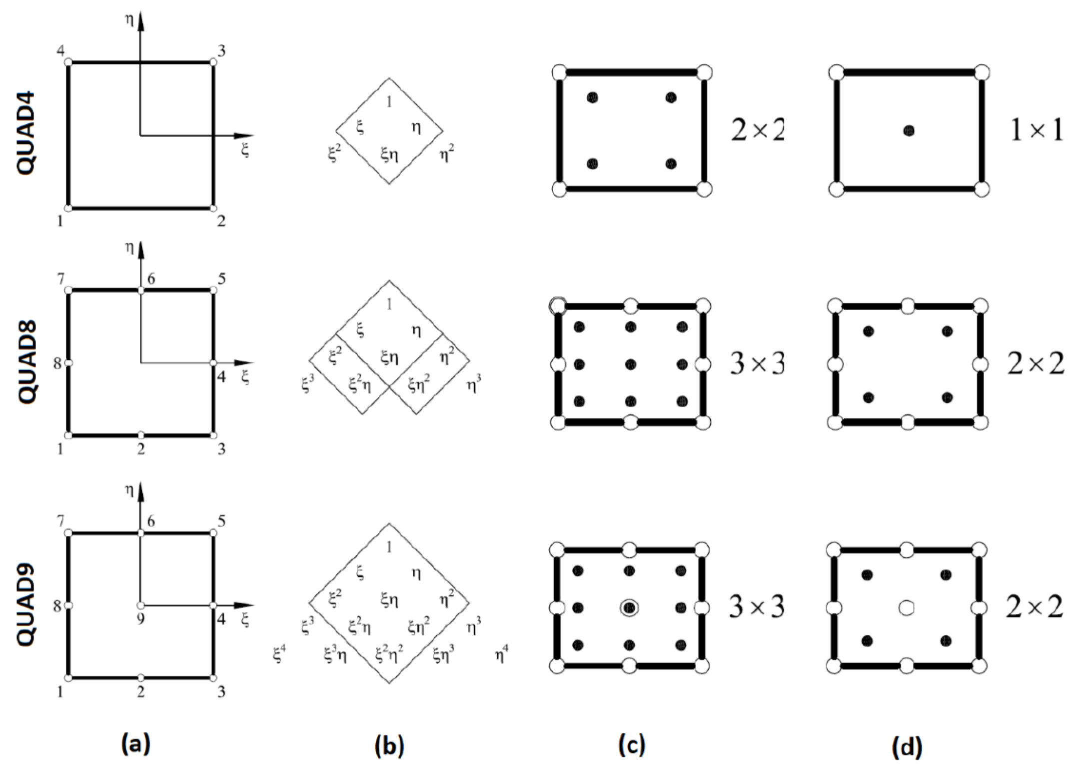

Figure 6.2 *Quadrilateral element type in natural coordinates (ξ, η), (b) Polynomial terms contained in the shape functions from Pascal's triangle, (c) Maximum number of Gauss*

In this thesis, the QUAD4 elements using 2x2 Gauss are selected for the following reason:
1) The purpose of this thesis is not to design a bridge properly. Rather than testing stresses or deflection limits, we're more interested in validating a damage detection approach. As a result, the shear locking effect, which leads to reduced bending displacements, is not a concern in this scenario.
2) The bridge modelling is a system with large degrees of freedom. Therefore, the computational cost would increase enormously if using quadratic isoparametric elements. Moreover, considering that a wide range of damage scenarios, temperature conditions, and load velocities are tested, the choice of QUAD4 are preferable regarding the calculation time, especially, when preforming a time-history analysis.
3) Although the mathematical formulation of quadratic elements (QUAD8 and QUAD9) has been implemented in the Python scripts for this benchmark, the creation of a mesh using these elements is still not coded.
4Because the selected reduced integration method is not available in the Python scripts, a 2x2 GQ scheme was used for the number of Gauss points. As a result, the shear component of the elemental stiffness matrices cannot be evaluated at a single Gauss point, but the bending component uses a complete integration approach.

In conclusion, the most convenient choice is to use QUAD4 elements with 2x2 GQ rule and a mesh size of 0.05m x 0.05m in terms of computational cost and accuracy in vertical displacements. Therefore, as shown in **Figure 6.3** the model is discretized in 400 and 12 elements in x and y directions, respectively, resulting in 4800 elements and 5213 nodes in total (10426 DOFs).

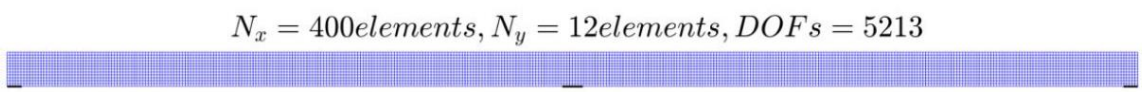

Figure 6.3 *FE mesh of the numerical bridge*

6.2.4 Damage scenarios and sensors

Structural damage in FE models usually is assumed as a reduction of bending stiffness which causes a change in of the dynamic behaviour. In this study, “cracks” on the beam surface are considered. They are modelled by reducing Young’s modulus at the Gauss points on particular the finite elements.

Six sensing points called “sensors” are considered to provide information about the nodal variables in both *x* and *y* directions (i.e., displacements, velocities, accelerations, strains, etc.). The location of these sensors is described in the **Table 6.3**. The six selected sensors are shown as green points in **Figure 6.4**

Table 6.3 *Sensors’ locations along the bridge*

Sensors	Location along the neutral axis (y=0.3m)
S01	x = 2.5 m
S02	x = 5.0 m
S03	x = 7.5 m
S04	x = 12.5 m
S05	x = 15.0 m
S06	x = 17.5 m

Furthermore, six damage scenarios are provided by the benchmark.

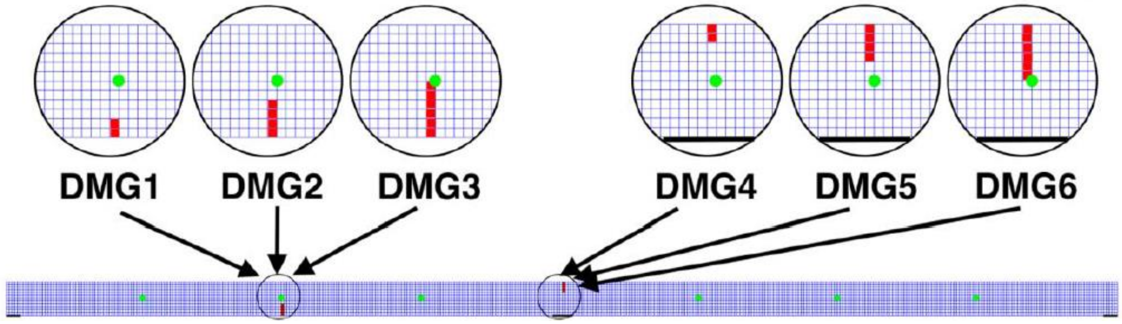

Figure 6.4 *Sensors (in green) and damage locations (in red) in bridge structure*

The first damage region is found in the centre of the left span (DMG1, DMG2, DMG3), starting from the bottommost edge of the beam cross section, while the second damage region is found in the intermediate support section (DMG4, DMG5, DMG6), starting from the uppermost edge of the beam. Besides, the number of damage-induced mesh elements also varies as shown in **Figure 6.4**. For instance, DMG1 and DMG4 cover an area of two damaged elements, DMG2 and DMG5, a zone of four damaged elements, while DMG2 and DMG6, a zone of six damaged elements. Therefore, the damaged elements have a width of 0.05m and the height ranges from 0.1 to 0.3m. The description of these six damage scenarios is summarized in **Table**

Table 6.4 *Damage scenarios provided by the benchmark*

Damage scenarios	Number of damaged elements	Damaged location
Undamaged (UND)	0	
Damaged 1 (DMG1)	2	At 1/2 L_1 from left-hand support, starting from the bottommost edge
Damaged 2 (DMG2)	4	
Damaged 3 (DMG3)	6	
Damaged 4 (DMG4)	2	At L_1 from left-hand support, starting from the uppermost edge
Damaged 5 (DMG5)	4	
Damaged 6 (DMG6)	6	

In addition to the damage scenarios, benchmark model allows to control the severity of the damage by setting the reduction of the Young's modulus given damage scenario at a given location.

In this thesis, stiffness reduction will be noted by **D** followed by the amount of reduction. For example, **D50%** means 50% reduction in Young's modulus at given element and damage scenario.

6.3 Modal analysis

To understand the vibration characteristics of the complex structures, particularly multi-degree-of-freedom (MDOF), the modal analysis must be performed. Furthermore, the continuous analysis of modal characteristics such as natural frequencies, mode shapes, and modal damping ratios might help to detect a structural weaknesses or defects caused by damage [ref]. As an engineer, one must be aware of all possible bridge vibration modes as well as the significance of each mode. It's especially important to avoid resonant vibrations when the loading frequencies coincide with the bridge's natural frequencies [ref]. This occurrence can result in catastrophic damage or structural failure (i.e., the Tacoma Narrows Bridge [ref]).

6.3.1 Mass-normalized mode shapes

To represent the free-vibration solutions of the structure harmonic motion (i.e., mode shapes and natural frequencies), the following equation for a MDOF system must be solved

$$M\ddot{U} + KU = 0$$

The equation above can be transformed into (67) if the non-trivial solution of (66) is the harmonic solution of the form $U = \phi sin\ (\omega t)$, where ω is the circular natural frequency and ϕ the mode shapes.

$$(K - \lambda M)\phi = 0$$

This equation forms the basis for the generalized eigenproblem, where λ are the eigenvalues (with $\lambda = \omega^2$) and ϕ are the eigenvectors (or mode shapes).

Therefore, each eigenvalue and eigenvector represent a free vibration mode of the structure [ref]. The eigenvalue λ_i is related to the i-th natural frequency (in Hz) as follows

$$f_i = \frac{\omega_i}{2\pi} = \frac{\sqrt{\lambda_i}}{2\pi}$$

Regarding the extraction of the eigenvalues and eigenvectors, the Lanczos method is used to solve (67) according to the Python scripts associated to the numerical bridge.

Figure 6.5 demonstrates that the vibration modal solutions of an isotropic rectangular plate are based on sinusoidal functions. These functions can be even [cosine: f(-x) = f(x) ∀x] or odd [sine: f(-x) = - f(x) ∀x], leading to a spatial symmetry or asymmetry regarding the center of the plate in both x and y dimensions. This spatial property has an impact on the corresponding eigenvalues and hence on the modes of vibration represented by the corresponding eigenvectors.

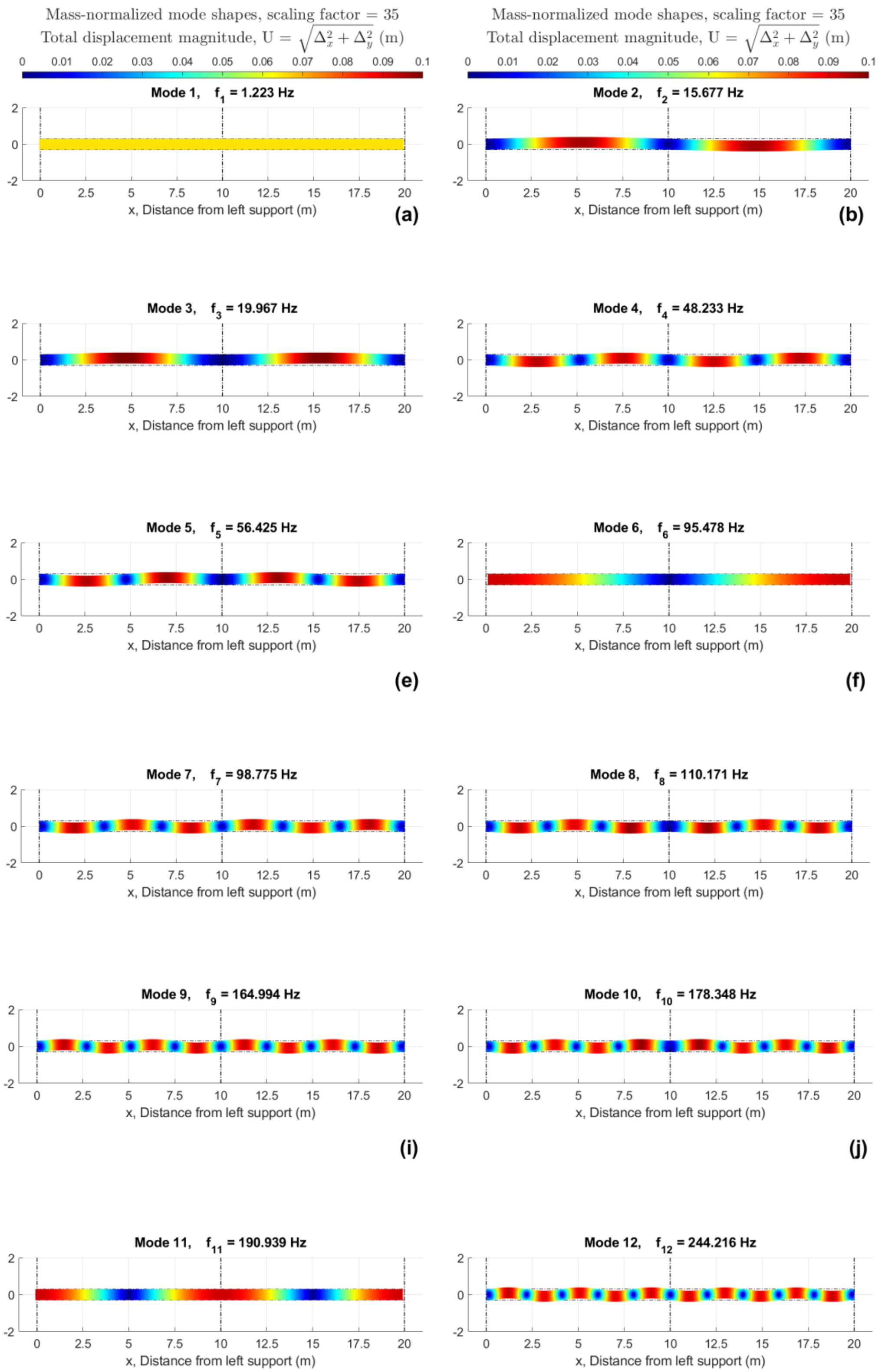

Mass-normalized mode shapes, scaling factor = 35
Total displacement magnitude, $U = \sqrt{\Delta_x^2 + \Delta_y^2}$ (m)
0 0.01 0.02 0.03 0.04 0.05 0.06 0.07 0.08 0.09 0.1
Mode 1, f_1 = 1.223 Hz
Mode 2, f_2 = 15.677 Hz
Mode 3, f_3 = 19.967 Hz
Mode 4, f_4 = 48.233 Hz
Mode 5, f_5 = 56.425 Hz
Mode 6, f_6 = 95.478 Hz
Mode 7, f_7 = 98.775 Hz
Mode 8, f_8 = 110.171 Hz
Mode 9, f_9 = 164.994 Hz
Mode 10, f_{10} = 178.348 Hz
Mode 11, f_{11} = 190.939 Hz
Mode 12, f_{12} = 244.216 Hz
x, Distance from left support (m)
(a)
(b)
(e)
(f)
(i)
(j)

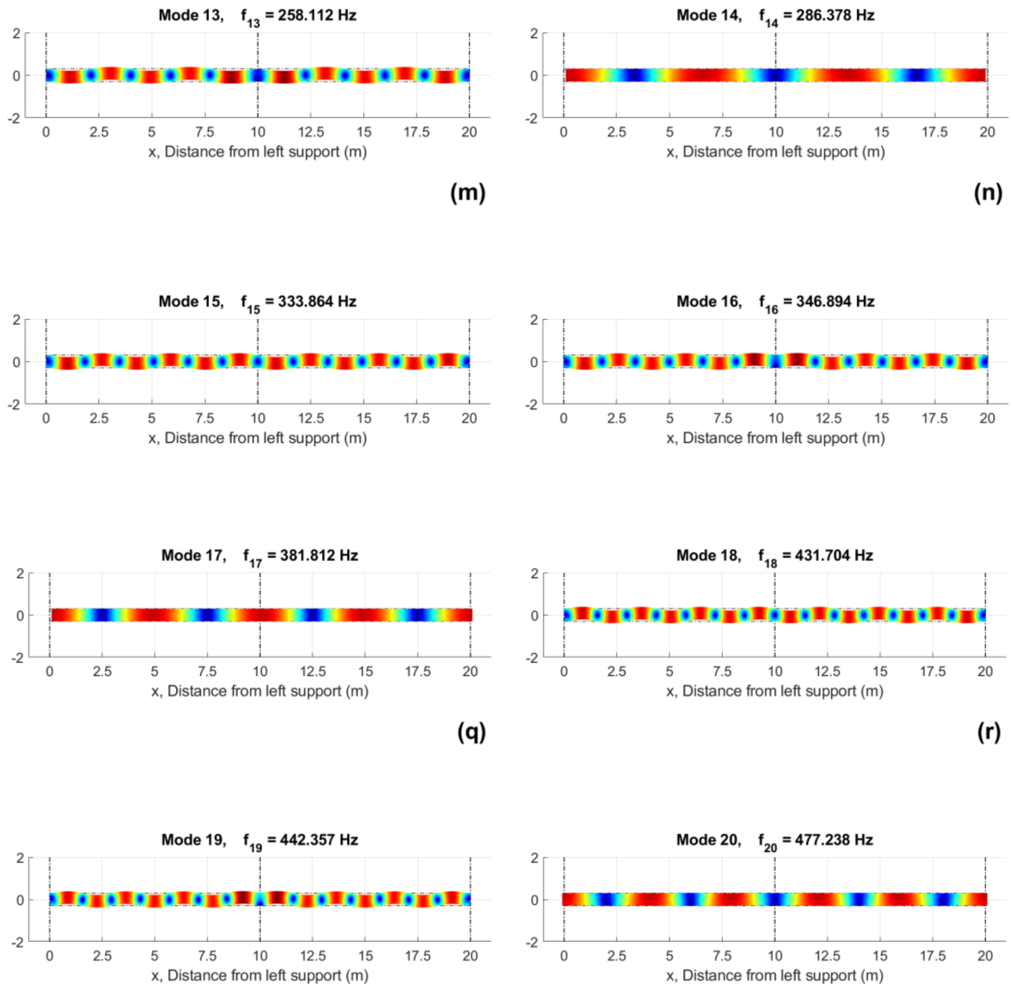

Figure 6.5 *The first 20 natural frequencies and mass-normalized mode shapes using a scaling factor of 35.*

6.3.2 Natural frequencies and EMPFs

The effective mass participation factor (EMPF) represents quantity of the system mass Two translations are allowed in this study: one in the longitudinal x direction and the other in the vertical y direction. The direction dependent EMPF provides a measure of the energy contained within each resonant mode. As a result, the greater the EMPF of a mode, the greater its contribution to the dynamic response. EMPF is noted as $\boldsymbol{\Gamma}_{i,j}$ and can be expressed as follows:

$$\mathbf{\Gamma}_{i,j} = \frac{\phi_j^T M r_i}{\phi_j^T M \phi_j} * 100\ [\%]$$

$\mathbf{\Gamma}_{i,j}$ – is the EMPF of the j-th mode for the translation i,
(It depends on both the direction of the translation and the normalization method used for mode shapes)
M – is the mass matrix
ϕ_j – is the eigenvector of the j-th mode, where $\phi_j^T M \phi_j$
r_i – influence vector which represents the displacement resulting from a static unit ground displacements in the direction i of the translation.

Table 6.5 *The first 20 natural frequencies with their corresponding EMPF*

Mode j	Natural frequency [Hz]	Description of the k-th mode shape		Effective Mass Participation Factor (EMPF), $\mathbf{\Gamma}$	
				$\mathbf{\Gamma}_x$ [%]	$\mathbf{\Gamma}_y$ [%]
1	1.223	1st LT mode	Asymmetric	~100	5.42E-23
2	15.677	1st VB mode	Symmetric	1.42E-06	9.16E-22
3	19.967		Asymmetric	7.63E-23	71.59344
4	48.233	2nd VB mode	Symmetric	1.31E-06	2.38E-23
5	56.425		Asymmetric	5.43E-25	0.151791
6	95.478	1st LT mode	Symmetric	1.90E-24	0.002314
7	98.775	3rd VB mode	Symmetric	1.69E-08	1.46E-24
8	110.171		Asymmetric	4.58E-29	12.24757
9	164.994	4th VB mode	Symmetric	3.93E-08	7.94E-26
10	178.348		Asymmetric	6.00E-27	0.12413
11	190.939	2nd LT mode	Asymmetric	5.68E-08	3.24E-28
12	244.216	5th VB mode	Symmetric	1.32E-09	1.15E-28
13	258.112		Asymmetric	9.77E-28	4.92399
14	286.378	2nd LT mode	Symmetric	1.97E-26	0.000372
15	333.864	6th VB mode	Symmetric	4.52E-09	9.14E-27
16	346.894		Asymmetric	4.79E-28	0.109547
17	381.812	2nd LT mode	Asymmetric	2.08E-08	9.16E-27
18	431.704	7th VB mode	Symmetric	2.22E-10	2.78E-26
19	442.357		Asymmetric	1.54E-28	2.801701
20	477.238	3rd LT mode	Symmetric	1.12E-26	0.002224
SUM				~100%	~91.95708%

LT – Longitudinal Translation
VB – Vertical Bending

6.4 Time history analysis

The numerical bridge is subjected to transient loads induced by a moving vehicle. The implicit Newmark integration scheme is used to solve the differential equation of dynamic system. The final dynamic response of the structure is then represented by sum of important eigenmodes of the system using the mode superposition approach. The number of significant eigenmodes used to represent the system should be carefully chosen, since the number of eigenmodes influences the program's running time and results.

In this section, the implicit Newmark integration schema is firstly presented. Secondly, the choice of the number of significant eigenmodes is discussed based on their corresponding EMPF values. Lastly, described as well as the moving load modelling.

6.4.1 Implicit Newmark integration schema

In time-history or transient analysis, direct time integration methods are frequently used to solve the time-dependent differential equations of motion (70) representative in structural vibration.

$$M\ddot{u}(t) + C\dot{u}(t) + Ku(t) = f(t)$$

This equation corresponds to the general governing equation system for a damped structure, where $f(t)$ is vector of transient loads, $u(t),\ \dot{u}(t),\ and\ \ddot{u}(t)$ are the vectors of the generalized displacement, velocity, and acceleration, respectively. M, K and C are the global mass, stiffens and damping matrices, respectively. For this case study, C is approximated by a proportional damping as (76).

In direct integration, the Eq. (70) is integrated using a step-by-step procedure that consists of discretizing time domain in a set of discrete time interval, Δt. The term "direct" means that prior to the numerical integration, no transformation of (70) into different forms is carried out [33]. Direct integration methods can be categorized into explicit and implicit schemes.

Explicit schemes compute the solution $u_{t+\Delta t}$ at time $t + \Delta t$ obtained by using (70) at time t, whereas implicit schemes calculate the solution $u_{t+\Delta t}$ at time $t + \Delta t$ by using (70) at time $t + \Delta t$. In other words, explicit methods need a complete historical information of u, $\dot{u}$ and $\ddot{u}$ at time t and before as (71), while implicit methods require knowledge of $\dot{u}$ and $\ddot{u}$ at time $t + \Delta t$ as (72)

$$U_{t+\Delta t} = f\left(U_t, \dot{U}_t, \ddot{U}_t, U_{t-1}, \dots\right)$$

$$U_{t+\Delta t} = f\left(\dot{U}_{t+\Delta t}, \ddot{U}_{t+\Delta t}, U_t, \dots\right)$$

According to Noh et al. [34]explicit methods are usually conditionally stable and are used with very small-time steps for short duration, while for structural vibration solutions mostly implicit schemes are used with larger time steps. In this thesis, the implicit Newark integration schema is used to approximate the solution for the numerical bridge. This method is given by,

$$U_{t+\Delta t} = U_t + \dot{U}_t \Delta t + \left[\left(\frac{1}{2} - \hat{\beta}\right)\ddot{U}_t + \hat{\beta}\ddot{U}_{t+\Delta t}\right]\Delta t^2$$

$$\dot{U}_{t+\Delta t} = \dot{U}_t + \left[(1-\gamma)\ddot{U}_t + \gamma\ddot{U}_{t+\Delta t}\right]\Delta t$$

Where $\hat{\beta}$ and γ are parameters to control the integration stability and accuracy. A value of $\gamma = \frac{1}{2}$ is set for avoiding artificial damping and a value of $\hat{\beta} = \frac{1}{6}$ is taken since the variation of the acceleration of mass in motion is assumed to be linear. The entire Newmark algorithm is presented in **Figure 6.6** which has been modified from FIG in [33]. Note that they used α and δ instead of $\hat{\beta}$ and γ, respectively.

Therefore, the velocity field determined from a definite integral of acceleration will be quadratic and hence the displacements field will present a cubic form as shown in **Figure 6.7**

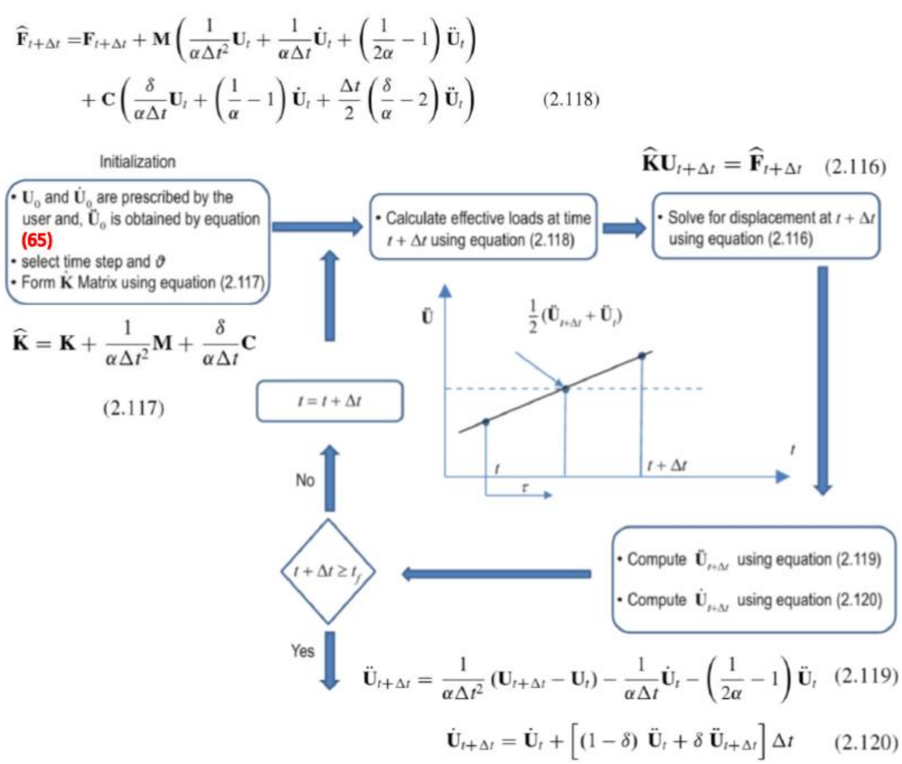

Figure 6.6 *Implicit Newmark algorithm, modified from [33]*

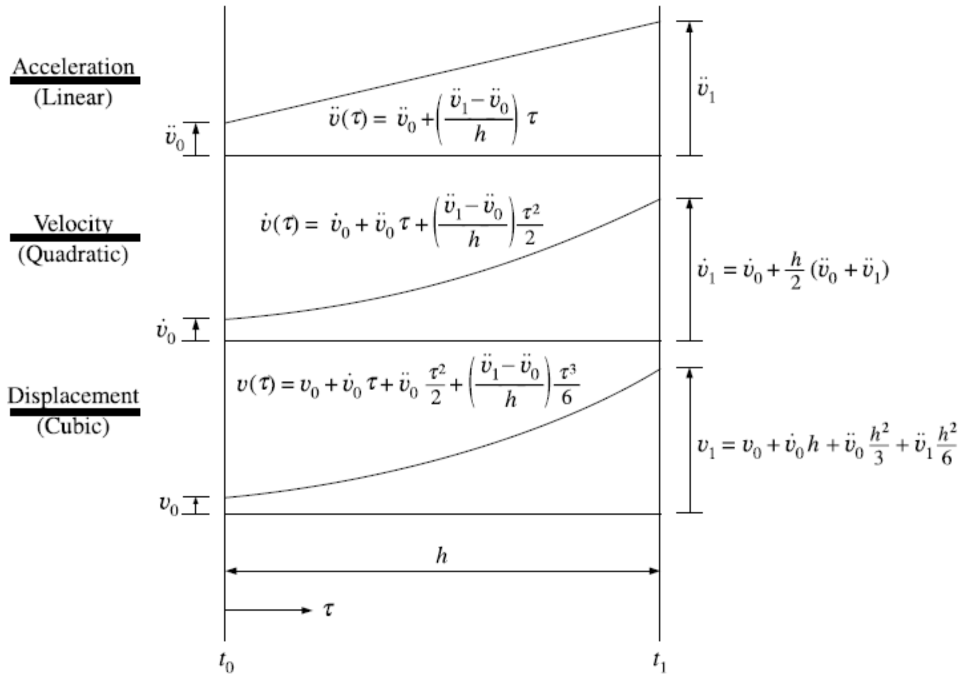

Figure 6.7 *Motion assuming a linear variation of acceleration extracted from [35]*

The Newmark's method using $\gamma = \frac{1}{2}$ and $\hat{\beta} = \frac{1}{6}$is called Newark's linear acceleration method and it is conditionally stable [33].

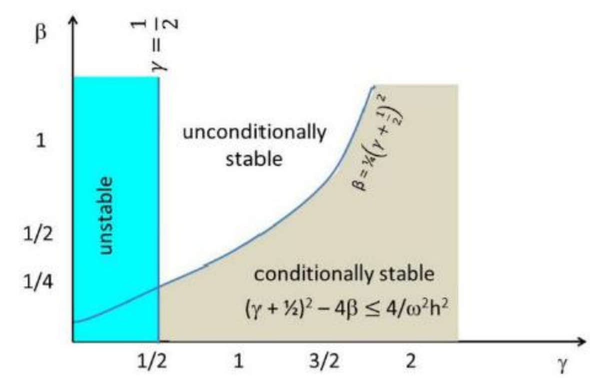

Figure 6.8 *Stability conditions for implicit Newmark method, extracted from [35]*

It can be deduced from **Figure 6.8** that the Newmark-$\hat{\beta}$ method is stable if the time step Δt to solve the differential equations of motion fulfils the following condition:

$$\Delta t \leq \frac{1}{\omega_{max}} \sqrt{\frac{4}{(\gamma + \frac{1}{2})^2 - 4\beta}}$$

where ω_{max} is the maximum angular frequency among the modes of vibration that has been considered for the calculation.

6.4.2 Mode superposition technique

In this study, the mode superposition technique consists of selecting the most representative modes that enables us to reproduce an accurate dynamic behavior of the structure. Do not confuse this technique with the mode superposition method that is used to solve the equilibrium equations instead of the direct integration schemes.

In this case study, only vertical bending modes are considered, thus the longitudinal modes 1, 6, 11, 14, 17 and 20 are disregarded (see **Figure 6.5**). As described in earlier, each *k*-th bending mode can be either symmetric or asymmetric. The number of bending modes to be considered will depend on their cumulative EMPF. Therefore, the 1st in-plane bending mode of vibration corresponding to modes 2 and 3 has a cumulative EMPF of 71.59% (see **Table 6.6**). The 1st and 2nd bending corresponding to the pairs of modes (2,3) and (4,5), respectively, have a similar cumulative EMPF of about 71.75%. The 1st, 2nd and 3rd bending modes have a cumulative EMPF of 83.99%. The first four bending modes have a cumulative EMPF of 84.12%; the first five BM modes, a cumulative EMPF of 89.04%; the six BM modes, a cumulative EMPF of 89.15%; and lastly the first seven BM modes, a cumulative EMPF of 91.95%. These values are summarized in **Table**

Table 6.6 *Cumulative EMPF for different group of bending modes*

The first k-th bending modes	"Individual" bending modes	Cumulative EMPF (%)
1	*2, 3*	71.59
2	*2, 3, 4, 5*	71.75
3	*2, 3, 4, 5, 7, 8*	83.99
4	*2, 3, 4, 5, 7, 8, 9, 10*	84.12
5	*2, 3, 4, 5, 7, 8, 9, 10, 12, 13*	89.04
6	*2, 3, 4, 5, 7, 8, 9, 10, 12, 13, 15, 16*	89.15
7	*2, 3, 4, 5, 7, 8, 9, 10, 12, 13, 15, 16, 18, 19*	91.95

Considering only the first two bending modes for the time-history analysis is not advisable since its cumulative EMPF (71.59%) is less than 80% [36] .Therefore, the first three bending modes or more can be considered as their corresponding cumulative EMF are found between 80% and 90%. As a first approximation, the first three bending modes are considered, that is, modes 2, 3, 4, 5, 7 and 8, based on reducing the computational cost. Moreover, once the damping ratios and the load speed are set, a new analysis is carried out to see if more modes are required for the time analysis based on the convergence of the maximum vertical displacements.

In this context, the time step for calculation is Δt=0.001s with $\omega_{max} = \omega_8$=692.24rad/s corresponding to the 8th mode of vibration and by setting γ = 1/2 and $\hat{\beta}$= 1/6. On the other hand, to accurately reproduce a signal it must be sampled at more than twice the highest frequency component of the signal according to the Nyquist-Shannon sampling theorem [37]. Therefore, if the highest frequency is about 110.171 Hz (692.24rad/s), then the sampling rate should be more than 200Hz. Then, a sampling frequency of *fs* = 400Hz is considered to identify all the frequencies corresponding to the selected modes. The half of the sampling rate is then 200 Hz also known as the Nyquist frequency.

6.4.3 Loading

To perform a time-history analysis simulating traffic flow, a deterministic moving load is used. Moving loads are frequently used as an external excitation to predict the dynamic response of bridges and to detect damage. The moving load passes across every section of the bridge, and singularities in the response are discovered when it passes directly over the damaged zone [ref]. Data-processing methods such as the Hilbert Huang Transform can detect these singularities in the signal caused by vibrations created by the moving load (HHT). The passage of a vehicle is modelled as a moving load F with constant speed v in this case study, as shown in **Figure 6.9**. The weight of a standard truck of about 30 tons is considered.

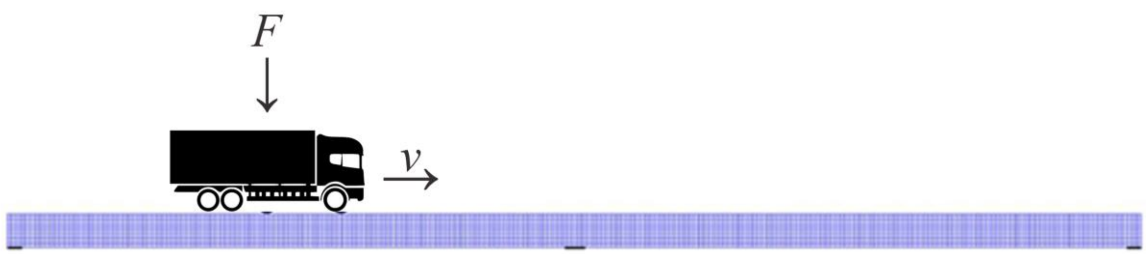

Figure 6.9 *Loading in the form of a moving vertical force F with a constant speed v.*

In conclusion, the following parameters are considered for the time history analysis:
- The 1st, 2nd, and 3rd bending modes are selected
- The Rayleigh damping coefficients are α = 0.1654 and β = 5.4333e-6
- The vehicle velocity is 10 m/s
- A sampling frequency of *fs* = 400Hz, a time step for calculation of Δt=0.001s, a final time step T_f =2s and the number of time samples is 800.

6.5 Temperature simulation

The numerical benchmark allows modelling the temperature and Young's modulus relationship. For this study, the work by Yubo Jiao et al. [38] was assumed as a reference. The relationship between modulus of elasticity and temperature was given:

$$E_c = -0.125T + 29.13$$
$$R^2 = 0.9852$$

However, for this thesis the $E_c = 35GPa$ is taken at reference temperature 20ºC. And the relationship is modified accordingly.

$$E_c = -0.125T + 37.5$$

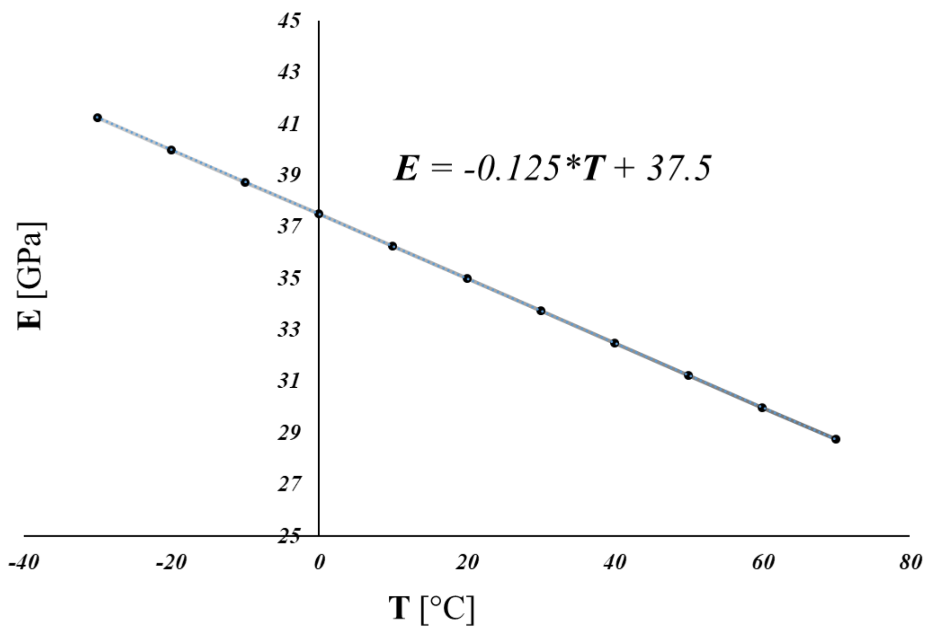

Figure 6.10 *The relationship between modulus of elasticity of a concrete and temperature*

6.6 Results and discussion

As it was stated earlier, the main objective of this thesis is to propose and test the methodology for damage detection in bridges that will be able to distinguish the real damage from the environmental changes. To simulate those conditions, it was decided to model a pseudo-continuous passing of the truck at 2 different temperatures at damaged and undamaged state.

Therefore, the following scenarios for time history analysis were chosen:
1. UND, T=-15°C, D0%
2. UND, T=20°C, D0%
3. DMG3, T=20°C, D90%
4. DMG3, T=-15°C, D90%

In **Figure 6.11** shown recorded accelerations at S01 from simulated benchmark. All the other accelerations from other sensors are provided at **Appendix A**.

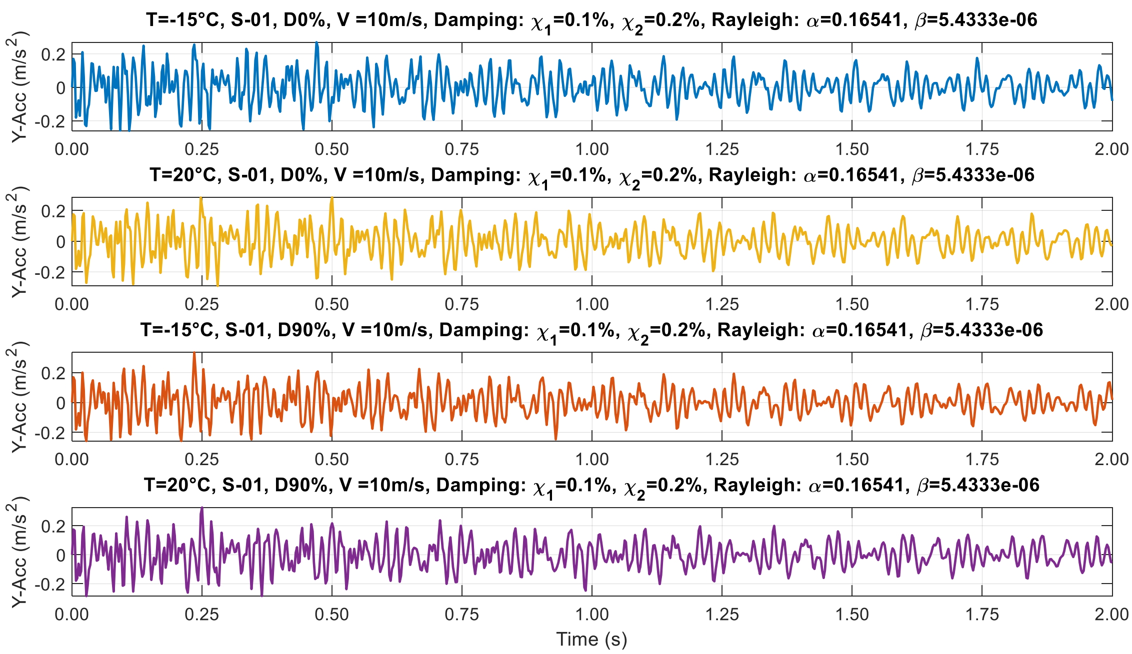

***Figure 6. 11** Recorded Y-accelerations at S01*

6.6.2 VMD

In this section, VMD signal decomposition techniques with its own experimental parameters, are evaluated on a set of 24 time series obtained from six sensors, of which 12 time series correspond to 2 damage scenarios for each group of damage and the 12 series correspond to the undamaged state.

For convenience, the vertical acceleration time series recorded in sensor S01 for the undamaged state at T=20°C is taken as a reference case, as shown in **Figure 6.12**. Therefore, all the experimental results obtained from each mode decomposition technique are related to the undamaged configuration and sensor S01.

Moreover, since the IMFs reveal the frequency information contained in the original signal, the peaks in the Fourier spectrum of this signal gives a rough indication of the number of IMFs to be extracted from a particular signal decomposition technique. Therefore, the single-sided amplitude spectrum of the decomposed IMFs is also discussed in the following sections. **Figure 6.13** represents Fourier spectrum of the original signal whose peaks represent the first three bending modes of vibration, including the asymmetric and symmetric modes

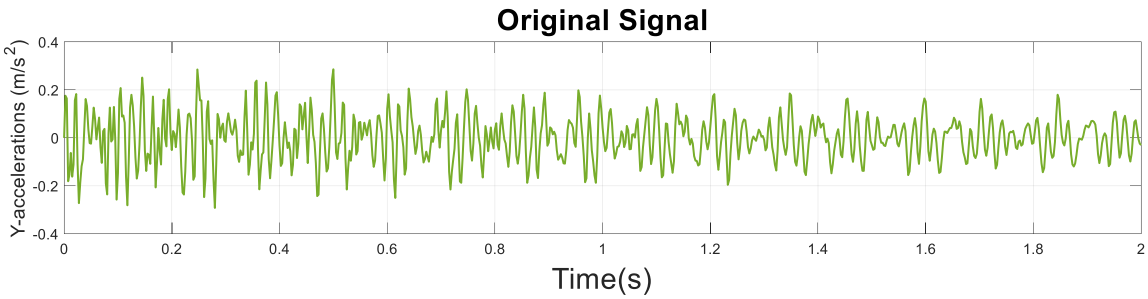

Figure 6.12 *Vertical time-history response for the undamaged state at T=20°C*

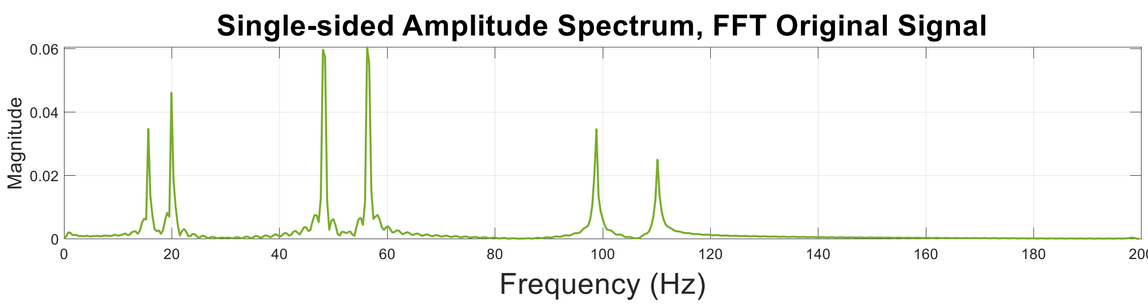

Figure 6.13 *FFT applied to the original signal for the undamaged state at T=20°C, sensor S01*

Variational Mode Decomposition is implemented using standard VMD code provided by MATLAB. There are six parameters that must be set to apply VMD $\varepsilon_a, \varepsilon_r, O, \alpha, \tau$ and K. ε_a and ε_r are absolute and relative tolerance respectively. In this case study the absolute tolerance is more restrictive than the relative tolerance, as in the implementation of MATLAB. Therefore, $\varepsilon_a = 0.1$ and $\varepsilon_r = 10^{-5}$. High number of iterations $O = 100000$ is set to stop the VMD only when relative tolerance is met.

The penalty factor α corresponds to the reconstruction accuracy. The bigger the value of α is, the faster the attenuation is on both sides of the center frequency. It is mainly determined according to the principle of avoiding aliasing between mode functions and is generally 1/6~2 times sampling frequency, $f_s = 400\,Hz$ [39]. It is specific value should be

determined depending on the characteristics of the signal. Different values of the are tested in this section.
The number of K must be determined in advance. However, there is no unified criterion or method to determine the value K so far. Shoujun Wu et al [39] divides into 3 categories the available methods to determine IMF number in VMD: (1) methods based on the center frequency observation, (2) methods based on threshold criteria, and (3) other methods. A high number of the K may cause the overlaps among the model central frequencies, whereas too small K may render the decomposition inadequate. Since the first three bending modes are considered in this case study, including asymmetric and symmetric modes, K should be equal or greater than six ($K \geq 6$).

The VMD implementation in MATLAB requires to select method to initialize central frequencies among the 3 options available:

- 'Peaks' to initialize the central frequencies as the peak locations of the signal in the frequency domain (default).

- 'Random' to initialize the central frequencies as random numbers distributed uniformly in the interval [0,0.5] cycles/sample.

- 'Grid' to initialize the central frequencies as a uniformly sampled grid in the interval [0,0.5] cycles/sample.

The main objective of this section is to properly decompose the signals using VMD, finding accurate parameters and a center frequency initialization method.

Here below in the table are shown parameters that were established for each sensor signal.

Table 6.7 *VMD parameters for each sensor*

Parameters	**S01**	**S02**	**S03**	**S04**	**S05**	**S06**
Number of modes, K	6	5	6	6	5	6
Relative tolerance, ε_r	10^{-5}	10^{-5}	10^{-5}	10^{-5}	10^{-5}	10^{-5}
Penalty factor, α	1000	1000	1000	1000	1000	1000
Fidelity coefficient, τ	0.1	0.1	0.1	0.1	0.1	0.1
Absolute tolerance, ε_a	0.1	0.1	0.1	0.1	0.1	0.1
Number of iterations, O	100000	100000	100000	100000	100000	100000

The decomposed signal is shown in **Figure 6.14** below

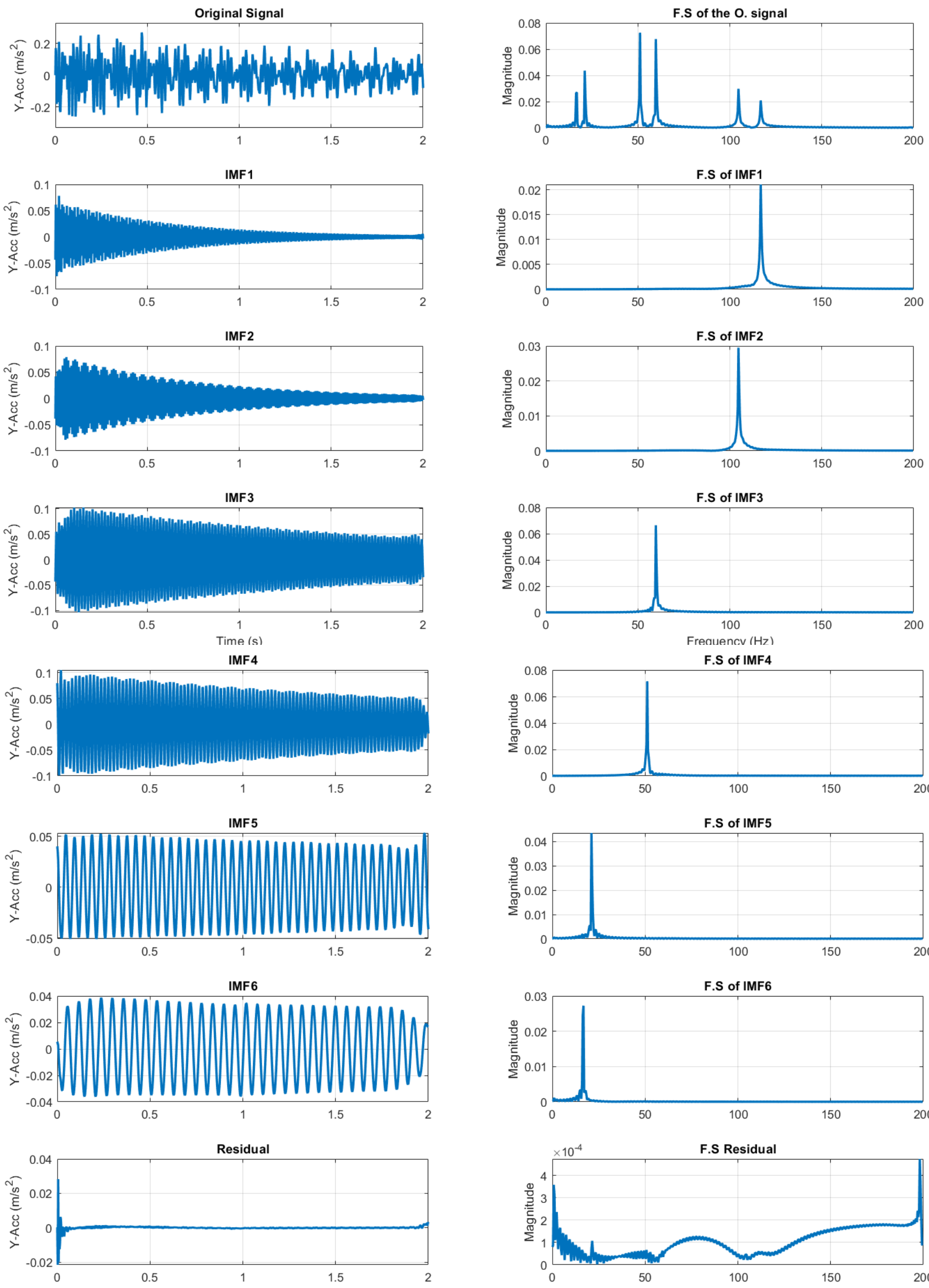

Figure 6.14 *Y-acceleration signal of undamaged state from S01 at T=20°C and its VMD*

The efficiency of the VMD method has been demonstrated. The algorithm always seeks to reconstruct the time series effectively with minimum error. The VMD method ensures no mixture of modes as well as the orthogonality of the transformation. Although, in this section is referred to the signal decomposition for the undamaged state at T=20°C in sensor S-01, the same procedure is performed for all sensors and compared to the damage scenarios. An in-depth study was done for every sensor, damage scenario and group of damage and the results can be found in **Appendix B**. This study revealed that the signal decomposition is similar for every damage scenario using the same VMD parameters as in sensor S01: $\varepsilon_a = 0.1$, $\varepsilon_r = 10^{-5}$, τ=0.1, $\varepsilon_r = 10^{-5}$ and O=100000, with exception of the number of modes K, which varies from one sensor to another as shown in **Table 6.7**.

K is found to be 6 for sensor S01, S03, S04 and S06 which are located at ¼ from the spring supports, whereas K is established as 5 for sensors S02 and S05 which are placed at the middle of the left span and right span, respectively. In these sensor signals the 2nd bending mode is far less than in the rest of the sensors, which causes in a mix of the asymmetric ans symmetric modes as shown in the IMF3 in **Figure 6.15** below.

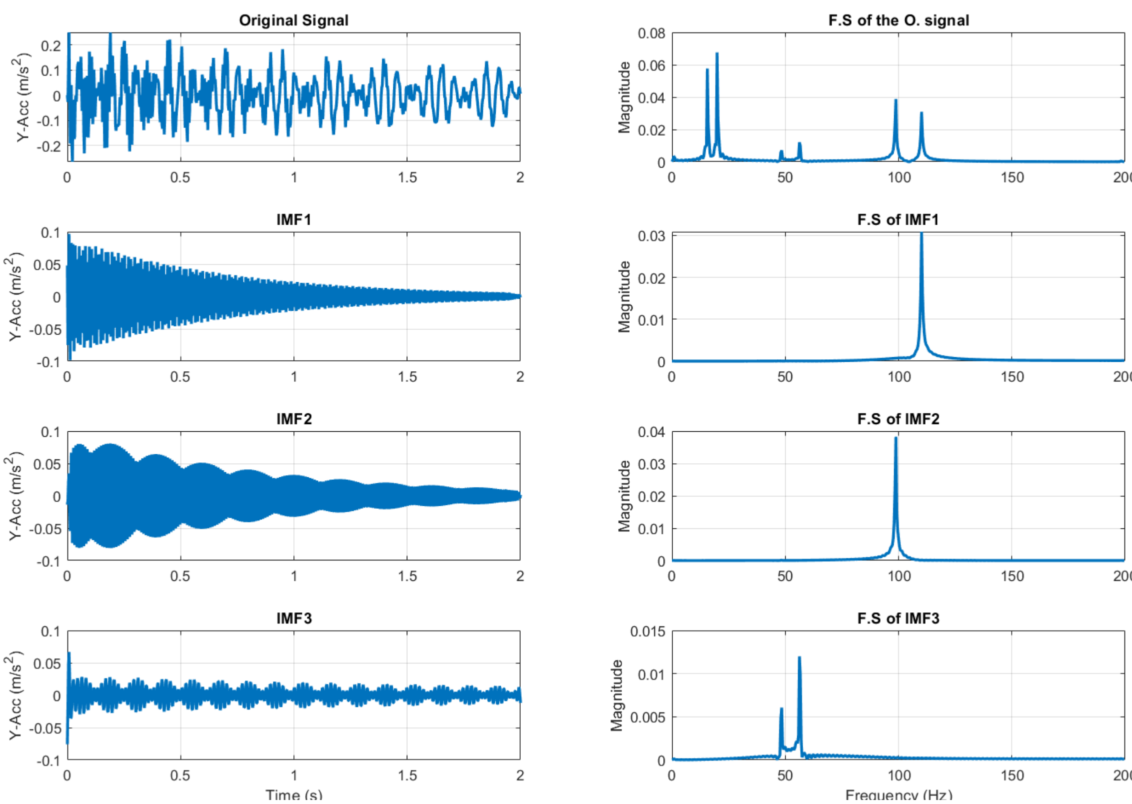

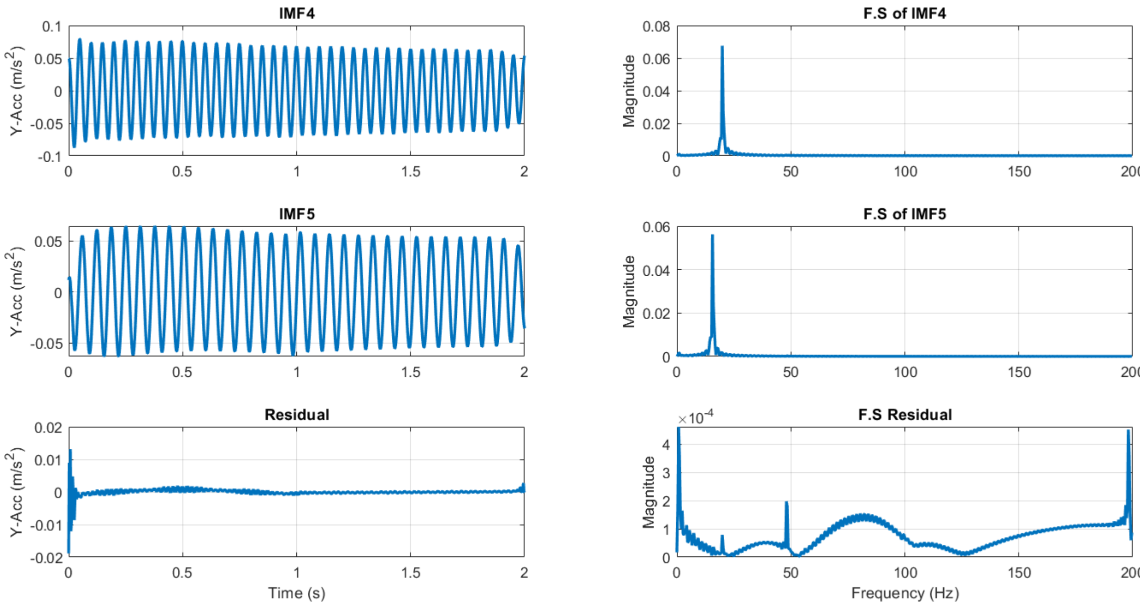

Figure 6.15 *Y-acceleration signal of undamaged state from S02 at T=20°C and its VMD*

The mode mixing could have been avoided by increasing the number of modes K and adjusting some other parameters. However, different spurious modes may uncontrollably appear during the signal decomposition for every damage scenario, resulting in an inadequate comparison of the results. Therefore, a lower order regarding of the expected IMFs is considered for sensors S02 and S05 to accurately decompose the raw vibration signal, that is, K=5.

6.6.3 Application of Hilbert Transform

In this section, the Hilbert transform is applied to study the characteristics of different time-varying parameters obtained from scenarios and to obtain damage sensitive features. In particular, the goal is to examine each IMF and obtain instantaneous frequency as functions of time. It can be achieved by applying the Hilbert Transform (HT) to each IMF extracted from the application of the VMD method.

The instantaneous frequencies $f_k(t)$ are obtained by applying the Hilbert Transform to the k physically meaningful IMFs. The Hilbert spectrum relate $f_k(t)$ with time as the energy can been contoured on the frequency-time plane. Therefore, since structural damages may cause changes in the dynamic parameters, such as the energy (the square of the amplitude of the signal), then the Hilbert spectrum may reveal these damage-induced changes.

MATLAB® [129] uses the *hilbert* function to compute the Hilbert transform for a real time series data, $x(t)$. Hence, running $z(t) = hilbert(x(t))$ will return a complex analytical signal $z(t)$, where the real part of $z(t)$ is the original real data, $x(t) = Re(z(t))$, and the imaginary part is the actual Hilbert transform, $H[x(t)] = Im(z(t))$. On the other hand, MATLAB® uses the hht function to compute the Hilbert-Huang transform for intrinsic mode functions (IMFs). Therefore, for a IMF with a sample length of m and a sampling frequency of Fs, running $hht(IMF(t), Fs)$ will return the Hilbert spectrum (HS), the instantaneous frequencies (in Hz), $imfinsf$, and the instantaneous energies (in (measured unit)^2), $imfinse$, having the same sample length m than the IMF. However, if the instantaneous frequency $f_k(t)$ is noted here as $instafreq$, will be a vector of length $m-1$. When plotting $instafreq$ with time, its values can be located at the middle of each time interval, that is, at $\frac{t_j+t_{j+1}}{2}$. Consequently, by a linear interpolation of the $instafreq$ values, $imsinf$ values are obtained and located at the exact time step t_j and using the first and last $instafreq$ values at t_0 and t_m, respectively. Therefore, both $imfsinf$ and the input $IMF(t)$ have the same vector length. In this section, the $imfsinf$ values (not the $instafreq$ *values*) are used as damage-sensitive features along with the instantaneous amplitudes, $imfinse$.

As mentioned in the previous section, depending on the sensor location, the signal can be decomposed into a different number of IMFs. That is, six IMFs associated to sensors S01, S03, S04, S06 and five IMFs to sensors S02, and S05. Therefore, the results obtained from sensor S01 and S05 are discussed more in detail since they have different behaviour and are located on different sides regarding the center of gravity (GoG) of the bridge. However, a final graph is presented containing the results of the time-varying parameters for all sensors and damage states.

Figure 6.16 illustrates the instantaneous frequency of the physically meaningful IMFs obtained from the undamaged condition of the bridge (upper part) and the damage scenarios (lower part), regarding the sensor S01. It can be noticed that no mode mixing has occurred and that IMF1, IMF2, IMF3, IMF4, IMF5 and IMF6 are clearly in synchronization in terms of frequency content, indicating that they are physically meaningful, representing the third asymmetric, third symmetric, second asymmetric, second symmetric, first asymmetric, and first symmetric vertical bending modes (VB), respectively. On the other hand, no significant difference is graphically observed between the undamaged and damage scenarios, however the temperature change can be clearly noticed. From now on, the 3rd bending mode is referred as the “high”-frequency mode, the 2nd VB mode as the “intermediate”-frequency mode and the 1st VB mode as the “low”-frequency mode. The terms “high”, “intermediate” and “low” are used in order to facilitate the understanding of the results but keeping in mind that the frequency values obtained from this numerical benchmark are much higher than the typical frequencies found in real bridges.

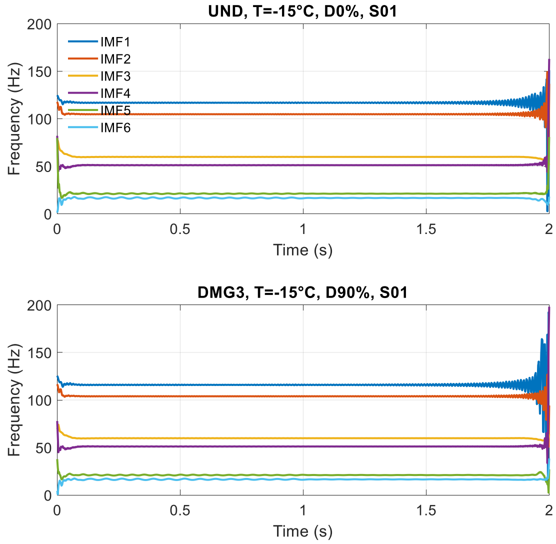

Figure 6.16 Instantaneous frequency for each scenario in sensor S-01.

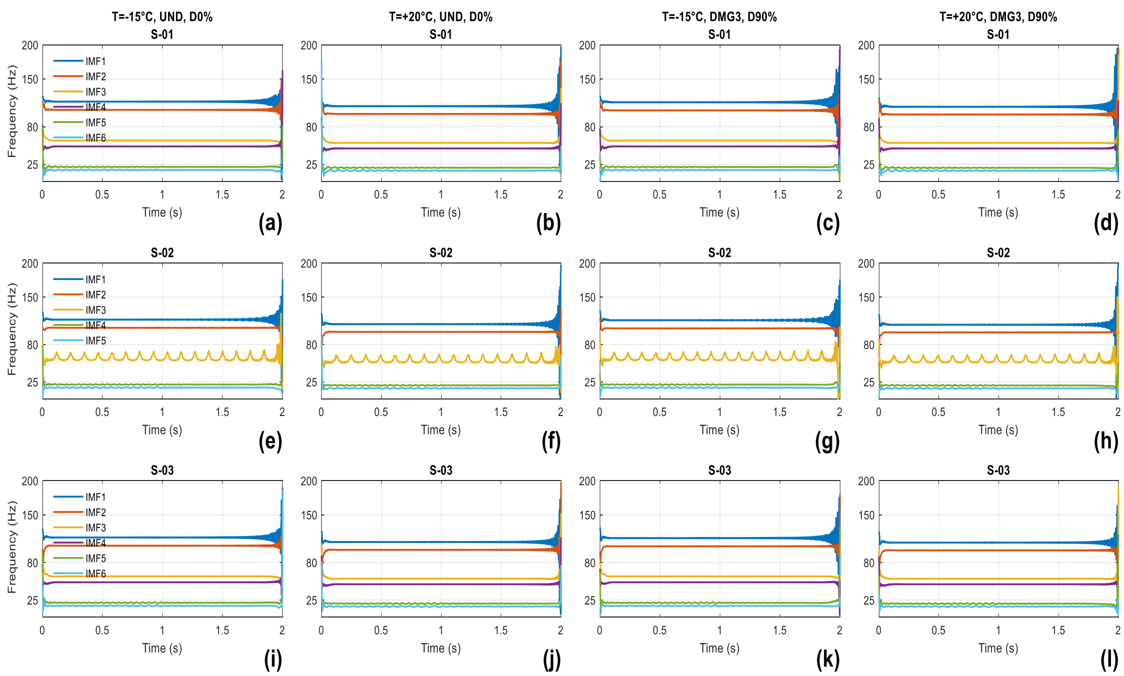

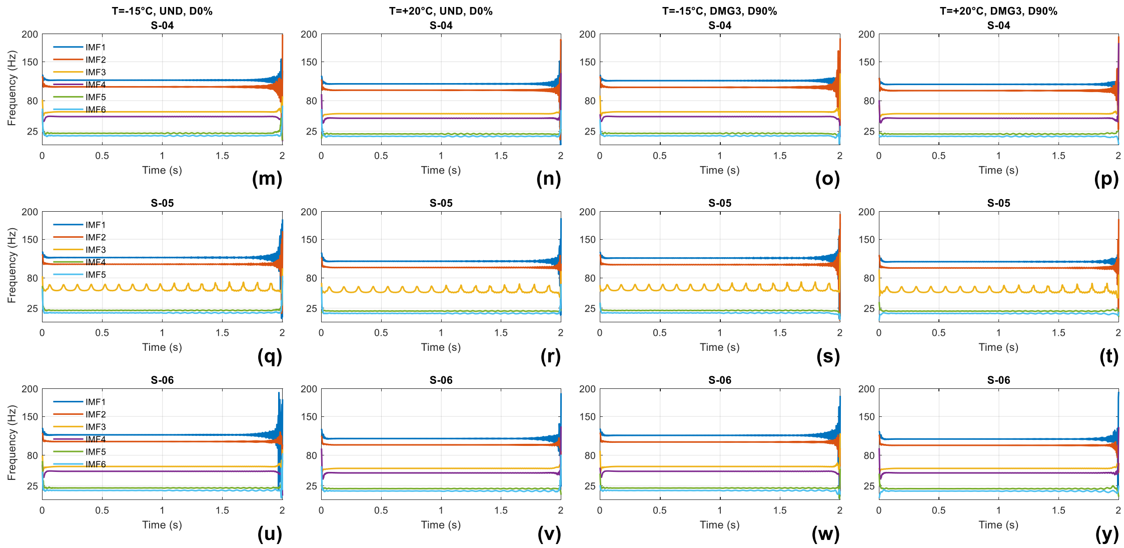

Figure 6.17 *Instantaneous frequency for each sensor (rows) and each scenario*

As it was noticed the boundary conditions, it was decided to take to concatenate the instantons frequencies an only consider in the interval 01.-1.5 sec as shown in figure below.

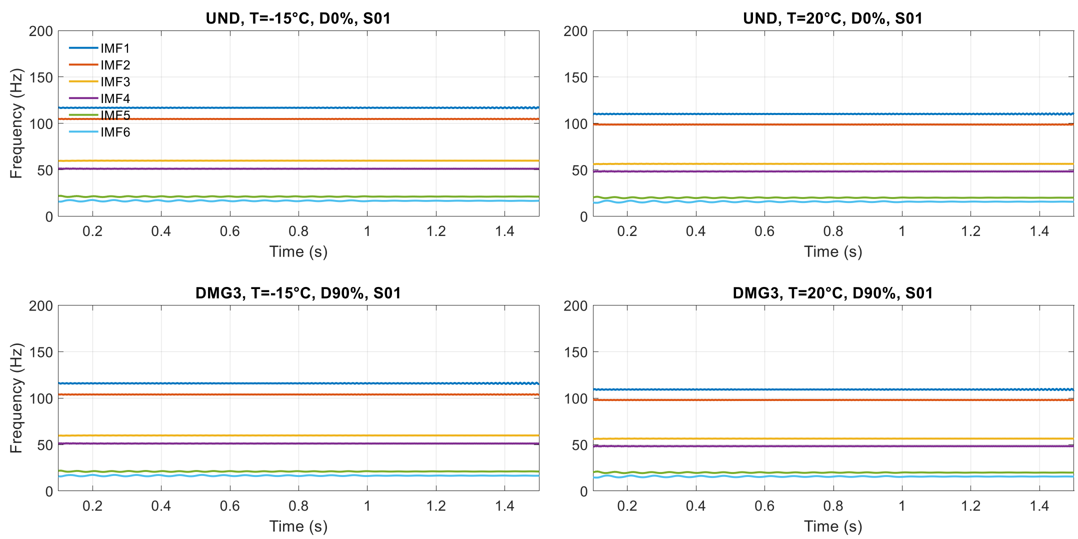

Figure 6.18 *Concatenated instantaneous frequencies for each scenario in sensor S-01.*

6.6.4 Application of PCA

When PCA is applied to the data set, the first principal component (PC1) represents the factor that creates the greatest variance within the data set, the second principal component (PC2) represents the factor that creates the second greatest variance affecting the data, and so on. Soo et al. [27] suggested that to represent the effects of temperature variations in the PC1, the data set must be obtained from two extreme and opposite temperature conditions. Consequently, the extreme cases will be represented on opposite sides in the PC1 graph, showing negative and positive values of the variance if the data set is standardized. Therefore, the other principal components will represent other minor factors affecting the data set such as structural damages.

The PCA methodology to filter the temperature effects affecting the vibration parameters can be divided into eight main steps. **Figure 6.19** shown the flow chart of the proposed method applied to the numerical benchmark.

The first step consists of defining the baseline based on two extreme and opposite temperature conditions. In this case study, these temperatures are taken at -30ºC and 70ºC. For a better performance of the proposed method, the baseline will consist of 8extreme cases including five cases at low temperatures [-30ºC, -29ºC, -28ºC, -27ºC,] and five cases at high temperatures [66ºC, 67ºC, 68ºC, 69ºC and 70ºC].

The second step consists of collecting the damage-sensitive features associated to the undamaged structure under the 8 extreme temperature cases. The vibration features can be either the natural frequencies (NF) of the bridge or the instantaneous frequencies (if) of the IMFs extracted from VMD.

The third step consists of creating the "baseline matrix" of the undamaged structure, noted as B, for each damage-sensitive feature. This matrix consists of *n* rows that indicate the number of extreme temperature cases (*n*=8) and *m* columns representing the number of modes from which the damage feature has been extracted. The number of *m* varies from one damage-sensitive feature to another.

The fourth step consists of adding a new observation to the baseline. That is, adding a new row to the matrix B, resulting in a final matrix Z (n+1 x m), which is referred as "case matrix". Note that this new observation can be obtained at any temperature. On the other hand, this new observation can be obtained either from the undamaged condition of the structure or any other damage scenario.

The fifth step consists of the application of PCA to the matrix Z. However, matrix Z first should be normalized to zero mean and unit variance. Then, the T-scores associated with the principal components can be obtained.

The sixth step consists of plotting the T-scores of every principal component for each study case.

The seventh step consists of analysing PCs. If there are PC that show the temperature effects, they are disregarded.

The eighth step consists of applying inverse PCA to remaining PCs. Moreover, the resulting matrix should be back scaled with to have meaningful damage sensitive features.

The last step consists of repeating procedures 4 to 8 for a new observation if the same damage sensitive feature is studied. In case of switching to a different vibration feature, steps 2 to 8 are repeated.

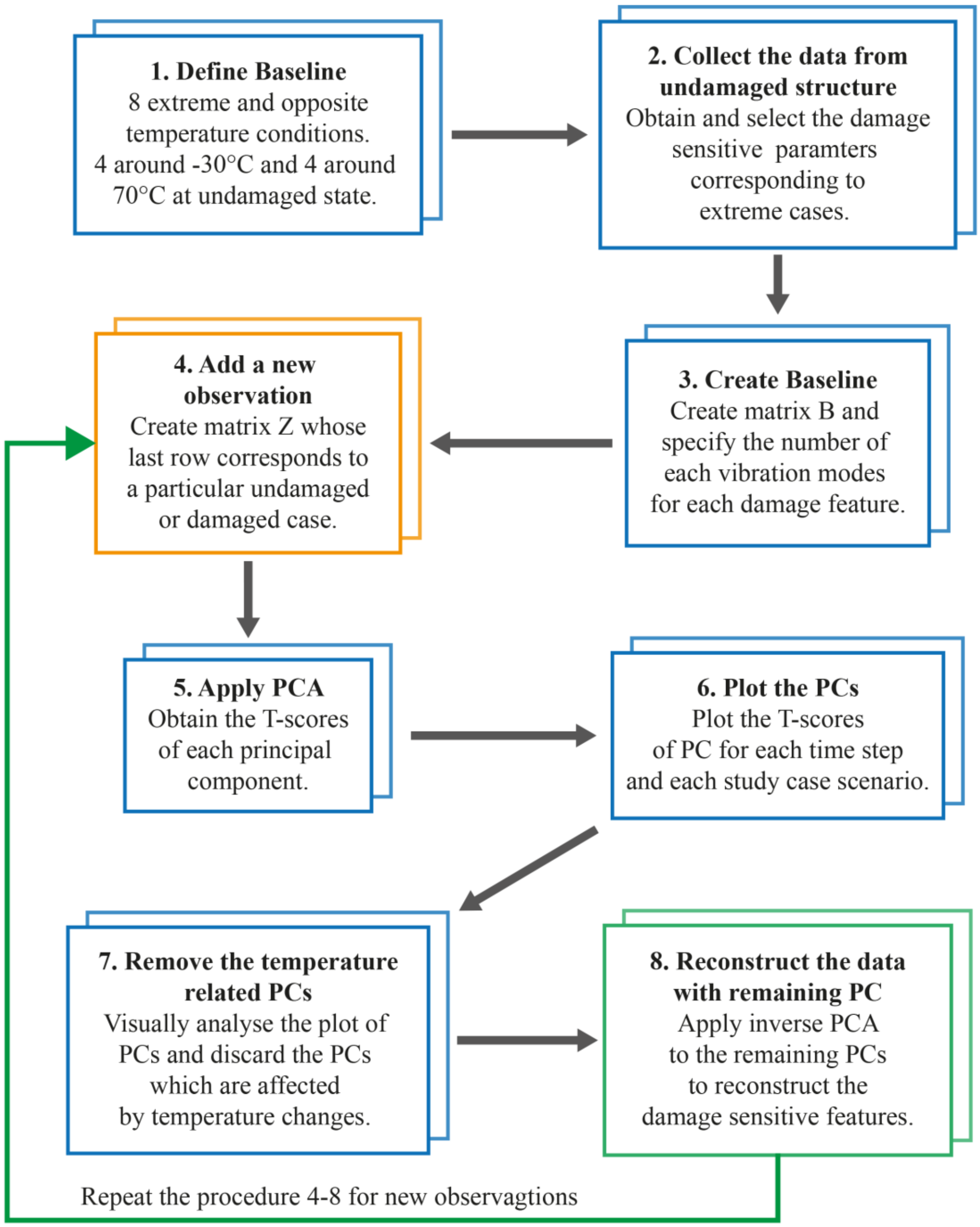

***Figure 6.19** Flow chart of the PCA based filtering method*

The basic data set for typical PCA is a 2-D matrix, $X_{n,m}$, consisting of *n* observations (e.g., temperature variability) and *m* measured variables (e.g., modes). The correlation between these variables is examined using the standard PCA method. However, because the observed variables (e.g., instantaneous frequencies) are continuous in time in this case study, a third dimension, k is added resulting $X_{n,m,k}$.

In this case study, correlations between a particular measured variable (e.g., IF) obtained for each IMF m and several temperature observations n, are analysed. Therefore, each time sample and each sensor are treated independently. As an illustration, **Figure 6.20** shows the unfolding in time samples of the data set corresponding to a sensor resulting in a 2-D data matrix, $X_{n,m,k}$

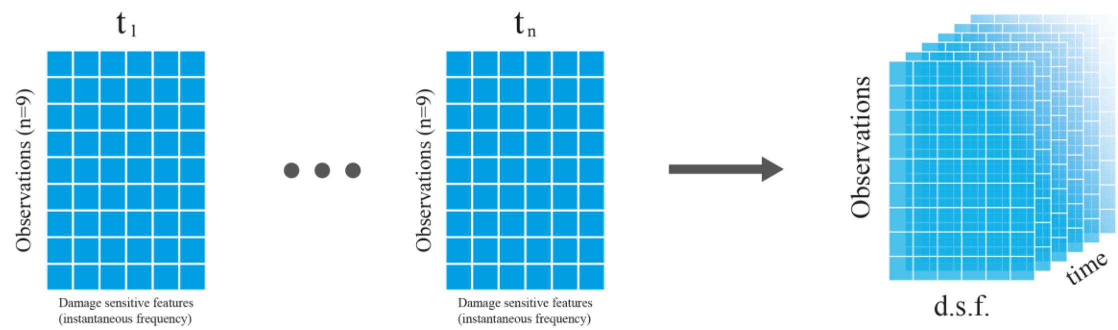

Figure 6.20 *Unfolding of PCA matrix for a sensor*

Moreover, a fourth dimension, l, must be added in the data matrix when various sensors are examined. As a result, a four-dimensional data matrix $X_{n,m,k,l}$ with a high number of connected variables is created, as illustrated in Figure

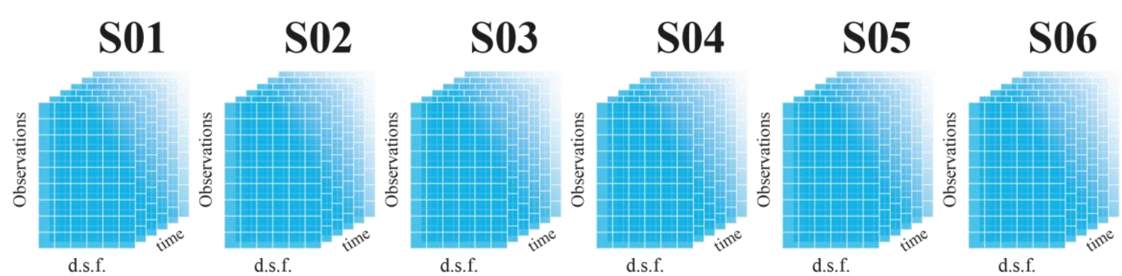

Figure 6.21 *Complete data matrix for PCA*

On one hand, the number of observations is n = 9 corresponding to the 8 extreme cases observations to create the baseline plus one new observation. On the other hand, the number of modes m represents the number of the IMFs in which the original signal has been decomposed. As seen in the previous chapter, the number of the IMFs m varies from one sensor to another: m=6 for sensors S01, S03, S04 and S06, and m=5 for sensors S02 and S05. As a remainder, the instantaneous modal parameters were obtained for the interval 0.1-1.5 seconds and an output time-step size of Δt = 0.0025 seconds (equivalent to a sampling frequency of 400Hz) was selected to capture the first three bending modes of vibration, hence dimension k = 560. The vertical acceleration response obtained for any temperature condition has been decomposed by means of the VMD-based method with the following parameters: $\alpha = 1000$ $\varepsilon_a = 0.1$, $\varepsilon_r = 10^{-5}$, τ=0.1, $\varepsilon_r = 10^{-5}$ and O=100000.

In the following sections, the results for the undamaged cases and damage cases corresponding to scenarios at temperatures of -15ºC and 20ºC are presented. Moreover, to create the baseline, four extreme cases at low temperatures around -30ºC (blue dots) and four extreme cases at high temperatures around 70ºC (red dots) are considered. Furthermore, each scenario case under consideration is represented as black dots.

The instantaneous frequency $x_k(\mathrm{t})$ of each IMF has been determined earlier. illustrates the 6 components for four scenario cases at at of -15ºC and 20ºC (from top to bottom). Furthermore, it can be noted that the magnitude of the observations in the PC1 is much larger than that in the PC2 for all four scenarios.

The motioned cases (black dots) move from the coldest temperature limit (blue dots) to the hottest temperature limit (red dots) when increasing temperature.

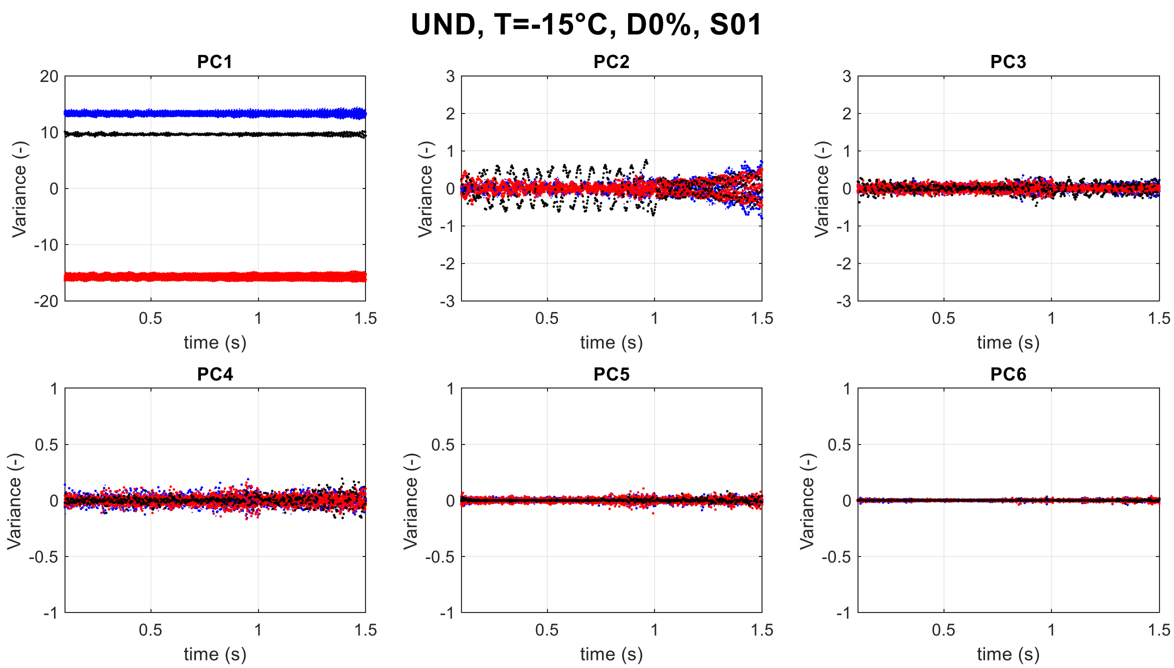

Figure 6.22 *PCA of UND T=-15°C, D0%, S01 (black dots); blue dots – extreme negative temperatures (-30°C, -29°C, -28°C, -27°C); red dots – extreme positive temprestures (67°C, 68°C, 69°C, 70°C)*

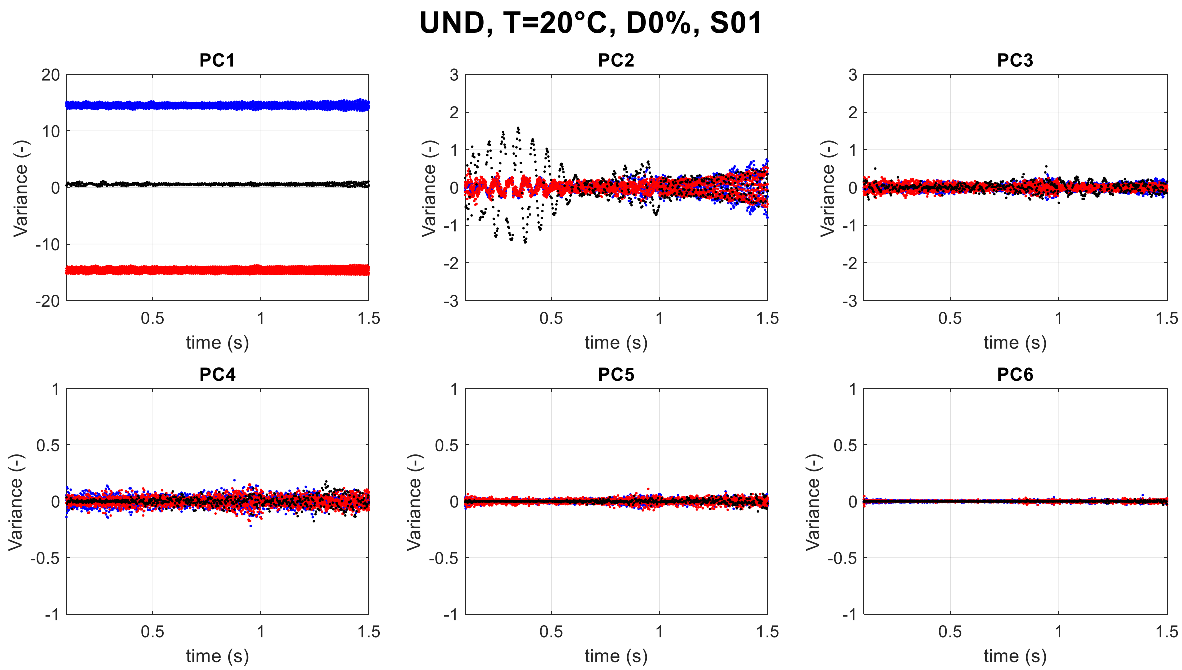

Figure 6.23 *PCA of UND T=20°C, D0%, S01 (black dots); blue dots – extreme negative temperatures (-30°C, -29°C, -28°C, -27°C); red dots – extreme positive temprestures (67°C, 68°C, 69°C, 70°C)*

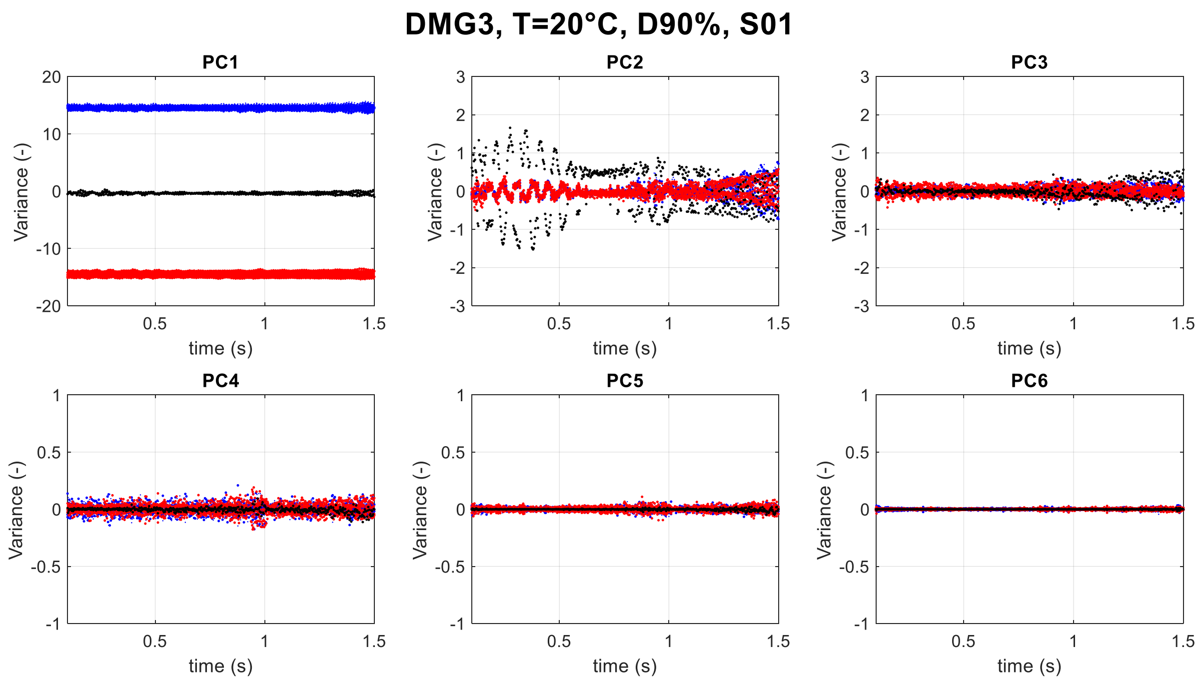

Figure 6.24 *PCA of DMG3, T=20°C, D90%, S01 (black dots); blue dots – extreme negative temperatures (-30°C, -29°C, -28°C, -27°C); red dots – extreme positive temprestures (67°C, 68°C, 69°C, 70°C)*

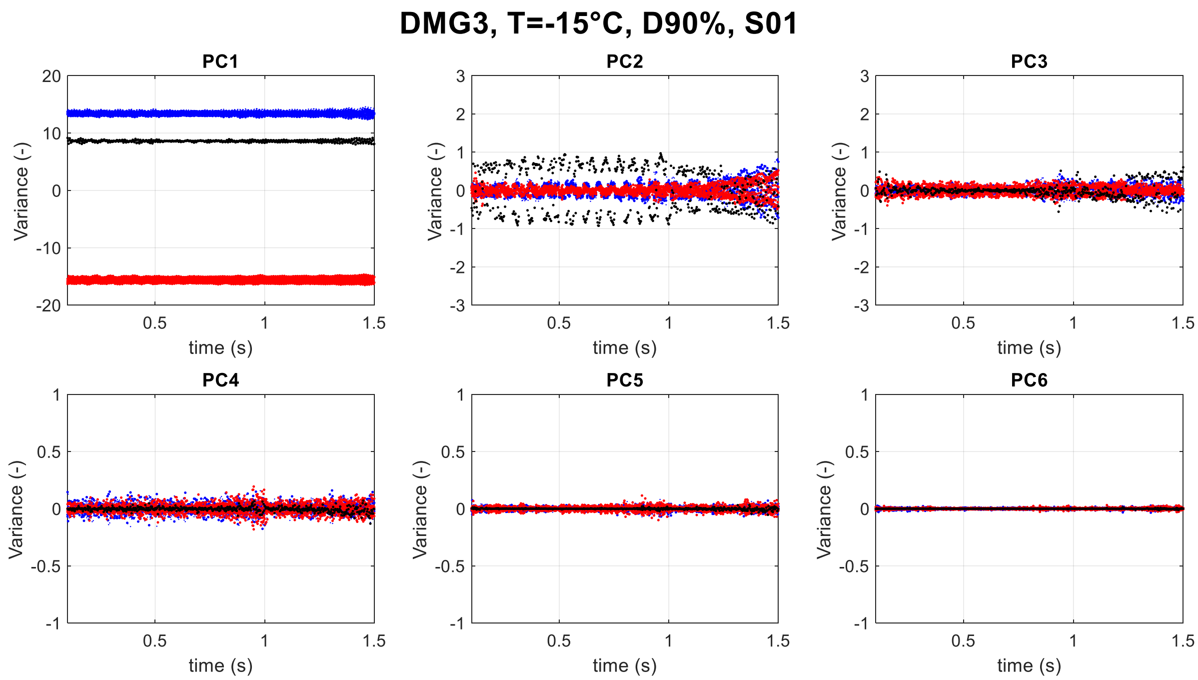

Figure 6.25 *PCA of DMG3, T=-15°C, D90%, S01 (black dots); blue dots – extreme negative temperatures (-30°C, -29°C, -28°C, -27°C); red dots – extreme positive temprestures (67°C, 68°C, 69°C, 70°C)*

As can be seen from **Figures 6.22-6.25** all PC 1 are related to the temperature, moreover they exhibit highest variance in the data. As scenarios under the consideration are at -15°C and 20°C they both fall between extreme cases both in damaged and undamaged cases. Thus, making it clear that the 1st PC is in fact temperature related.

Moreover, it important to note that the PC2 can reveal some changes in the structure response as well. If two cases of damaged and undamaged at T= 20°C are compared, we can see the difference in PC2.

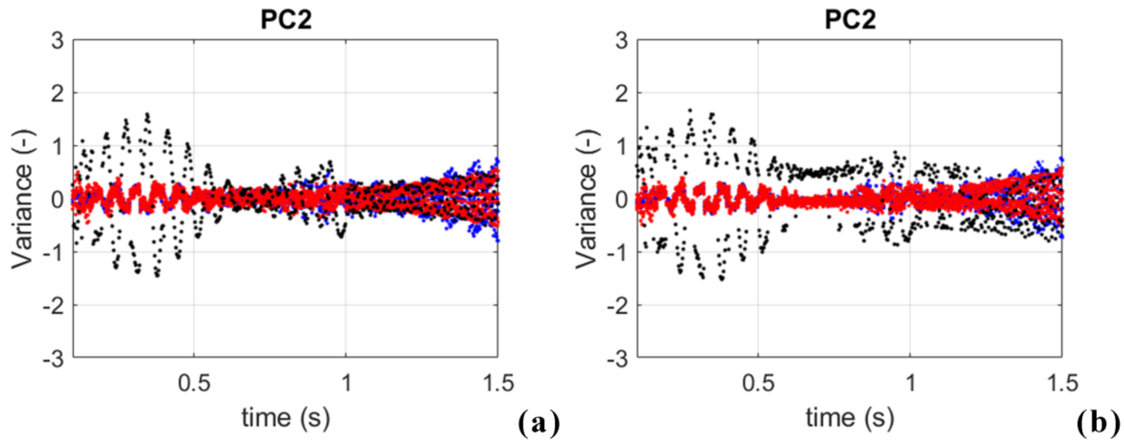

Figure 6.26 *Comparison of the PC2*
(a) *UND T=20°C, D0%, S01 (black dots); blue dots – extreme negative temperatures (-30°C, -29°C, -28°C, -27°C); red dots – extreme positive temprestures (67°C, 68°C, 69°C, 70°C)*
(b) *DMG3, T=20°C, D90%, S01 (black dots); blue dots – extreme negative temperatures (-30°C, -29°C, -28°C, -27°C); red dots – extreme positive temprestures (67°C, 68°C, 69°C, 70°C)*

As a next step, the damage sensitive features (instantaneous frequencies) are reconstructed using 5 last Principal Components (from PC2 to PC6). It worth noting that the reconstructed data should be rescaled to have a physical meaning.

In the **Figure 6.27** below, the IF from all scenarios at S01 is shown before and after application of PCA dimensionality reduction. It is worth noting that IF at 20°C had a slight change in their magnitude as it can be seen from their difference. However, IF at -15°C have shifted up >6 Hz.

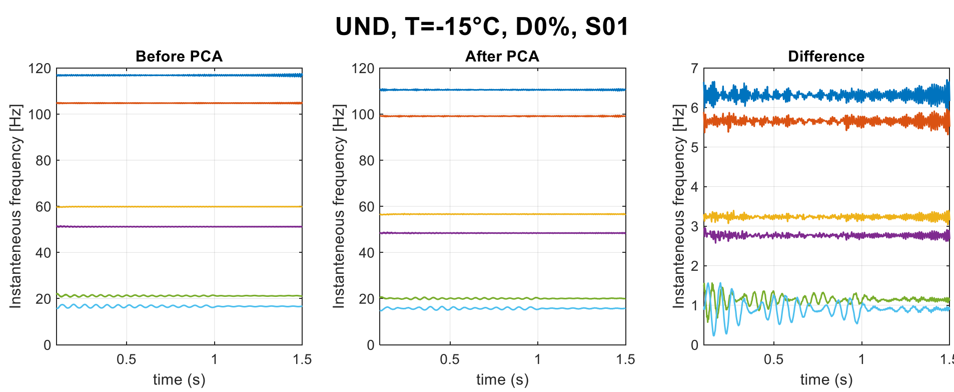

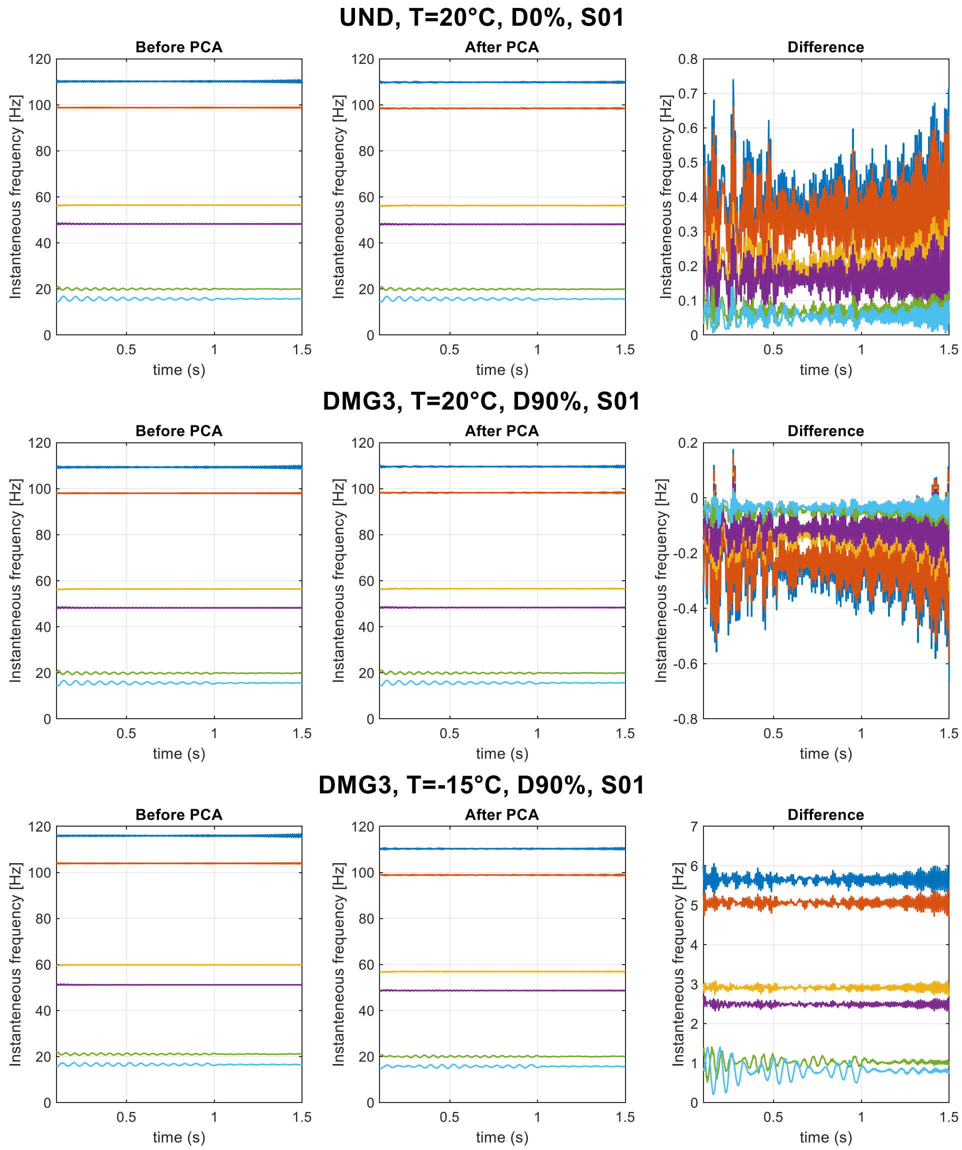

Figure 6.27 *Instantaneous Frequencies before and after the application of PCA dimensionality reduction (all scenarios, S01)*

All the other IF from other sensors are provided in the **Appendix D**

Figure shows the variation of the instanternous frequencies at each damage scenorio from S01. As it can be observed, although PCA dimensinality reduction was applied at high frequencies (~48 Hz, ~56.5 Hz, ~98.7Hz, ~110 Hz) the difference between damage and temprature scenarios in their value is visibly clear. And the application of the cluster analysis to such data will be not appropriate, as the goal of the methodoly is the distinguish betweem damaged and undamaged states. Moreover, signals from S02 and S05 were desregarded as well, as the mode mixing problem that was described earlier created data mixing after the PCA analysis, making instantenous frequencies unreliable.

In conclusion, only the first instanetous frequencies (~15.6 Hz) from S01, S03, S04 and S06 were considered for the clustering algorithm.

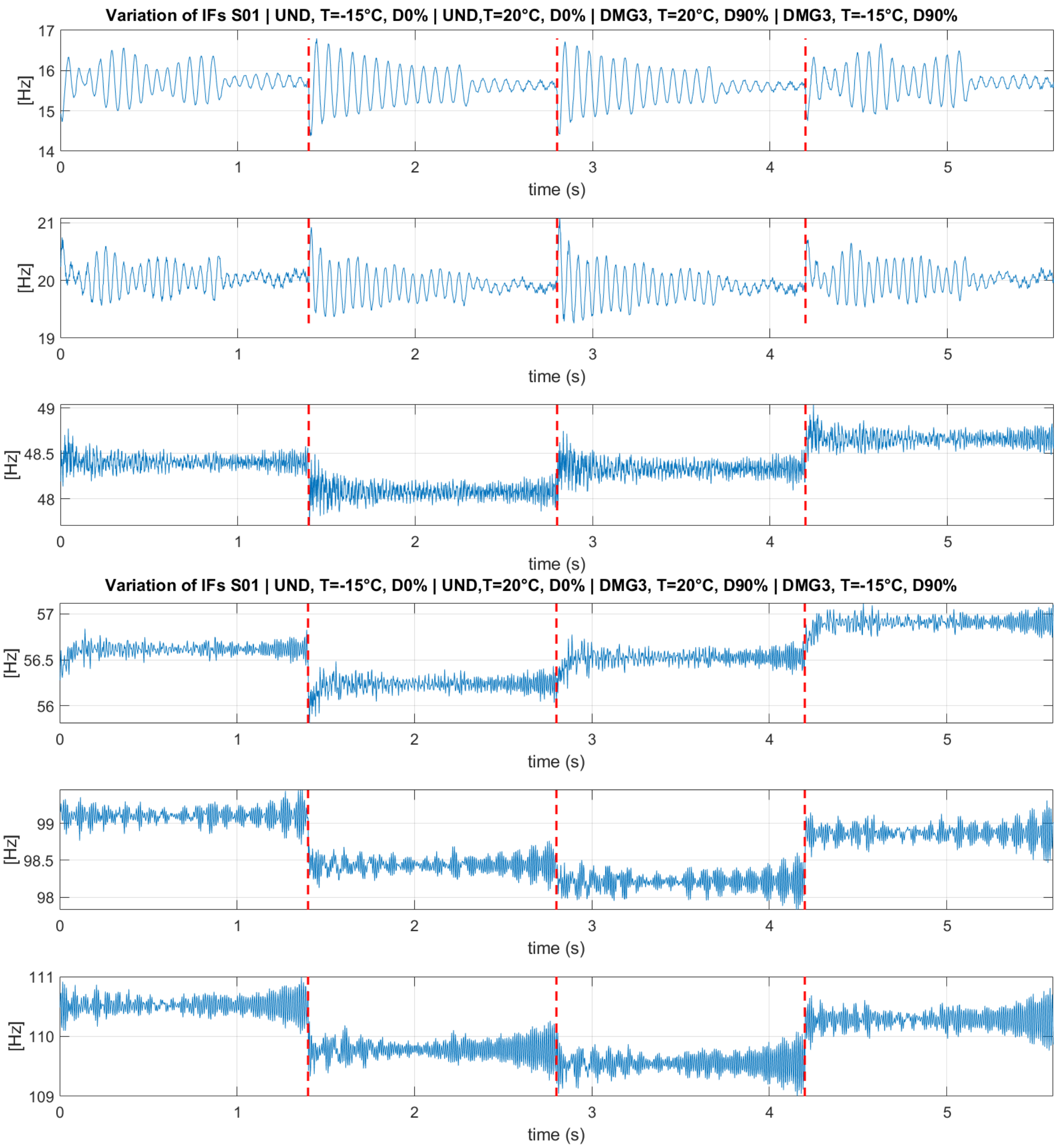

Figure 6.28 *Variation of the Instantaneous Frequencies of different scenarios related to S01*

Other IF from other variations from other sensors are provided in the **Appendix E**

6.6.5 K-means

Clustering methods, like K-means, are unsupervised machine learning algorithms. They do not require the definition of the reference or training data unlike supervised learning algorithms. Instead, they have capability to 'understand' a data set's structure by trying to find the most compact and separated set of clusters [7].

Before the application of the K-means algorithm, the data must be reduced in more generic types and less voluminous information in contrast with classical data used in SHM. The extracted damage sensitive features, in this case instantaneous frequency of the four scenarios with total time 5.6 seconds are converted into symbolic data (interquartile interval). The total number of points were 2240. A symbolic data length L=112 points was considered and respective boxplot for each sensor was constructed.

Figure 6.29 below illustrates 1st instantaneous frequency for all scenarios and corresponding boxplot which represents symbolic data.

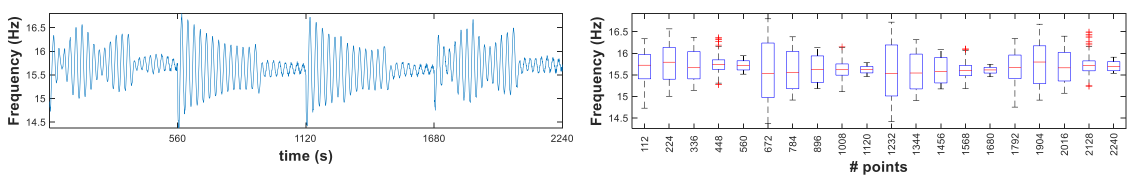

Figure 6.29 *1st instantaneous frequency of all scenarios for S01 and corresponding box plot*

It should be noted K-means algorithm has it is own advantages and disadvantages [40]

Table 6.8 *Advantages and disadvantages of K-means*

Advantages	Disadvantages
Relatively simple to implement	Choosing k-manually
Scales to large data sets	Being dependent on initial values
Guarantees convergence	Clustering data of varying sizes and density
Can warm-start the positions of centroids	Clusering outliers
Easily adapts to new examples	Scaling with number of dimensions
Genralizes to clusters of different shapes and sizes such as elliptical clusters	

The second step k-means algorithm is to determine the number of the K cluster which best describes the data. The silhouette index (SIL) was introduced earlier. Highest number of SIL corresponding to K clusters best describes the condition of the structure. It is performed for each moving window.

Moreover, in the implementation of the K-means algorithm in the MATLAB, the suitable method *'Start'* to determine the initial clusters centroid positions (or seeds) should be set among the options [41]:

'cluster'	Perform a preliminary clustering phase on a random 10% subsample of X when the number of observations in the subsample is greater than k. This preliminary phase is itself initialized using 'sample'. If the number of observations in the random 10% subsample is less than k, then the software selects k observations from X at random.
'plus' (default)	Select *k* seeds by implementing the *k*-means++ algorithm for cluster center initialization.
'sample'	Select k observations from X at random.
'uniform'	Select k points uniformly at random from the range of X. Not valid with the Hamming distance.
'numeric matrix'	k-by-*p* matrix of centroid starting locations. The rows of *Star*t correspond to seeds. The software infers k from the first dimension of *Start*, so you can pass in [] for *k*.
'numeric array'	*k*-by-*p*-by-*r* array of centroid starting locations. The rows of each page correspond to seeds. The third dimension invokes replication of the clustering routine. Page *j* contains the set of seeds for replicate *j*. The software infers the number of replicates (specified by the 'Replicates' name-value pair argument) from the size of the third dimension.

For this study case 'sample' was found as a consistent and appropriate method for the initial cluster centroid positions.

As explained methodology in Chapter 5.3 damage detection method is based on the value of the DC, which is difference between clusters. To calculate DC, the clusters of moving window must be defined. In this work the size of windows were selected as S=5 symbolic data, each comprising L=112 points of the damage sensitive feature. **Figure 30** shows a sequence of mobile windows.

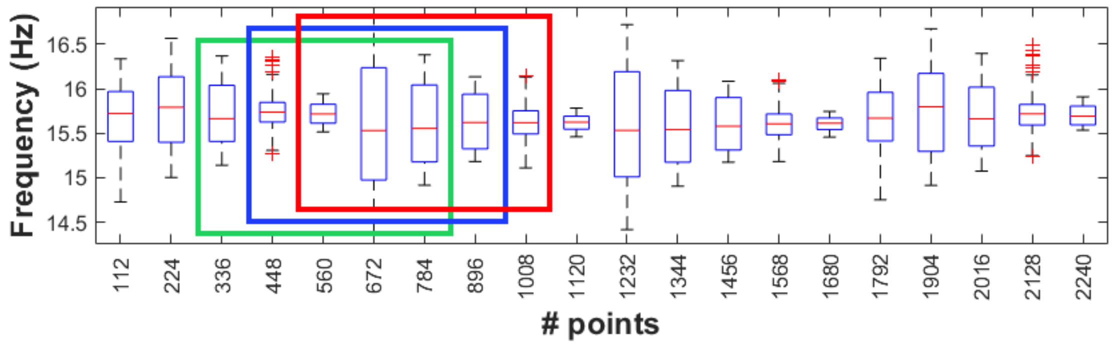

Figure 6.30 *A sequence of mobile windows*

The total number symbolic data equals 20 and the number of mobile windows as well DC are 16.

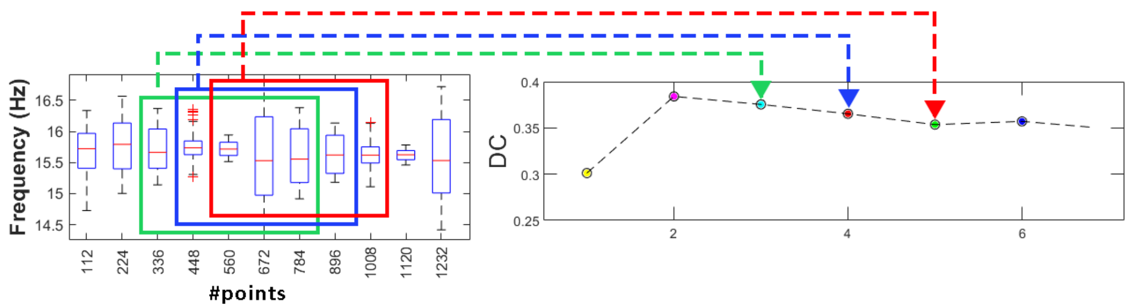

Figure 6.31 *DC values obtained for each time window*

It should be noted that if the time window increases, then we obtain higher sensitivity to damage detection, but higher probability of false detections. Moreover, If the samples within a time window decreases, it is possible to detect the damage earlier, but the probability of false detections increases (there is less sensitivity to damage detection). Therefore, it is necessary to find a balance among the 2 objectives: detect damage as soon as possible but get high confidence on the detection.

After the DC values are obtained, they must be statistically tested by the Confidence Boundary test. CB is defined for each time window containing 5 values of DC. The formula of CB is given at Chapter 5.3.

Finally, using DC and CB values the original detection index, DI is calculated. When DI value is negative or zero there is no damage in the structure, and while it is positive it indicates to the damage in the structure.

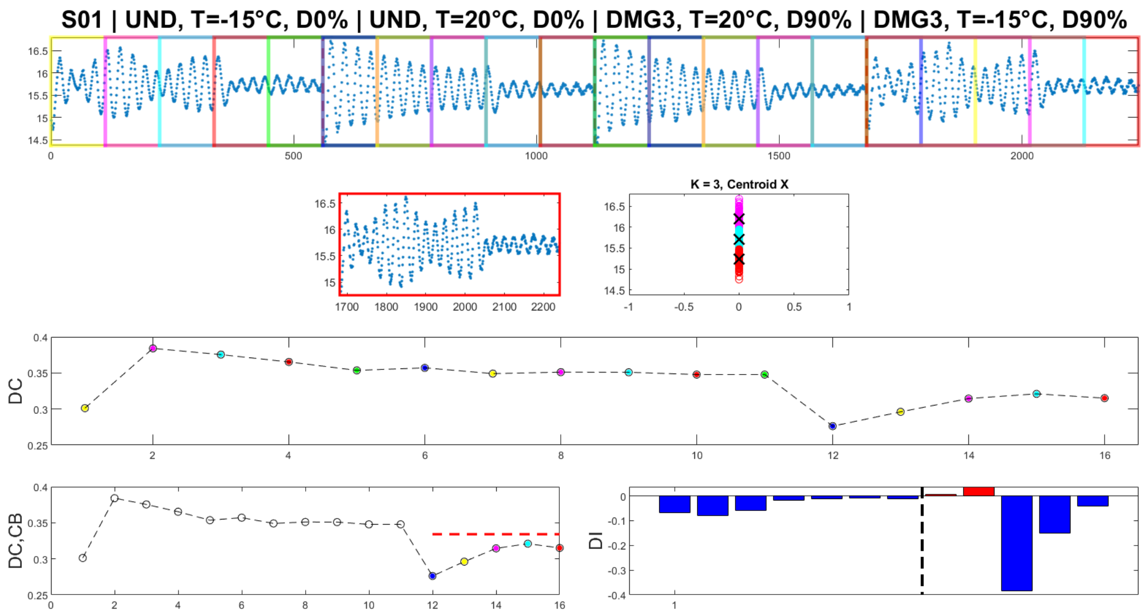

Figure 6.32 *K-means clustering on the S01 1st IF from different scenarios (Dashed line on the DI diagram – damage introduction).*

Figure 6.32 shows whole procedure for the IF (~15.6 Hz) from S01 for the damage scenarios. As it can be seen that the clustering algorithm exactly detects damage when it crosses the scenarios between UND T=20°C D0% and DMG3 T=20°C D90% while temperature change between scenarios does not create positive DI value.

One of the biggest distadcantages of the k-means algorithm is that is dependent on initial values. As the cluster centroids assigned randomly, it may create different output each time the algorithm runs. However, in this study case, this property of the algorithms has been founds useful to localize the damage. Specifically, k-means gives consistent output to the data closet thos the damage -S01, as it can be seen in the 4 tials (experiments) with DI index in **Figure 6.33** below.

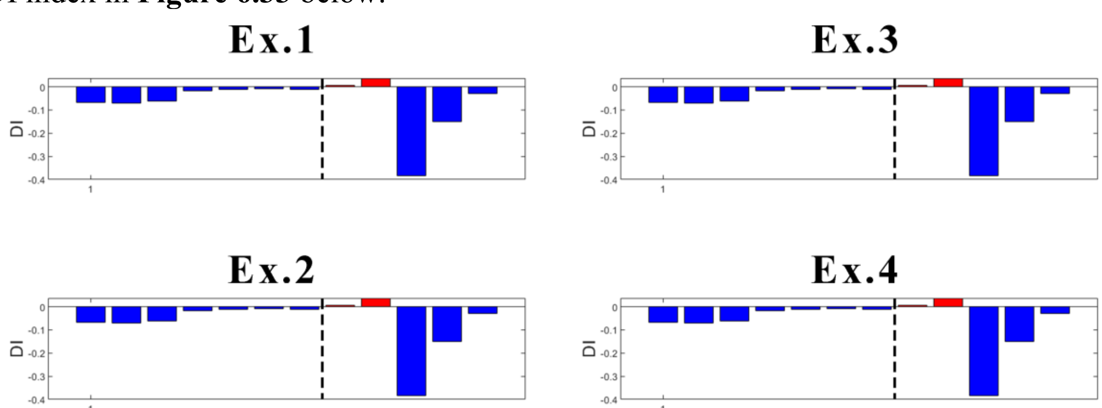

Figure 6.33 *4 Experiments with DI for S01 (dashed line- damage introduction)*

In the case S03, which is the second closest to the damage, K-means has early damage detection in all cases. However, the DI also shows the damage introduction at the correct place at DI diagram.

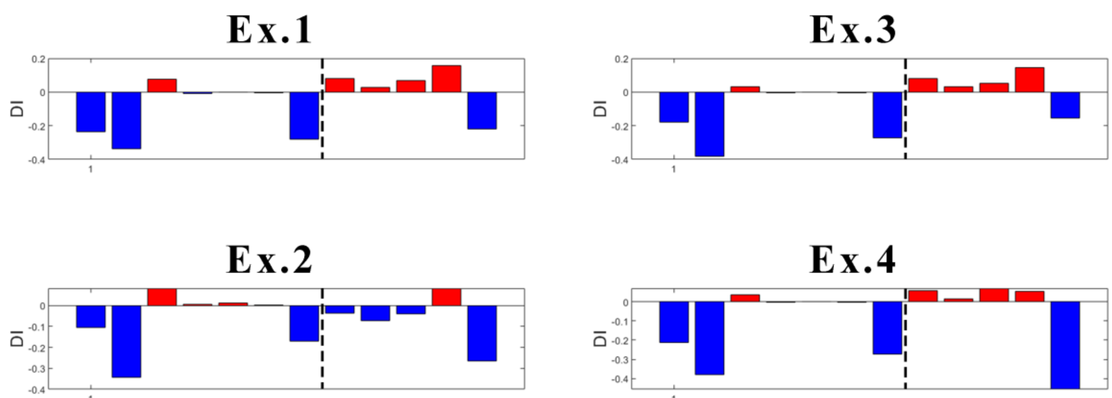

Figure 6.34 *Experiments with DI for S03 (dashed line- damage introduction)*

What concerns top DI for sensors S04 and S06, they both provided inconsistent results. With thigh randomness in their output. Early and false detection exist in their results.

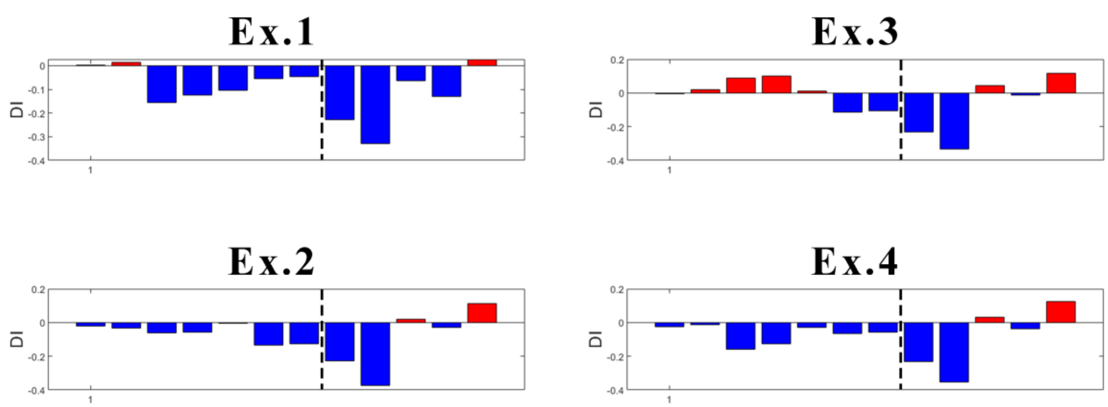

Figure 6.35 *Experiments with DI for S04 (dashed line- damage introduction)*

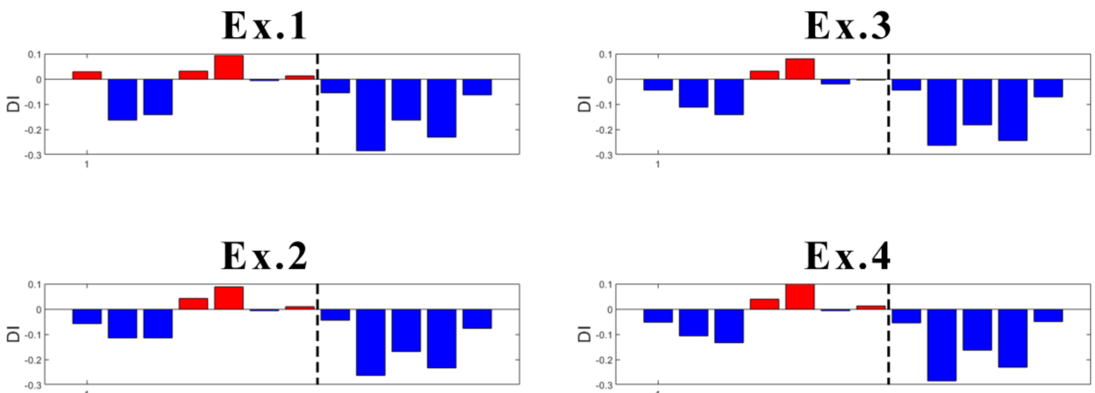

Figure 6.36 *4 Experiments with DI for S06 (dashed line- damage introduction)*

As a conclusion it can be said that the damage is located somewhere between the location of the S01 and S03, which is correct as the damage was introduced at the middle of the left span of the numerical bridge.

7 CONCLUSIONS

7.1 Summary

The research work presented in this thesis is dedicated to proposing testing the methodology for damage detection in bridges under traffic loading and environmental variability. Moreover, this study treats both operational and environmental effects comprehensively by modeling different damage and temperature scenarios.

Since the damage methodology presented in this thesis is based on time series data collected from a FE model, accurate information is required to build a robust model. The geometry and material properties of the bridge superstructure were modified from those established by Tatsis et al. [9], assuming a bridge height of 0.6m, a span length of 10m, and that it was made of reinforced concrete with E=35 MPa at T=20°C.

Very small damping (0.1% for the 1st bending frequency) is assumed since more realistic damping makes the bridge hardly vibrates and little information is extracted. The load speed-mesh size ratio is chosen to avoid as much as possible the appearance of forcing frequencies lower than the Nyquist frequency of 200Hz. Hence, a mesh size of 0.05m x 0.05m and a speed of 10m/s are considered.

To test the methodology for the numerical bridge 4 scenarios were assumed:

- 2 scenarios at the undamaged state of the bridge at T=-15°C and 20°C.
- 2 scenarios with damage (0.05m x 0.3 m) at the left mid-span with 90% stiffness reduction at T=-15°C and 20°C.

Due to the non-transient nature of recorded data, the Fast Fourier Transform (FFT) is not applicable. Instead, vertical acceleration measurements obtained from six sensors spaced along the bridge-like structure were analysed using the Hilbert–Huang transform (HHT).

The first step of the HHT-based method is the decomposition of the signal into Intrinsic Mode Functions (IMF) by applying of the Vibrational Mode Decomposition (VMD. The VMD method ensures no mixture of modes as well as the orthogonality of the transformation. Moreover, the signal decomposition is similar for every damage for all scenarios using always the same VMD: $\alpha = 1000$ $\varepsilon_a = 0.1$, $\varepsilon_r = 10^{-5}$, τ=0.1, $\varepsilon_r = 10^{-5}$ and O=100000, with exception of the number of modes K, taken as six for sensors S01, S03, S04, and S06; as five for sensors S02 and S05. This selection depends on the number of the predominant bending modes for a particular sensor location.

In the second step of the HHT-based method, the Hilbert Transform is then used to extract instantaneous frequencies, which are the damage-sensitive features.

To remove the temperature effects from the damage-sensitive features, PCA dimensionality reduction analysis was applied by the method proposed by Soo et al. [8] and Mujica, et al. [28]. The method consists of defining the baseline to the data matrix with the extreme temperature cases (30ºC and 70ºC) and adding a new observation for each scenario. It was observed that 1st Principal Component with the highest variance in the data matrix was responsible for the temperature-related effects. As a result, the damage-sensitive features were reconstructed by removing 1st PC.

Finally, to detect and localize the damage, a machine learning algorithm (K-means) is applied. Using the symbolic data to reduce the amount of data, a technique of moving the time window is applied to damage-sensitive features. A confidence boundary (CB) was deployed to test DC values for each window and detection index (DI) is defined to give a result with high confidence.

Results have shown that K-means in combination with PCA dimensionality reduction can identify and localizing damages. The methodology is very effective and reliable in the field of bridge structural health monitoring under both traffic-induced loads and temperature changes.

7.2 Proposals for future research

Further investigation of damage detection systems under operational and environmental variability is one of this thesis's potential study areas. The proposed methodology can be validated on the real structure, given the fact that both damaged and undamaged data is available.

In this work, the environmental effects were eliminated from the structure’s response by PCA dimensionality reduction, specifically creating a baseline data with extreme temperature cases. Although it was proven to effective at the low instantaneous frequencies, in the future it can be improved for high instantaneous frequencies as well. Moreover, it is worth considering developing a completely new methodology without the baseline data, as it computationally expensive.

Finally, the higher levels of the damage assessment can be reached. In this study, the capability of the K-means algorithms to detect and localize the damage was shown. The damage type, extent and prediction could be achieved by examining machine learning algorithms like Neural network (NN) and Support-Vector Machine (SVM).

REFERENCES

[1] M. Morgese, F. Ansari, M. Domaneschi and G. P. Cimellaro, "Post-collapse analysis of Morandi's Polcevera viaduct in Genoa Italy," *Journal of Civil Structural Health Monitoring,* no. ISSN 2190-5452, 2019.

[2] G. J. Puskar, Associated Press, [Online]. Available: https://www.nytimes.com/2022/01/28/us/pittsburgh-bridge-collapse-biden.html.

[3] Taiwan News, [Online]. Available: https://www.engineering.com/story/what-caused-taiwans-nanfangao-bridge-to-collapse.

[4] "Pittsburgh Post-Gazette," [Online]. Available: https://www.post-gazette.com/local/city/2022/01/28/pittsburgh-bridge-collapse-forbes-braddock-avenue-point-breeze-squirrel-hill/stories/202201280075.

[5] R. Horgan, "Fatal Taiwan bridge collapse is latest example of maintenance failings," New Civil Engineer, [Online]. Available: https://www.newcivilengineer.com/latest/fatal-taiwan-bridge-collapse-is-latest-example-of-maintenance-failings-07-10-2019/.

[6] N. Rania, I. Coppola, F. Martorana and L. Migliorini, "The collapse of the Morandi Bridge in Genoa on 14 August 2018: A collective traumatic event and its emotional impact linked to the place and loss of a symbol," *Sustainability,* vol. 11, no. 23, 2019.

[7] J. P. Santos, C. Crémona, L. Calado, P. Silveira and A. D. Orcesi, "On-line unsupervised detection of early damage," *STRUCTURAL CONTROL AND HEALTH MONITORING,* vol. 23, pp. 1047-1069, 2016.

[8] W. Soo Lon Wah, Y.-T. Chen, A. Elamin and G. W. Roberts, "Damage detection under temperature conditions using PCA - an application to the Z24 Bridge".

[9] K. Tatsis and E. Chatzi, "A NUMERICAL BENCHMARK FOR SYSTEM IDENTIFICATION UNDER OPERATIONAL AND ENVIRONMENTAL VARIABILITY," in *IOMAC*, Copenhagen, 2019.

[10] K. Gkoumas, F. L. Marques Dos Santos, M. van Balen , A. Tsakalidis, A. Ortega Hortelano, M. Grosso, G. Haq and F. Pekár, "Research and innovation in bridge maintenance, inspection and monitroing - A European perspective based on the Transport Research and Innovation Monitoring Information System (TRIMIS)," Publications Office of the European Union, Luxembourg, 2019.

[11] N. Rania, I. Coppola, F. Martorana and L. Migliorini, "The collapse of the Morandi Bridge in Genoa on 14 August 2018: A collective traumatic event and its emotional impact linked to the place and loss of a symbol," *Sustainability,* 2019.

[12] A. Malekloo, E. Ozer, M. AlHamaydeh and M. Girolami, "Machine learning and structural health monitoring overview with emerging technology and high-dimensional data source highlights," *Structural Health Monitoring,* vol. 0(0) 1–50, 2021.

[13] A. Rytter, "Vibrational based inspection of civil engineering structures," Dept. of Building Technology and Structural Engineering, Aalborg University, 1993.

[14] P. A. Gardner, "On Novel Approaches to Model-Based Structural Health Monitoring," 2018.

[15] P. Cao, S. Qi and J. Tang, "Structural damage identification using piezoelectric impedance measurement with sparse inverse analysis," *Smart Mater Struct,* vol. 27, 2018.

[16] E. Z. Moore, J. M. Nichols and K. D. Murphy, "Model-based SHM: Demonstration of identification of a crack in a thin plate using free vibration data.," *Mech Syst Signal Process,* pp. 284-295, 2012.

[17] F. J. Tenelema, R. M. Delgadillo and J. R. Casas, "Bridge damage detection and quantification under environmental effects by Principal Component Analysis," 2020.

[18] R. M. Delgadillo and J. R. Casas, "Bridge damage detection via Improved Completed Ensemble EMD with Adaptive Noise and machine learning algorithms".

[19] K. Dragomiretskiy and D. Zosso, "Variational Mode Decomposition," *IEEE TRANSACTIONS ON SIGNAL PROCESSING,* vol. 62, no. 3, pp. 531-544, FEBRUARY 1, 2014.

[20] A. Bagheri, E. O. Ozbulut and K. D. Harris, "Structural system identification based on variational mode," *Journal of Sound and Vibration,* no. 417, pp. 182-197, 2018.

[21] F. J. Tenelema Muñoz, "Bridge Damage Identification under operational and environmental variability," Department of Civil and Environmental Engineering, UPC, Barcelona, 2020.

[22] M. Zhang, Z. Jiang and K. Feng, "Research on variational mode decomposition in rolling bearings fault diagnosis of the multistage centrifugal pump," *Mechanical Systems and Signal Processing,* vol. 93, pp. 460-493, 2017.

[23] S. Liu, G. Tang and X. Wang, "Time frequency analysis method for rotary mechanical fault based on improved variational mode decomposition," *Journal of Vibration Engineering,* vol. 29, pp. 1119-1126, 2016.

[24] S. Wu, F. Feng, J. Zhu, C. Wu and G. Zhang, "A Method for Determining Intrinsic Mode Function Number in Variational Mode Decomposition and Its Application to Bearing Vibration Signal Processing," *Research Article,* vol. 2020.

[25] D. Pines and L. Salvino, "Health Monitoring of One Dimensional Structures Using Empirical Mode Decomposition and the Hilbert-Huang Transform".

[26] D. Zappalà, "HILBERT ANALYSIS OF AIR TEMPERATURE DYNAMICS," Universitat Politècnica de Catalunya, Terrassa (Spain), 2019.

[27] W. Soo Lon Wah, Y.-T. Chen, G. W. Roberts and A. Elamin, "Separating damage from environmental effects affecting civil structures for near real-time damage detection," *Structural Health Monitoring,* pp. 1-19, 2017.

[28] L. E. Mujica, J. Rodellar, A. Fernandez and A. Guemes, "Q-statistic and T2-statistic PCA-based measures for damage assessment in structures," *Structural Health Monitoring,* pp. 1-15, 2010.

[29] D. Xu and Y. TIan, "A Comprehensive Survey of Clustering Algorithms," 2015.

[30] J. Santos, C. Crémona, A. D. Orcesi and P. Silveira, "Multivariate statistical analysis for early damage detection," *Engineering Structures,* vol. 56, pp. 273-285, 2013.

[31] J. P. Santos, "Smart structural health monitoring techniques for novelty identification in civil engineering structures," Lisbon, 2014.

[32] E. Oñate, Structural analysis with the finite element method. Linear statics: volume 2: beams, plates and shells, Springer Science & Business Media,, 2013.

[33] M. A. Neto, A. Amaro, L. Roseiro, J. Cirne and R. Leal, Engineering computation of structures: the finite element method, Springer, 2015.

[34] G. Noh and K. J. Bathe, "For direct time integrations: A comparison of the Newmark and q∞-Bathe schemes," 2019.

[35] P. Paultre, Dynamics of structures, John Wiley & Sons, 2013.

[36] M. N. Priestley, F. Seible and G. M. Calvi, Seismic design and retrofit of bridges, John Wiley & Sons, 1996.

[37] P. A. Millette, "The heisenberg uncertainty principle and the nyquist-shannon sampling theorem," *Progress in Physics,* vol. 9, no. 3, pp. 9-14, 2013.

[38] Y. Jiao, H. Liu, X. Wang, Y. Zhang, G. Luo and Y. Gong, "Temperature Effect on Mechanical Properties and Damage Identification of Concrete Structure," *Advances in Materials Science and Engineering,* p. 10, 2014.

[39] S. Wu, F. Feng, J. Zhu, C. Wu and G. Zhang, "A Method for Determining Intrinsic Mode Function Number in Variational Mode Decomposition and Its Application to Bearing Vibration Signal Processing," *Hindawi Shock and Vibration,* vol. 2020, no. 8304903, p. 16, 2020.

[40] Google, "Clustering in Machine Learning," 11 February 2020. [Online]. Available: https://developers.google.com/machine-learning/clustering/algorithm/advantages-disadvantages.

[41] MATLAB, "k-means clustering," [Online]. Available: https://it.mathworks.com/help/stats/kmeans.html#d123e555240.

APPENDIX

Appendix A

The appendix contains Y-accelerations from all six sensors of four case scenarios.

Appendix B

The appendix contains Vibrational Mode Decomposition (VMD) of the recorded signals from all 6 sensor of four case scenarios.

Appendix C

The appendix contains Principal Component Analysis of each case scenario.
Red dots represent extreme positive temperatures (67°C, 68°C, 69°C, 70°C)
Blue dots represent extreme negative temperatures (-30°C, -29°C, -28°C -27°C)
Black dots represent the case study under the observation.

Appendix D

The appendix contains Instantaneous Frequencies (IF) before and after the application of PCA dimensionality reduction. Moreover, their difference is presented as well.

Appendix E

The appendix contains the variation of the Instantaneous Frequencies (IF) along the case scenarios.

Appendix A

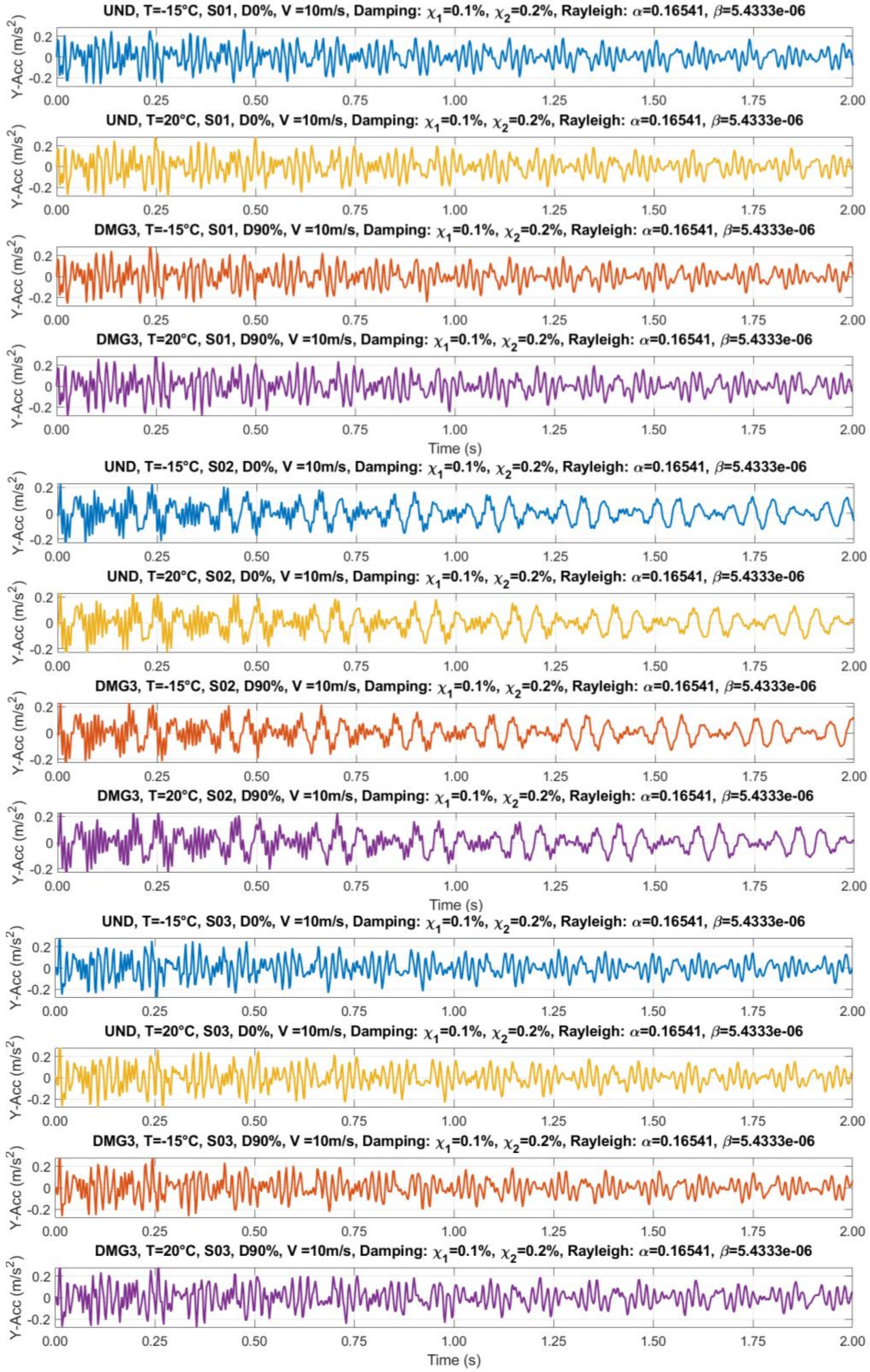

UND, T=-15°C, S01, D0%, V =10m/s, Damping: χ_1=0.1%, χ_2=0.2%, Rayleigh: α=0.16541, β=5.4333e-06
UND, T=20°C, S01, D0%, V =10m/s, Damping: χ_1=0.1%, χ_2=0.2%, Rayleigh: α=0.16541, β=5.4333e-06
DMG3, T=-15°C, S01, D90%, V =10m/s, Damping: χ_1=0.1%, χ_2=0.2%, Rayleigh: α=0.16541, β=5.4333e-06
DMG3, T=20°C, S01, D90%, V =10m/s, Damping: χ_1=0.1%, χ_2=0.2%, Rayleigh: α=0.16541, β=5.4333e-06
UND, T=-15°C, S02, D0%, V =10m/s, Damping: χ_1=0.1%, χ_2=0.2%, Rayleigh: α=0.16541, β=5.4333e-06
UND, T=20°C, S02, D0%, V =10m/s, Damping: χ_1=0.1%, χ_2=0.2%, Rayleigh: α=0.16541, β=5.4333e-06
DMG3, T=-15°C, S02, D90%, V =10m/s, Damping: χ_1=0.1%, χ_2=0.2%, Rayleigh: α=0.16541, β=5.4333e-06
DMG3, T=20°C, S02, D90%, V =10m/s, Damping: χ_1=0.1%, χ_2=0.2%, Rayleigh: α=0.16541, β=5.4333e-06
UND, T=-15°C, S03, D0%, V =10m/s, Damping: χ_1=0.1%, χ_2=0.2%, Rayleigh: α=0.16541, β=5.4333e-06
UND, T=20°C, S03, D0%, V =10m/s, Damping: χ_1=0.1%, χ_2=0.2%, Rayleigh: α=0.16541, β=5.4333e-06
DMG3, T=-15°C, S03, D90%, V =10m/s, Damping: χ_1=0.1%, χ_2=0.2%, Rayleigh: α=0.16541, β=5.4333e-06
DMG3, T=20°C, S03, D90%, V =10m/s, Damping: χ_1=0.1%, χ_2=0.2%, Rayleigh: α=0.16541, β=5.4333e-06
Y-Acc (m/s^2)
0.2
0
-0.2
0.00
0.25
0.50
0.75
1.00
1.25
1.50
1.75
2.00
Time (s)

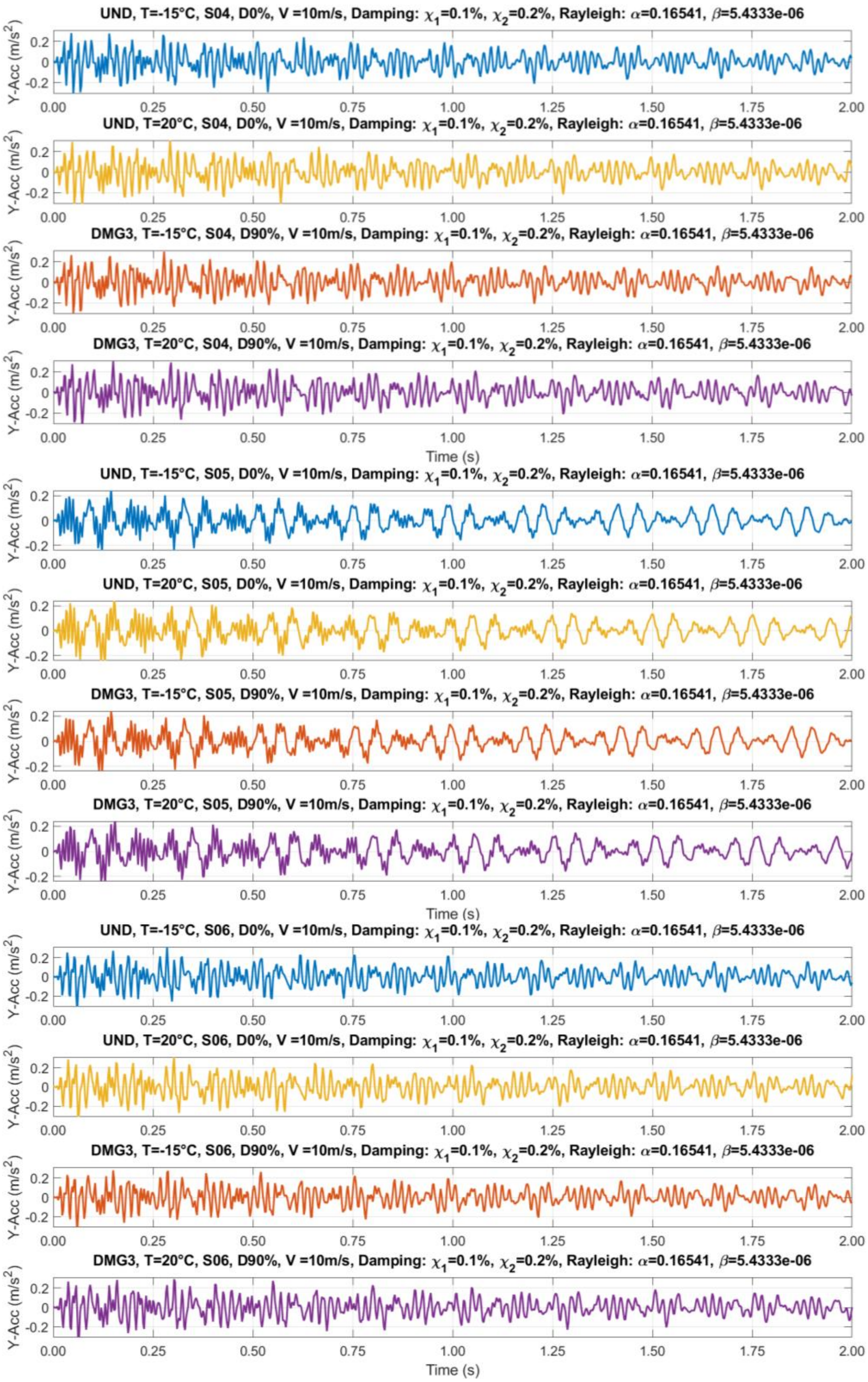
UND, T=-15°C, S04, D0%, V =10m/s, Damping: χ_1=0.1%, χ_2=0.2%, Rayleigh: α=0.16541, β=5.4333e-06
UND, T=20°C, S04, D0%, V =10m/s, Damping: χ_1=0.1%, χ_2=0.2%, Rayleigh: α=0.16541, β=5.4333e-06
DMG3, T=-15°C, S04, D90%, V =10m/s, Damping: χ_1=0.1%, χ_2=0.2%, Rayleigh: α=0.16541, β=5.4333e-06
DMG3, T=20°C, S04, D90%, V =10m/s, Damping: χ_1=0.1%, χ_2=0.2%, Rayleigh: α=0.16541, β=5.4333e-06
UND, T=-15°C, S05, D0%, V =10m/s, Damping: χ_1=0.1%, χ_2=0.2%, Rayleigh: α=0.16541, β=5.4333e-06
UND, T=20°C, S05, D0%, V =10m/s, Damping: χ_1=0.1%, χ_2=0.2%, Rayleigh: α=0.16541, β=5.4333e-06
DMG3, T=-15°C, S05, D90%, V =10m/s, Damping: χ_1=0.1%, χ_2=0.2%, Rayleigh: α=0.16541, β=5.4333e-06
DMG3, T=20°C, S05, D90%, V =10m/s, Damping: χ_1=0.1%, χ_2=0.2%, Rayleigh: α=0.16541, β=5.4333e-06
UND, T=-15°C, S06, D0%, V =10m/s, Damping: χ_1=0.1%, χ_2=0.2%, Rayleigh: α=0.16541, β=5.4333e-06
UND, T=20°C, S06, D0%, V =10m/s, Damping: χ_1=0.1%, χ_2=0.2%, Rayleigh: α=0.16541, β=5.4333e-06
DMG3, T=-15°C, S06, D90%, V =10m/s, Damping: χ_1=0.1%, χ_2=0.2%, Rayleigh: α=0.16541, β=5.4333e-06
DMG3, T=20°C, S06, D90%, V =10m/s, Damping: χ_1=0.1%, χ_2=0.2%, Rayleigh: α=0.16541, β=5.4333e-06
Y-Acc (m/s^2)
Time (s)
0.00 0.25 0.50 0.75 1.00 1.25 1.50 1.75 2.00
-0.2 0 0.2

Appendix B

UND, T = -15°C, D0%
S01

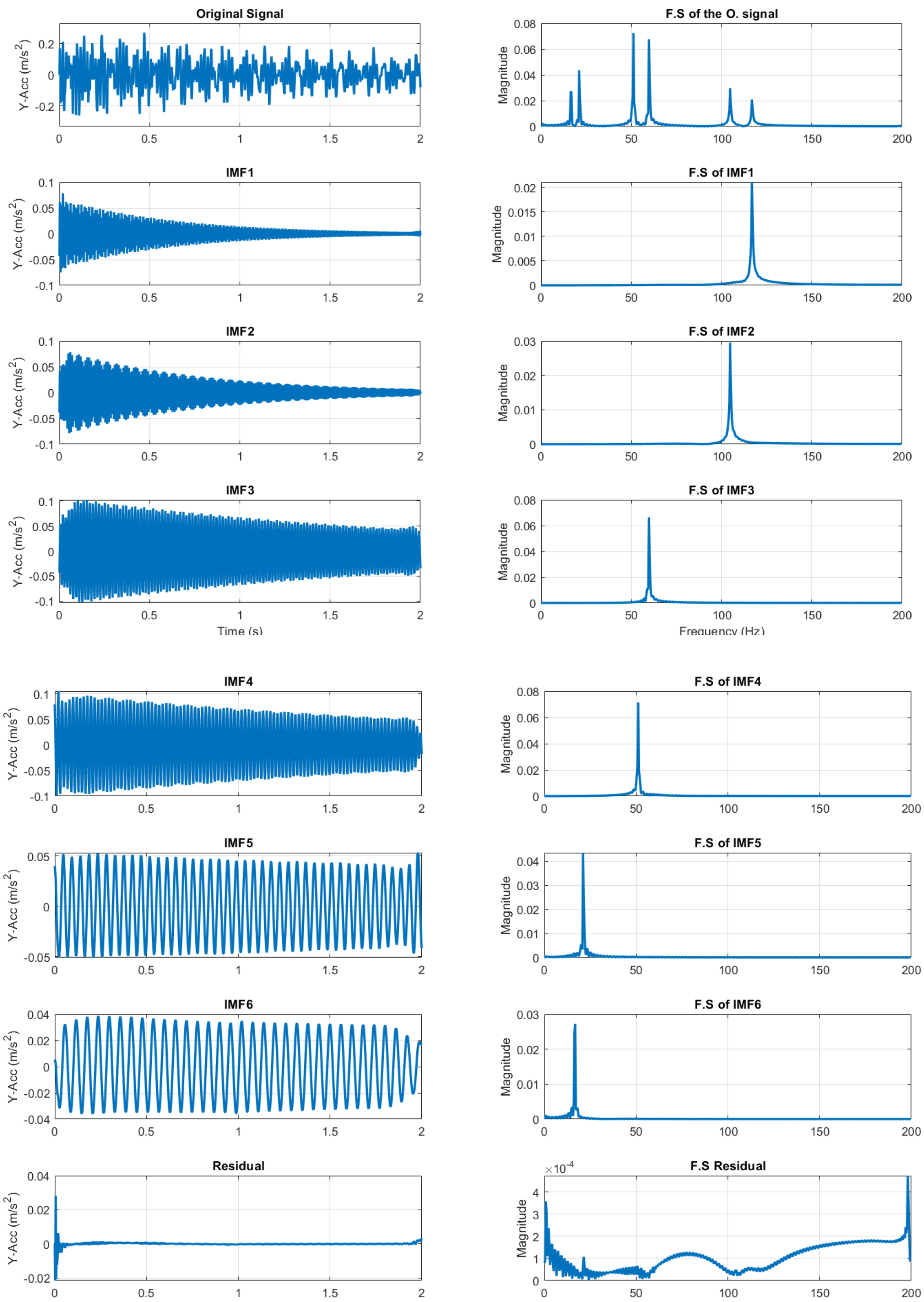

S02

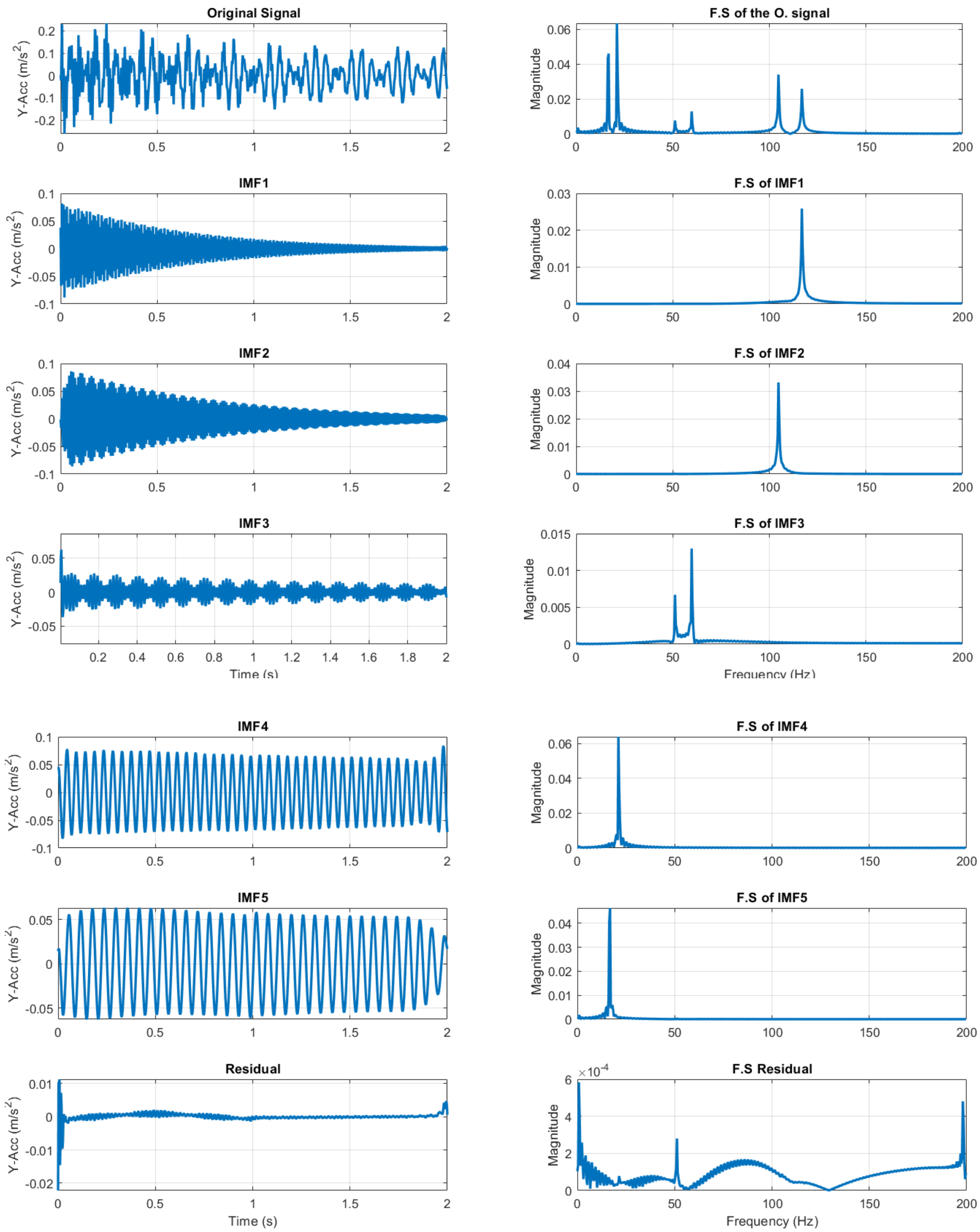
Original Signal
F.S of the O. signal
IMF1
F.S of IMF1
IMF2
F.S of IMF2
IMF3
F.S of IMF3
IMF4
F.S of IMF4
IMF5
F.S of IMF5
Residual
F.S Residual
Y-Acc (m/s²)
Magnitude
Time (s)
Frequency (Hz)

S03

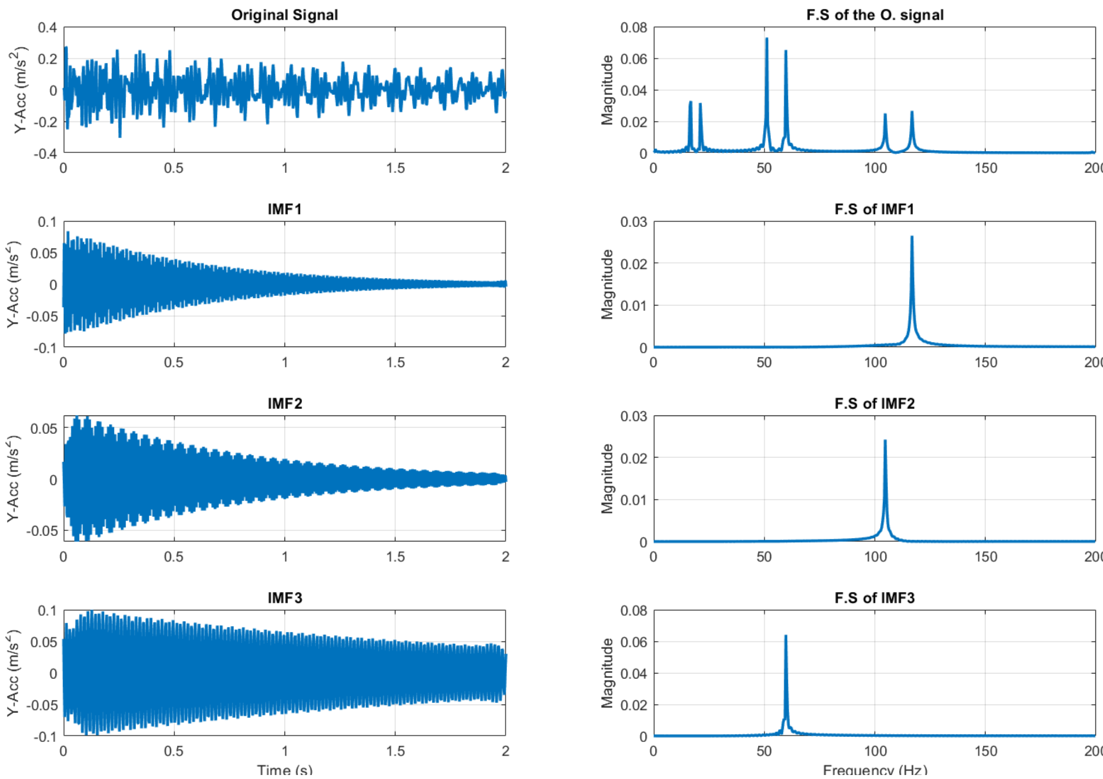

Original Signal
F.S of the O. signal
IMF1
F.S of IMF1
IMF2
F.S of IMF2
IMF3
F.S of IMF3
Y-Acc (m/s^2)
Magnitude
Time (s)
Frequency (Hz)

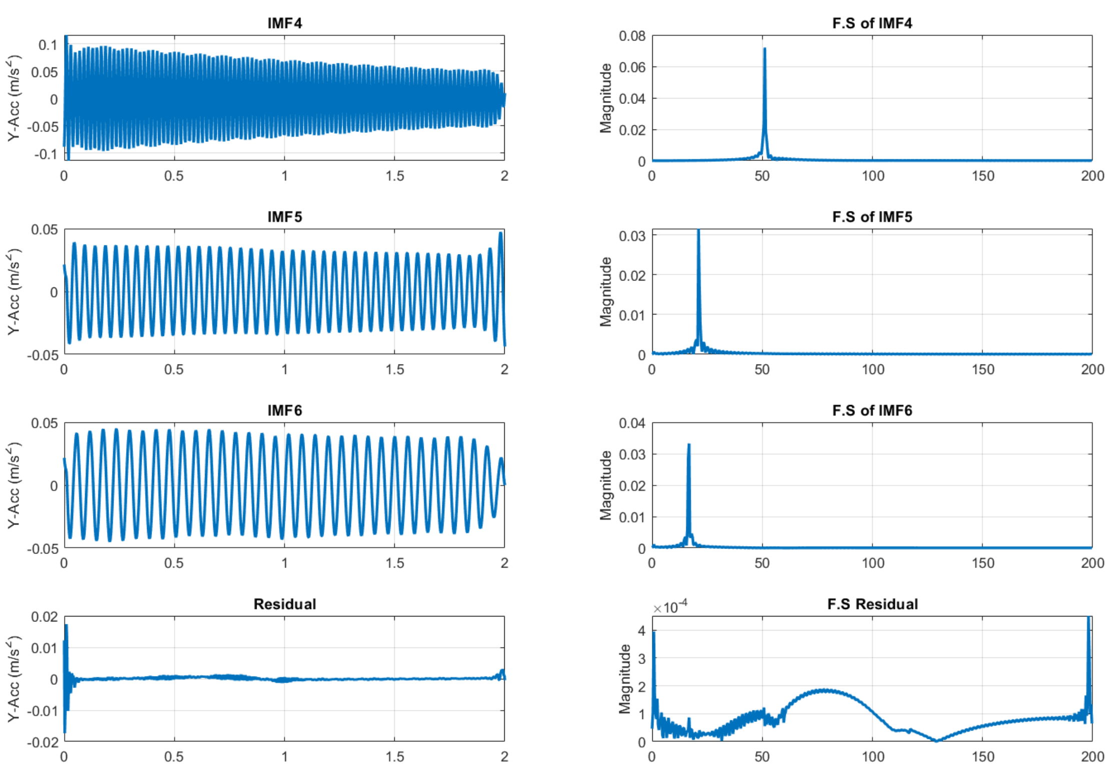

IMF4
F.S of IMF4
IMF5
F.S of IMF5
IMF6
F.S of IMF6
Residual
F.S Residual
Y-Acc (m/s^2)
Magnitude
$\times 10^{-4}$
Time (s)
Frequency (Hz)

S04

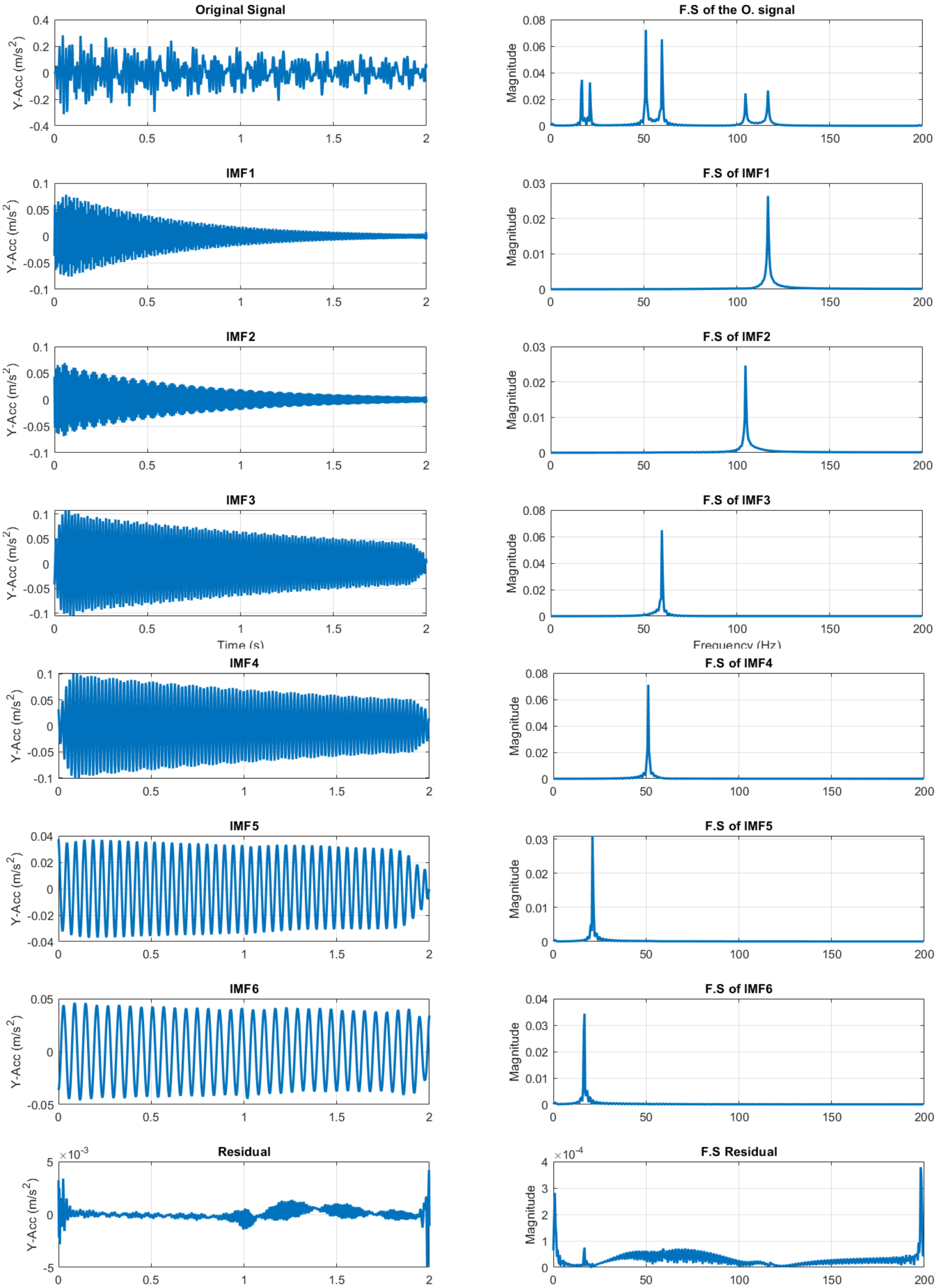

Original Signal
Y-Acc (m/s^2)
F.S of the O. signal
Magnitude
IMF1
F.S of IMF1
IMF2
F.S of IMF2
IMF3
F.S of IMF3
Time (s)
Frequency (Hz)
IMF4
F.S of IMF4
IMF5
F.S of IMF5
IMF6
F.S of IMF6
Residual
F.S Residual
×10^-3
×10^-4
Time (s)
Frequency (Hz)

S05

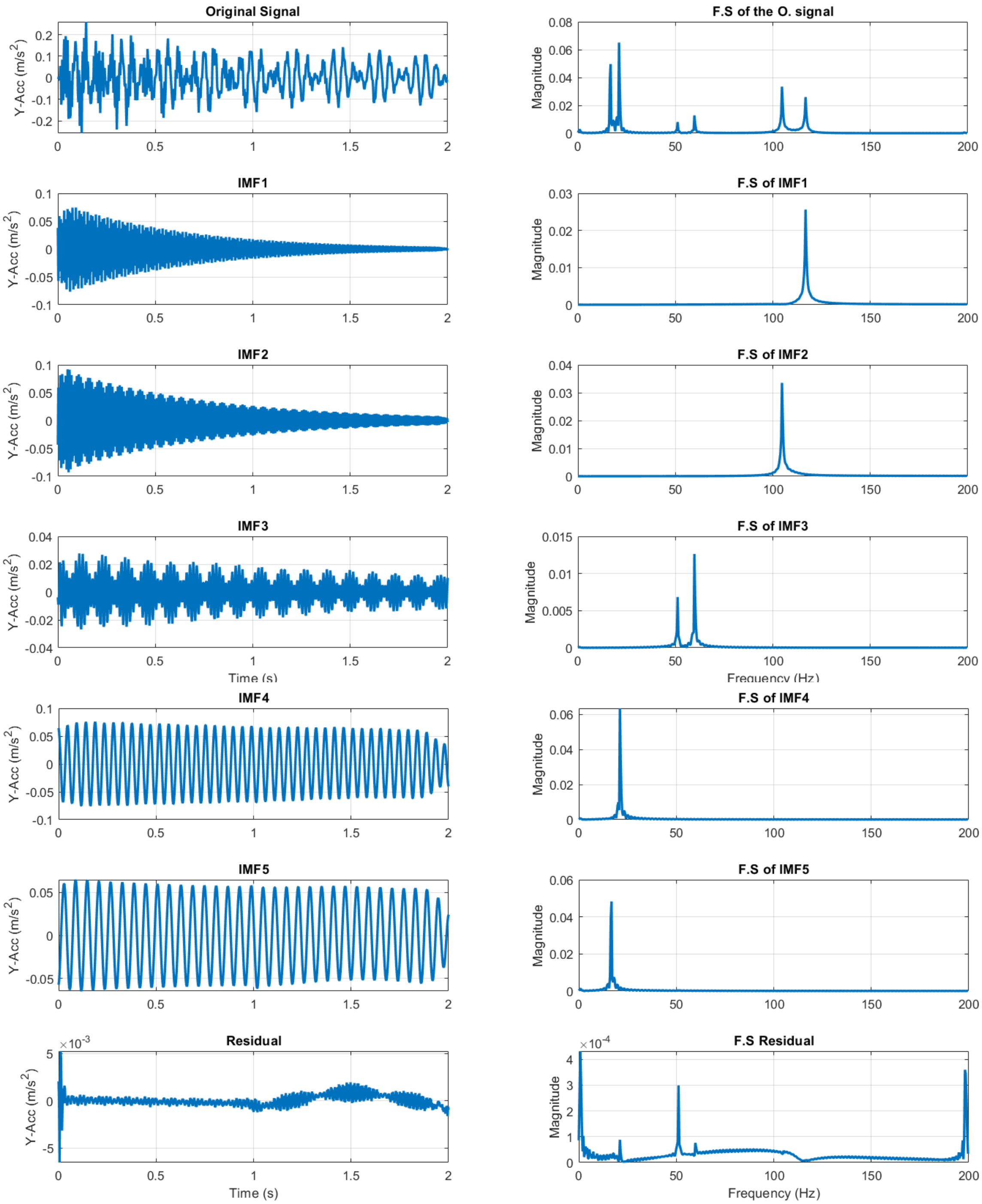
Original Signal
F.S of the O. signal
IMF1
F.S of IMF1
IMF2
F.S of IMF2
IMF3
F.S of IMF3
IMF4
F.S of IMF4
IMF5
F.S of IMF5
Residual
F.S Residual
Y-Acc (m/s^2)
Magnitude
Time (s)
Frequency (Hz)
×10^-3
×10^-4

S06

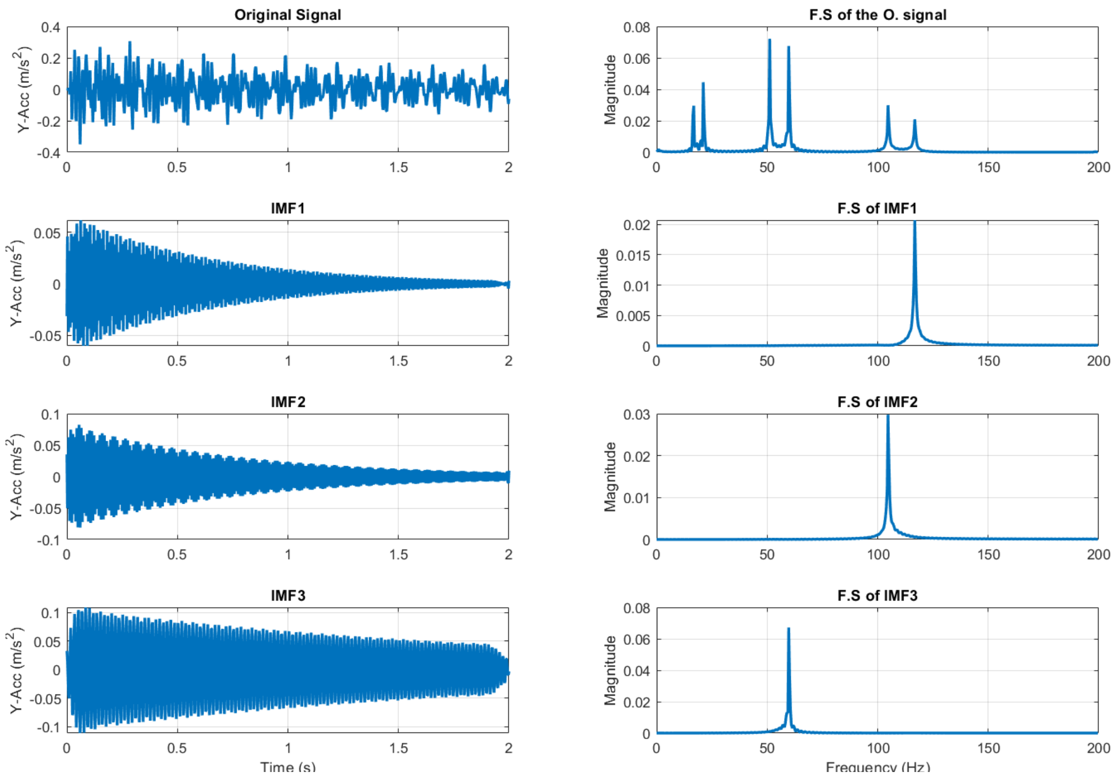
Original Signal
F.S of the O. signal
IMF1
F.S of IMF1
IMF2
F.S of IMF2
IMF3
F.S of IMF3
Y-Acc (m/s^2)
Magnitude
Time (s)
Frequency (Hz)

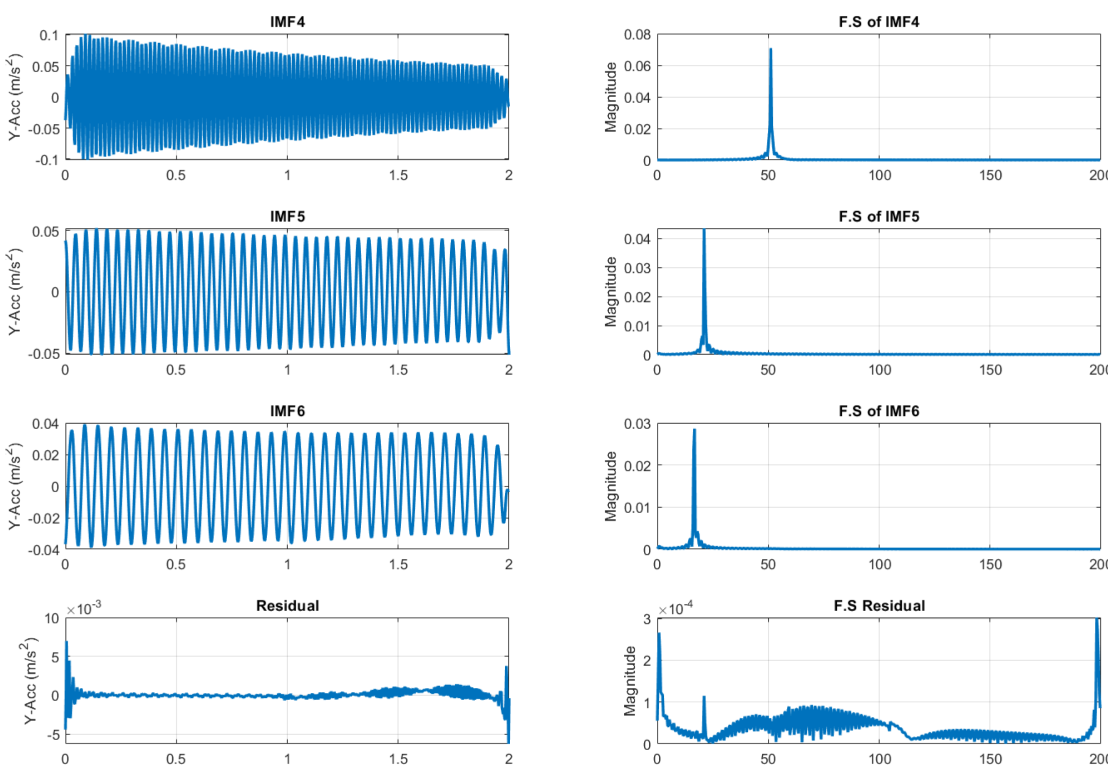
IMF4
F.S of IMF4
IMF5
F.S of IMF5
IMF6
F.S of IMF6
Residual
F.S Residual
Y-Acc (m/s^2)
Magnitude
Time (s)
Frequency (Hz)

UND, T= 20°C, D0%
S01

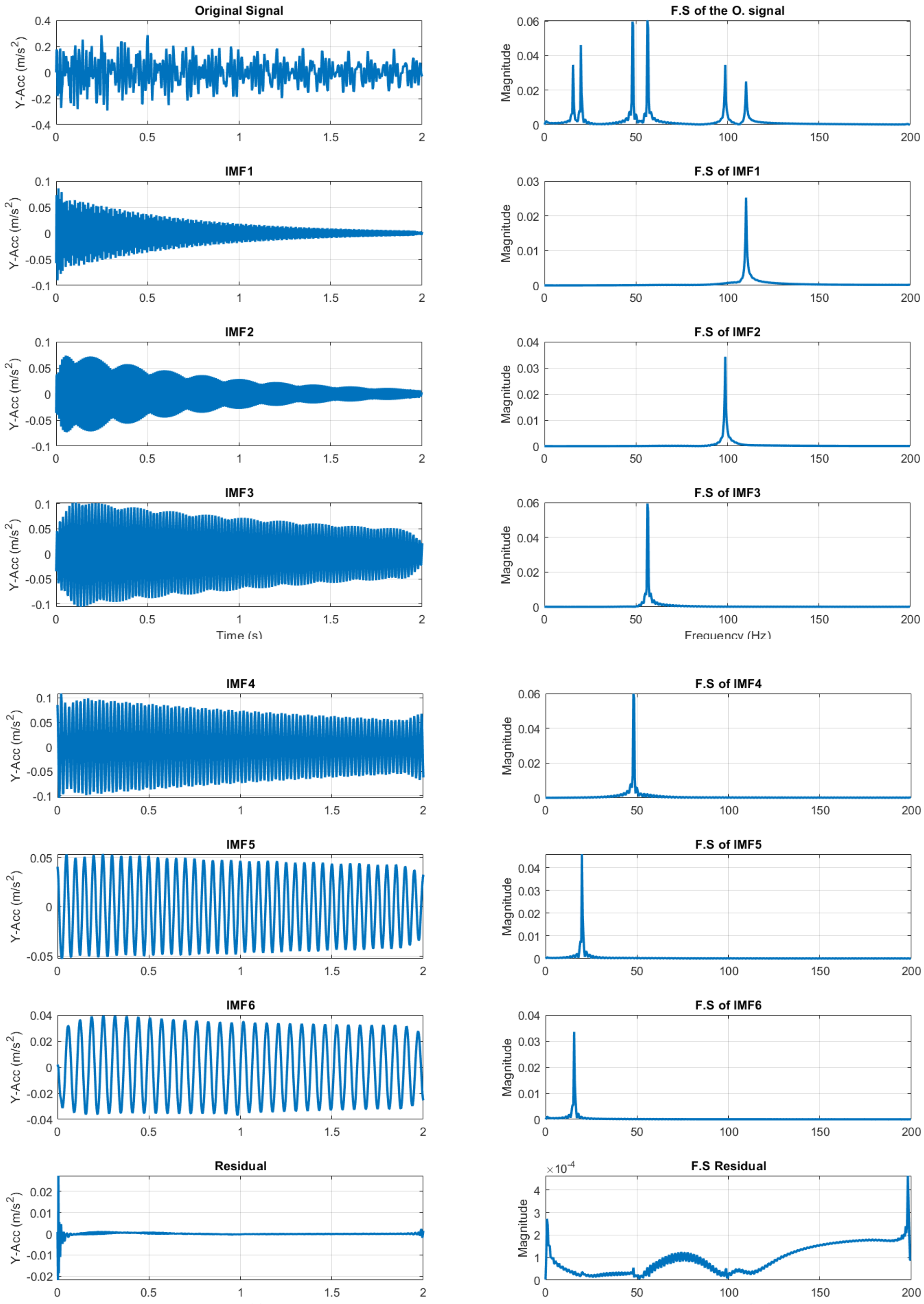

S02

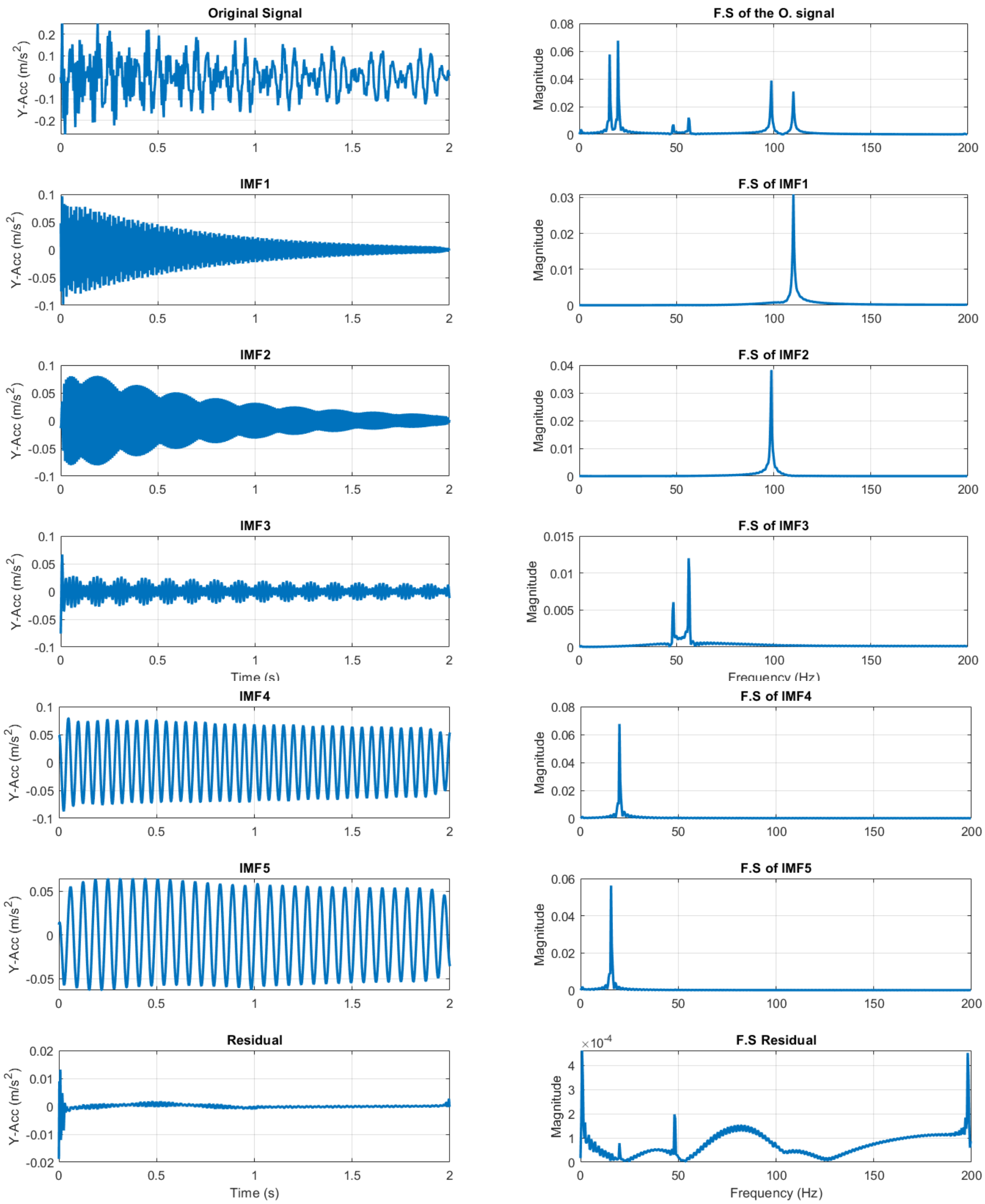
Original Signal
F.S of the O. signal
IMF1
F.S of IMF1
IMF2
F.S of IMF2
IMF3
F.S of IMF3
IMF4
F.S of IMF4
IMF5
F.S of IMF5
Residual
F.S Residual
Y-Acc (m/s^2)
Magnitude
Time (s)
Frequency (Hz)

S03

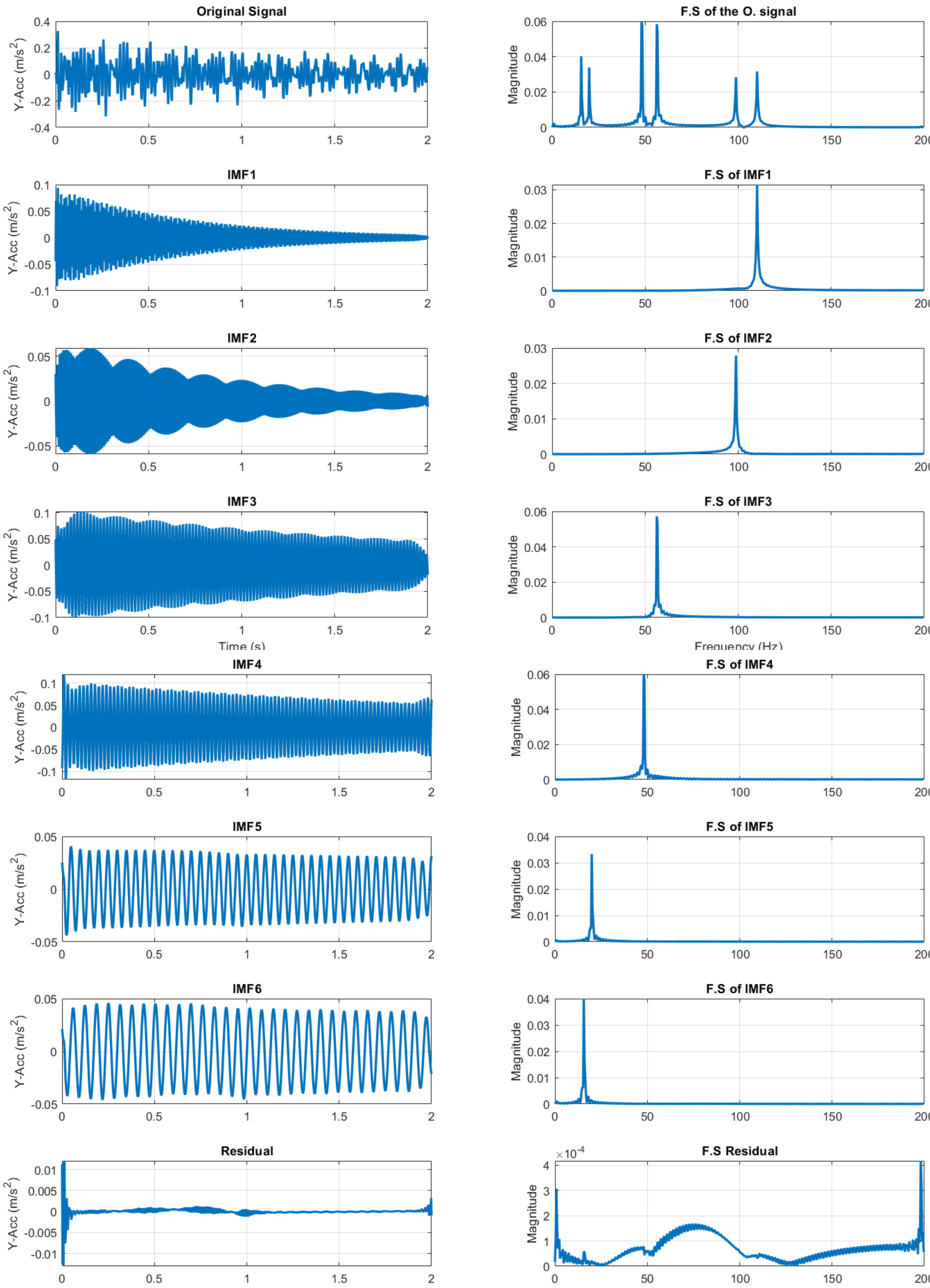
Original Signal
F.S of the O. signal
IMF1
F.S of IMF1
IMF2
F.S of IMF2
IMF3
F.S of IMF3
IMF4
F.S of IMF4
IMF5
F.S of IMF5
IMF6
F.S of IMF6
Residual
F.S Residual
Y-Acc (m/s^2)
Magnitude
Time (s)
Frequency (Hz)
$\times 10^{-4}$

S04

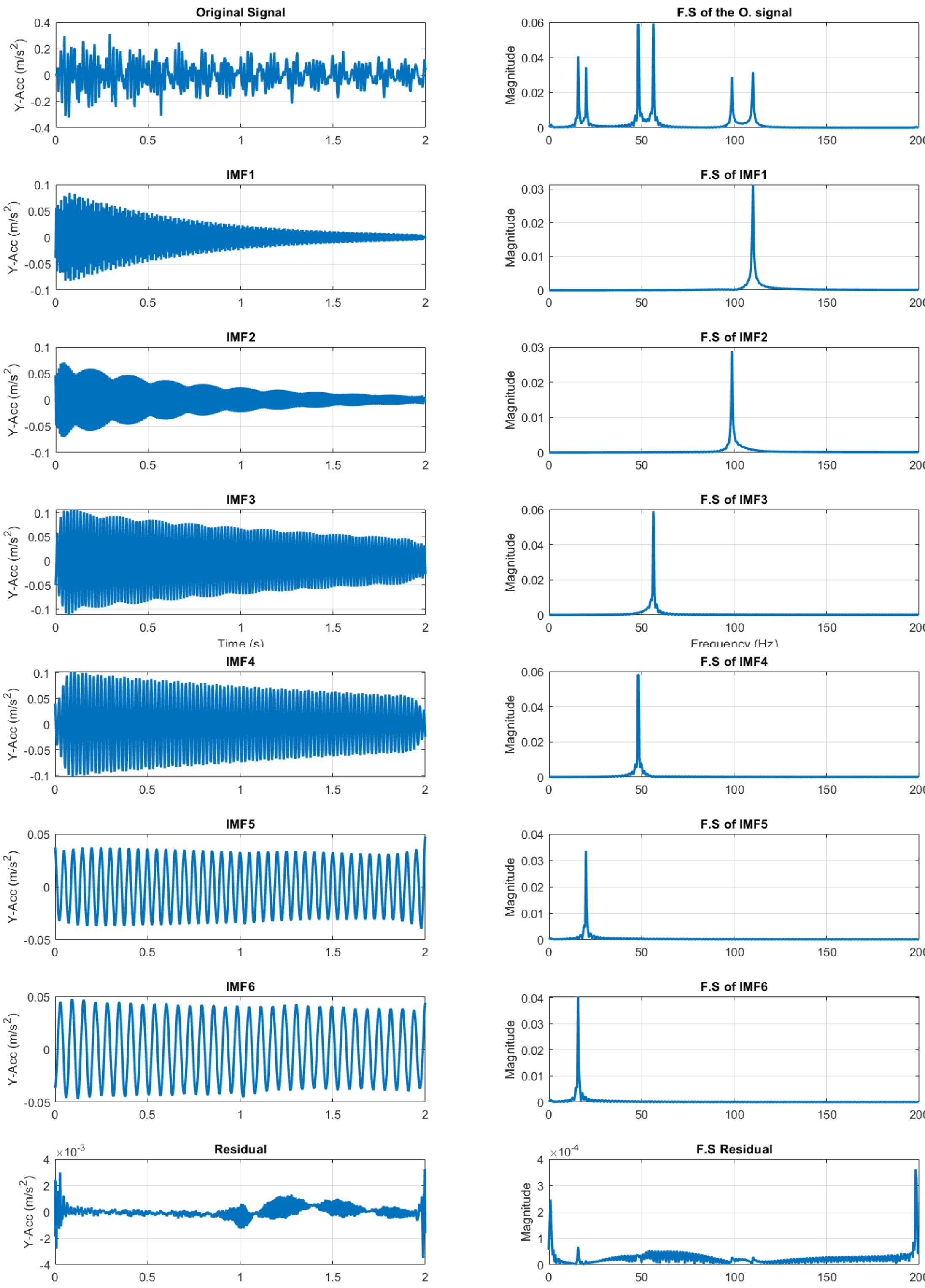

Original Signal
F.S of the O. signal
IMF1
F.S of IMF1
IMF2
F.S of IMF2
IMF3
F.S of IMF3
IMF4
F.S of IMF4
IMF5
F.S of IMF5
IMF6
F.S of IMF6
Residual
F.S Residual
Y-Acc (m/s^2)
Magnitude
Time (s)
Frequency (Hz)
$\times 10^{-3}$
$\times 10^{-4}$

S05

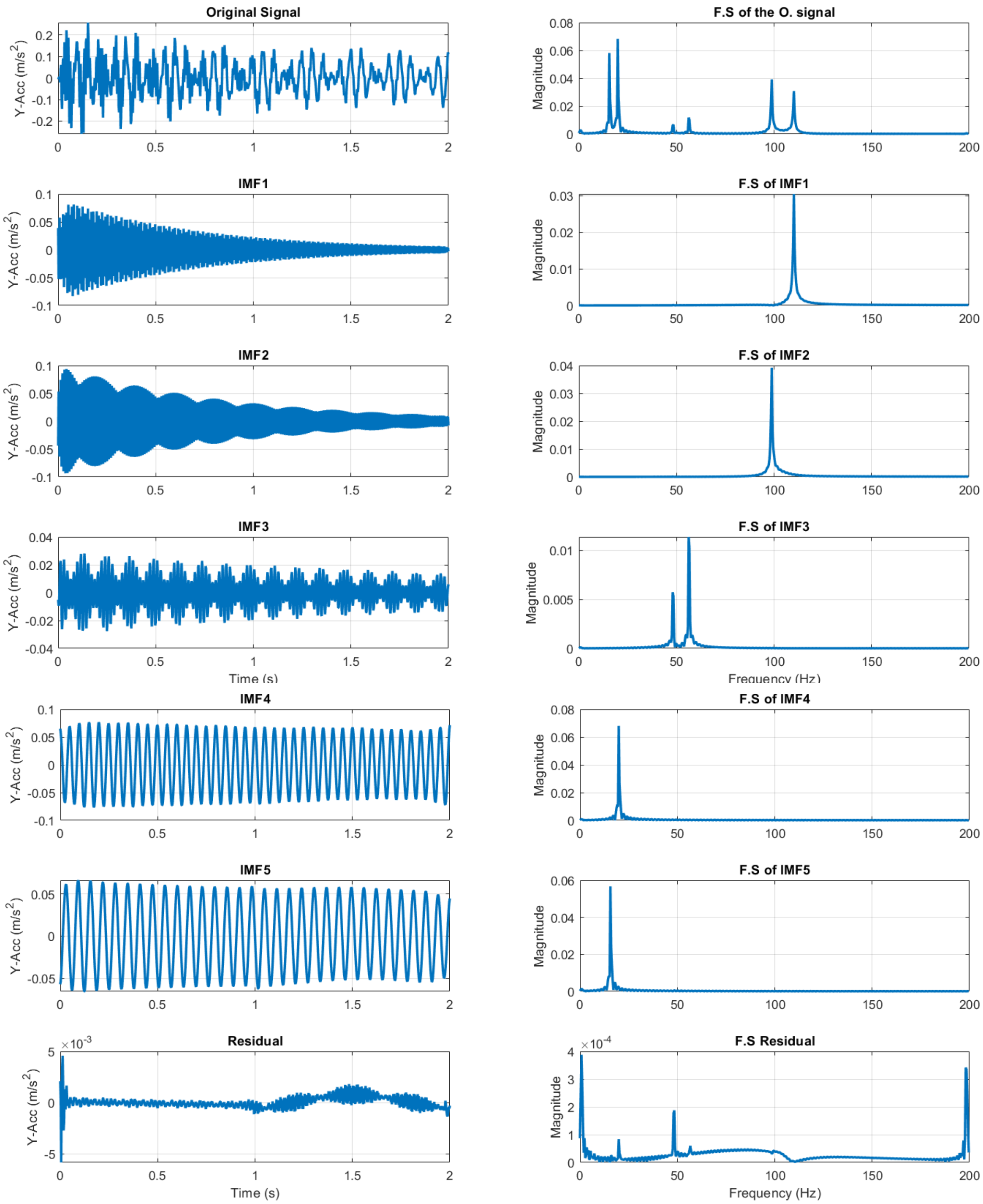
Original Signal
Y-Acc (m/s^2)
F.S of the O. signal
Magnitude
IMF1
F.S of IMF1
IMF2
F.S of IMF2
IMF3
F.S of IMF3
Time (s)
Frequency (Hz)
IMF4
F.S of IMF4
IMF5
F.S of IMF5
Residual
$\times 10^{-3}$
F.S Residual
$\times 10^{-4}$
Time (s)
Frequency (Hz)

S06

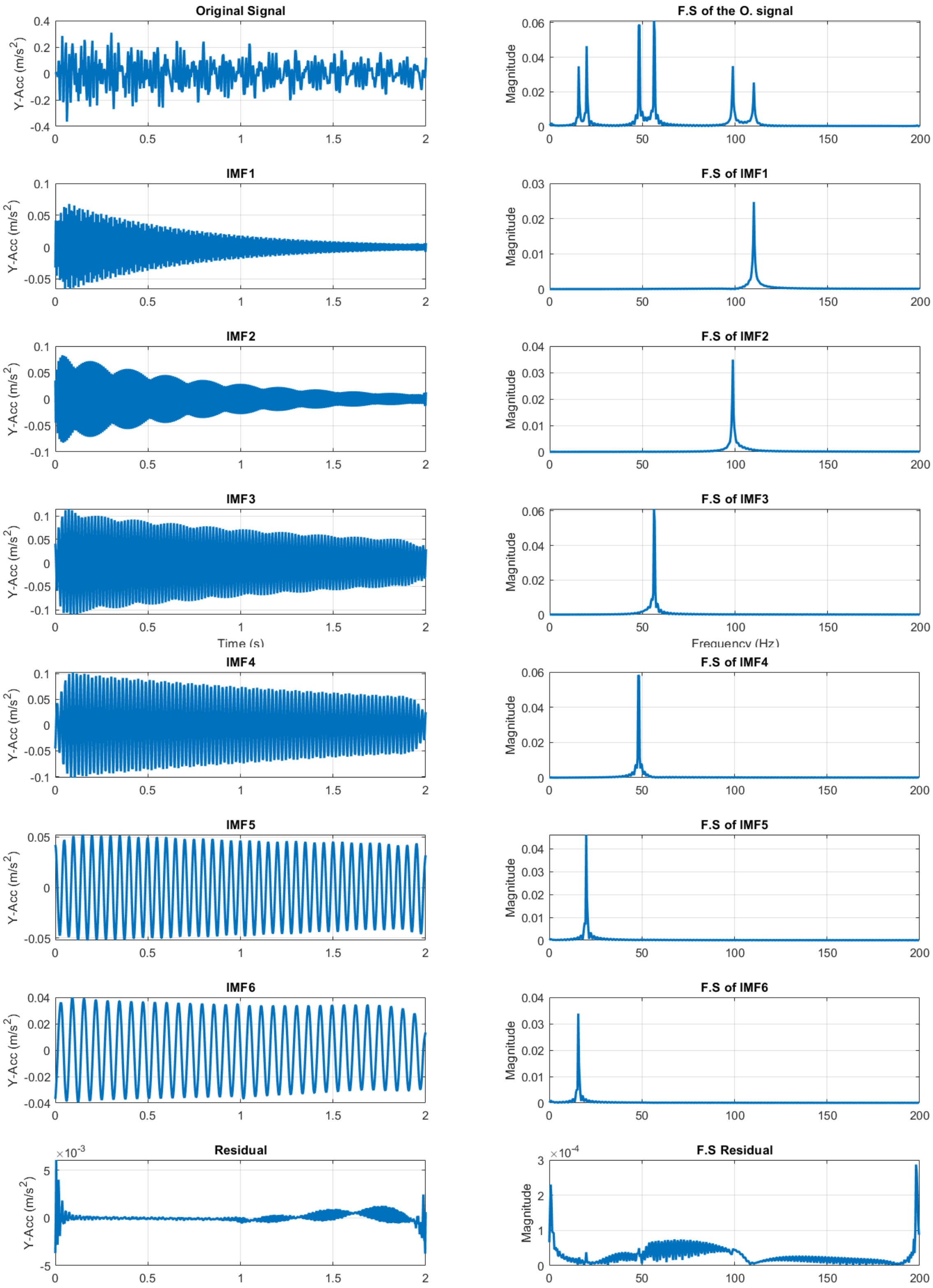
Original Signal
Y-Acc (m/s^2)
F.S of the O. signal
Magnitude
IMF1
F.S of IMF1
IMF2
F.S of IMF2
IMF3
F.S of IMF3
Time (s)
Frequency (Hz)
IMF4
F.S of IMF4
IMF5
F.S of IMF5
IMF6
F.S of IMF6
Residual
F.S Residual
$\times 10^{-3}$
$\times 10^{-4}$
Time (s)
Frequency (Hz)

DMG3, T= -15°C, D90%
S01

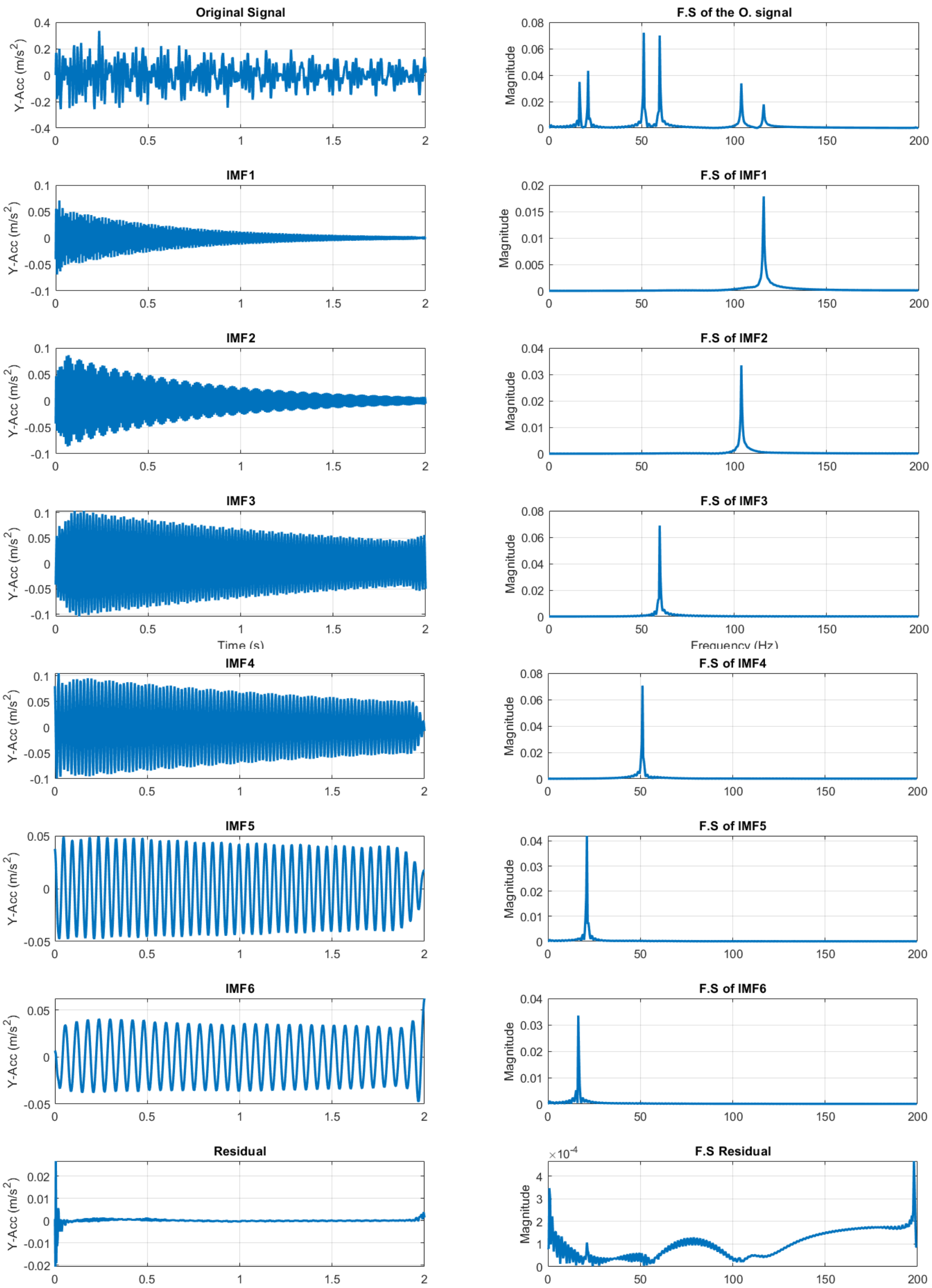

S02

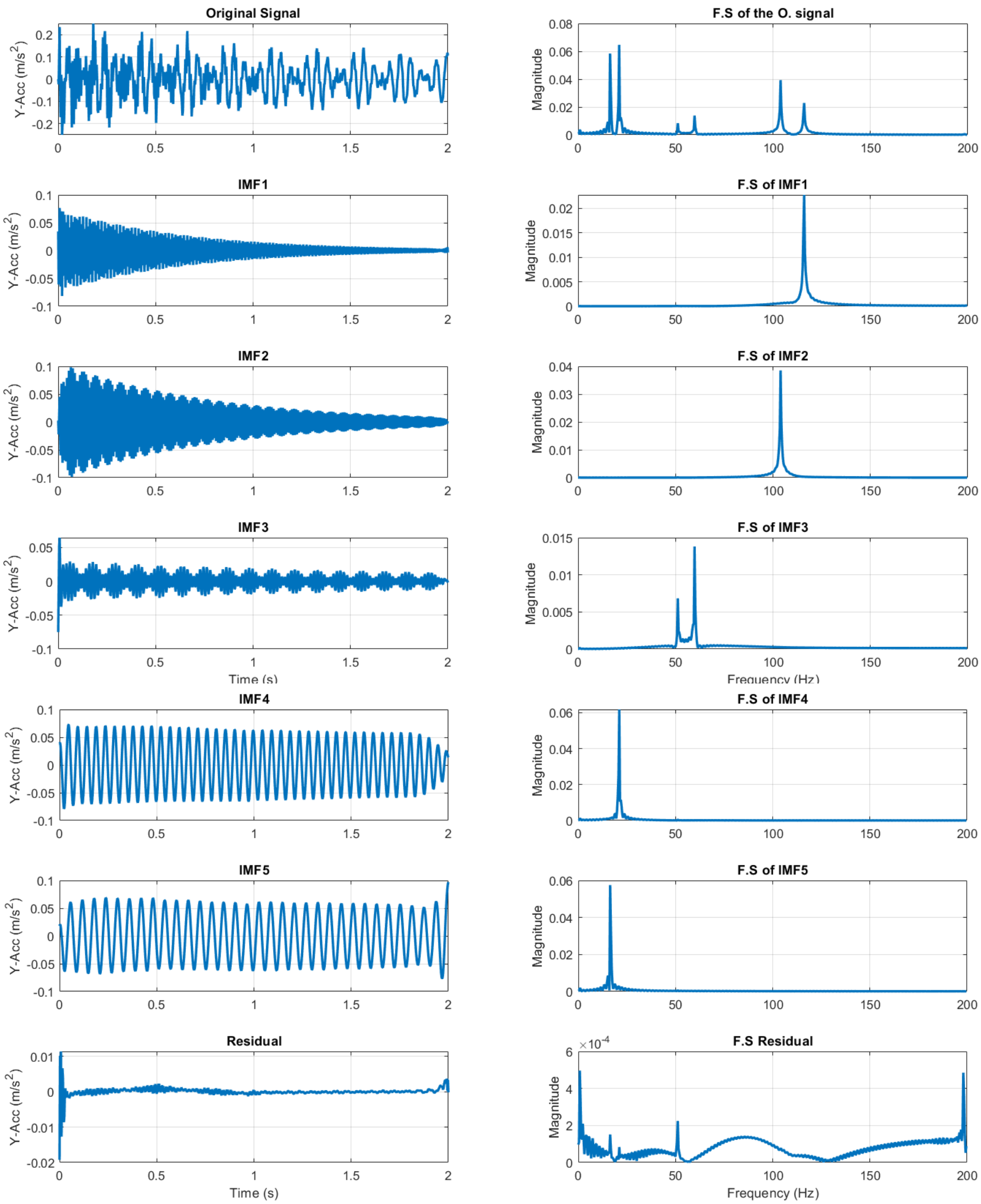

Original Signal
F.S of the O. signal
IMF1
F.S of IMF1
IMF2
F.S of IMF2
IMF3
F.S of IMF3
IMF4
F.S of IMF4
IMF5
F.S of IMF5
Residual
F.S Residual
Y-Acc (m/s^2)
Magnitude
Time (s)
Frequency (Hz)
$\times 10^{-4}$

S03

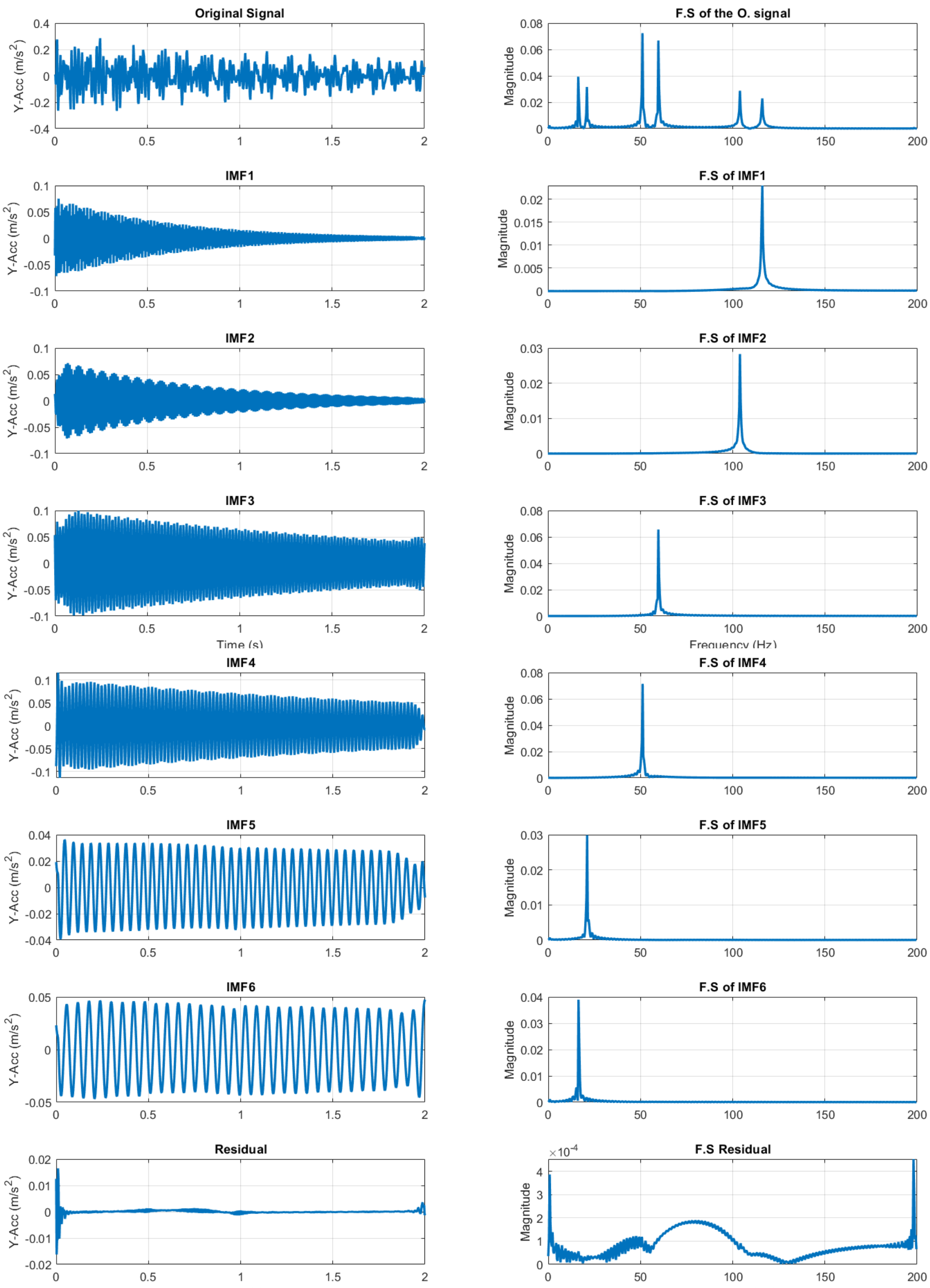
Original Signal
F.S of the O. signal
IMF1
F.S of IMF1
IMF2
F.S of IMF2
IMF3
F.S of IMF3
IMF4
F.S of IMF4
IMF5
F.S of IMF5
IMF6
F.S of IMF6
Residual
F.S Residual
Y-Acc (m/s2)
Magnitude
Time (s)
Frequency (Hz)
×10-4

S04

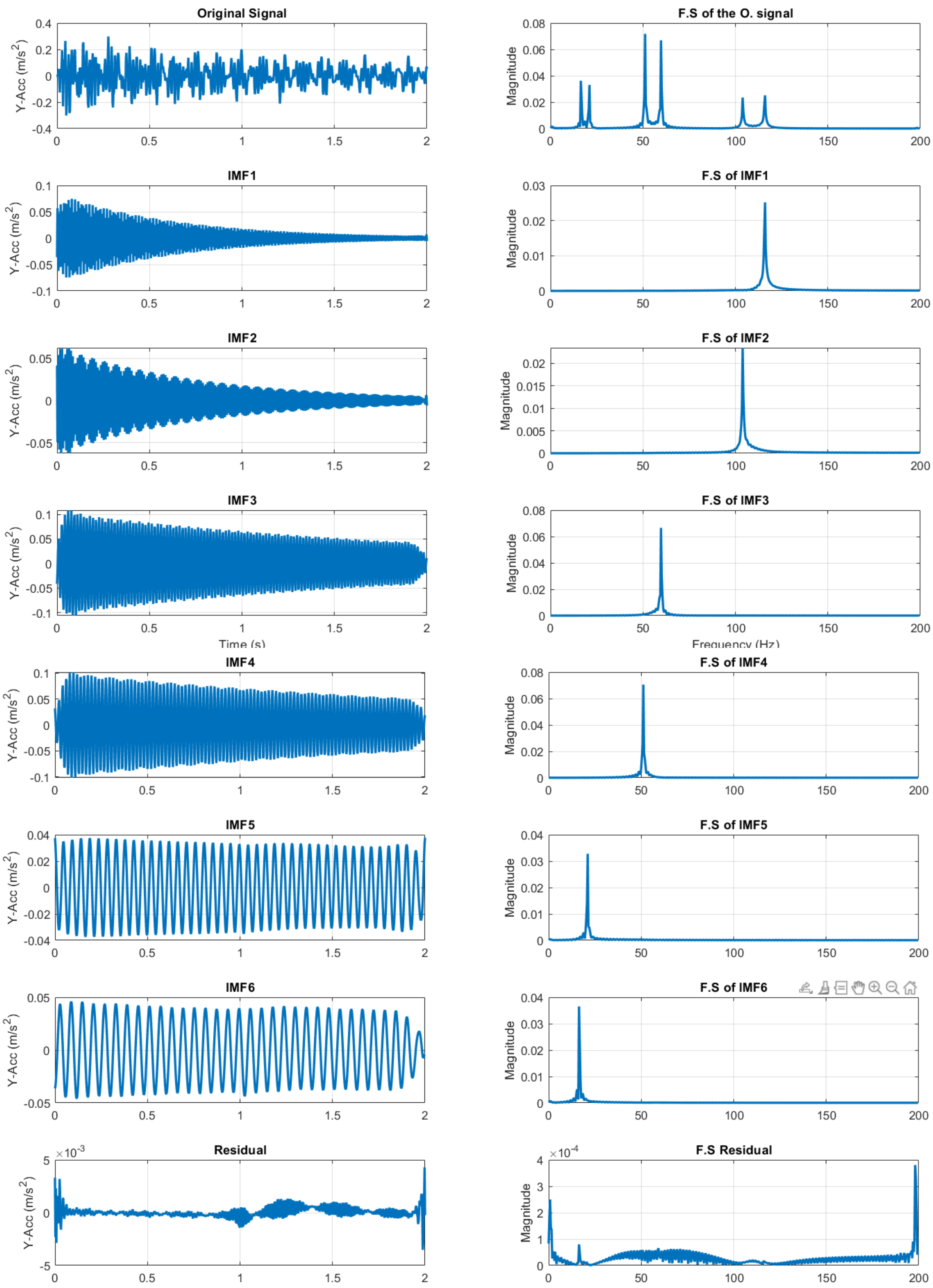
Original Signal
F.S of the O. signal
IMF1
F.S of IMF1
IMF2
F.S of IMF2
IMF3
F.S of IMF3
IMF4
F.S of IMF4
IMF5
F.S of IMF5
IMF6
F.S of IMF6
Residual
F.S Residual
Y-Acc (m/s^2)
Magnitude
Time (s)
Frequency (Hz)

S05

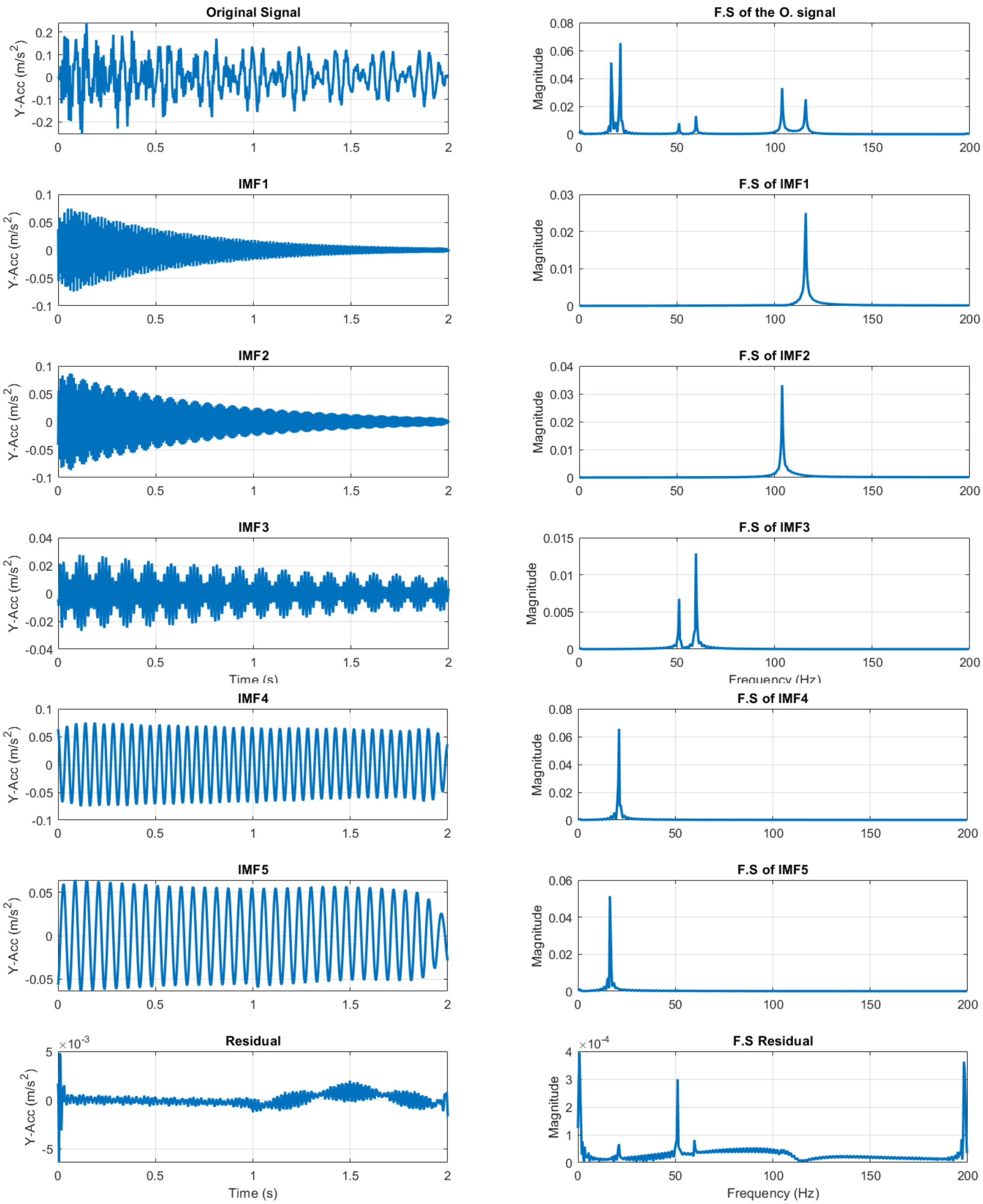

Original Signal
F.S of the O. signal
IMF1
F.S of IMF1
IMF2
F.S of IMF2
IMF3
F.S of IMF3
IMF4
F.S of IMF4
IMF5
F.S of IMF5
Residual
F.S Residual
Y-Acc (m/s^2)
Magnitude
Time (s)
Frequency (Hz)

S06

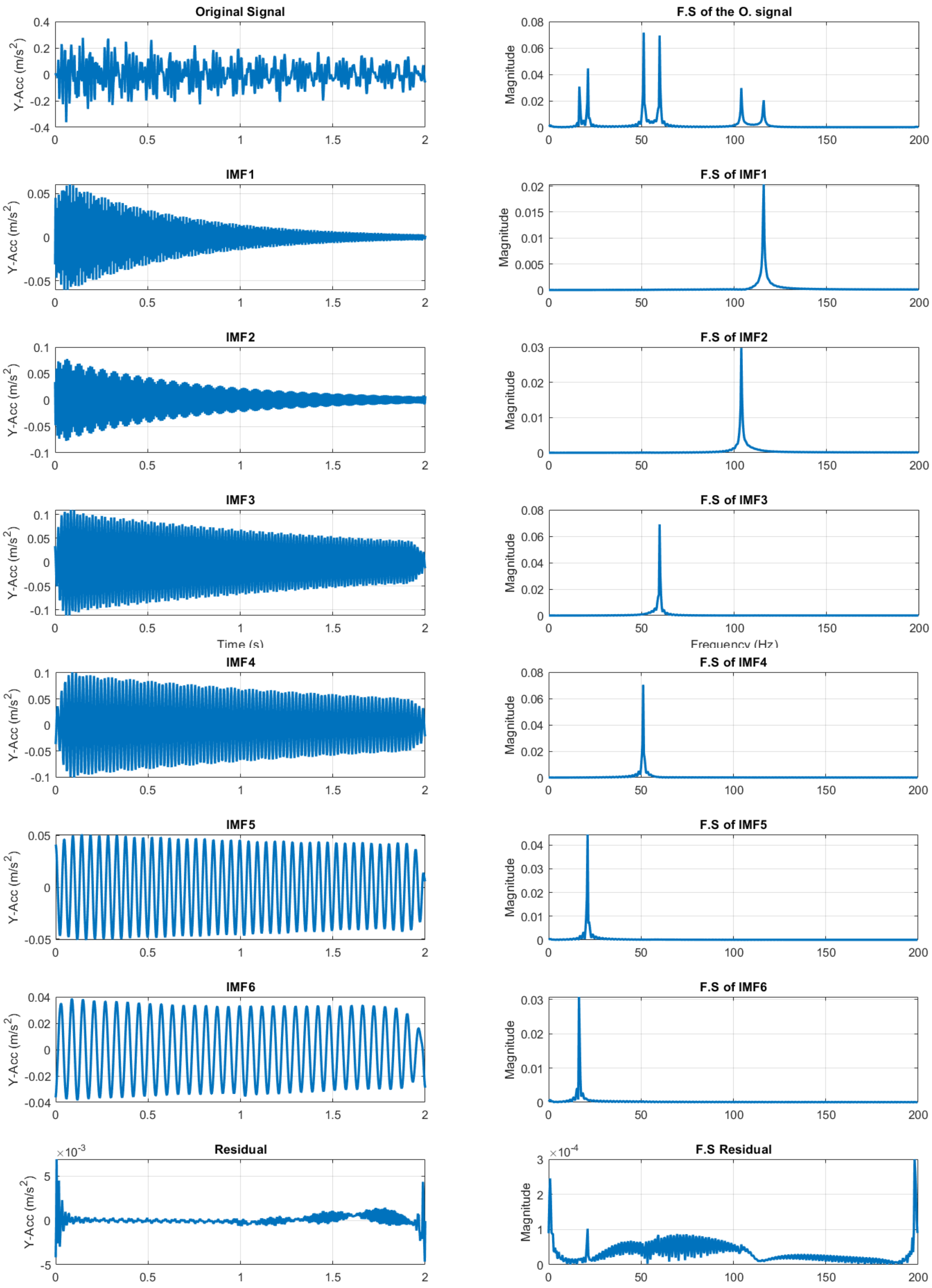

Original Signal
F.S of the O. signal
IMF1
F.S of IMF1
IMF2
F.S of IMF2
IMF3
F.S of IMF3
IMF4
F.S of IMF4
IMF5
F.S of IMF5
IMF6
F.S of IMF6
Residual
F.S Residual
Y-Acc (m/s^2)
Magnitude
Time (s)
Frequency (Hz)

DMG3, T= 20°C, D90%
S01

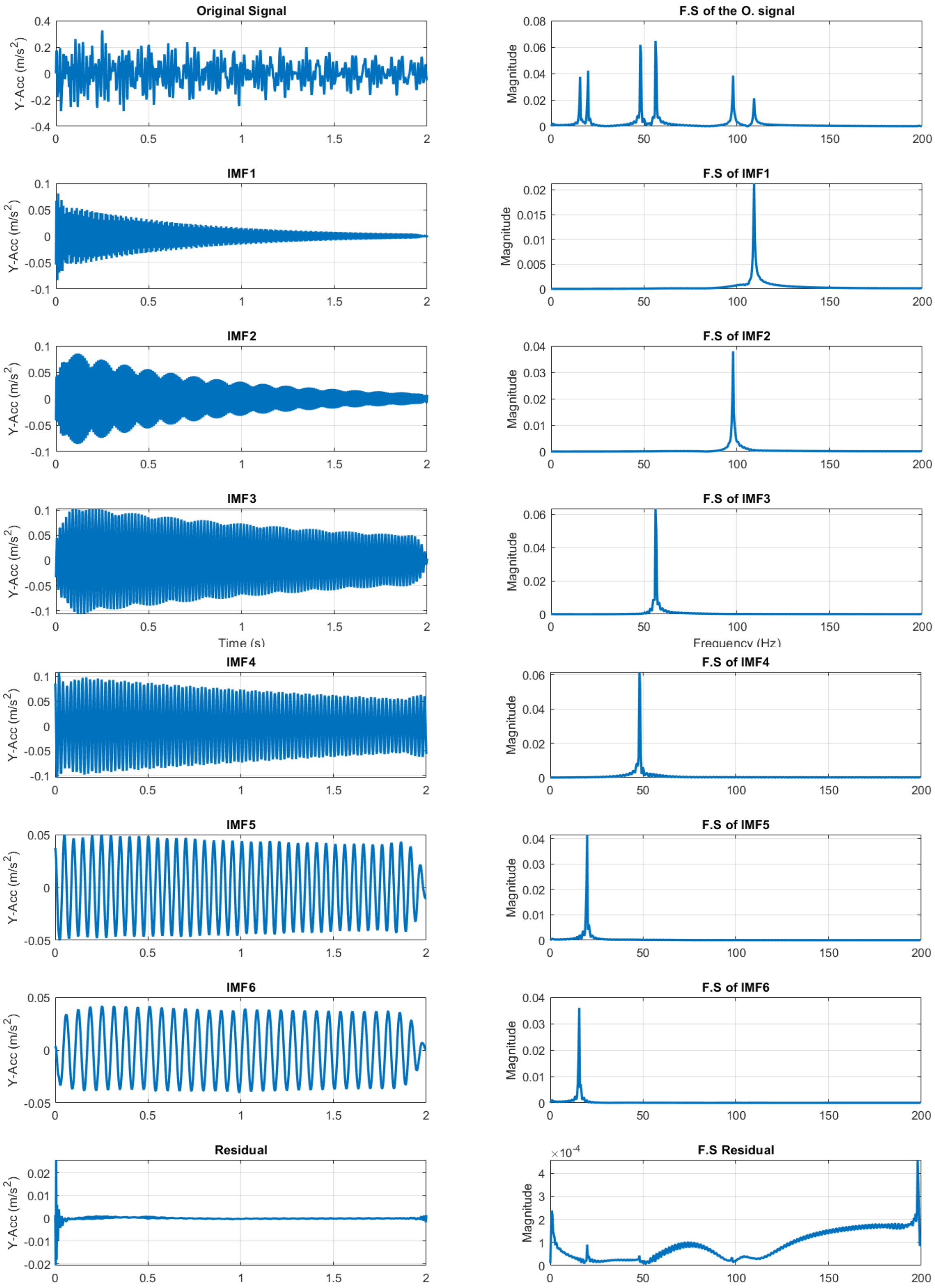

S02

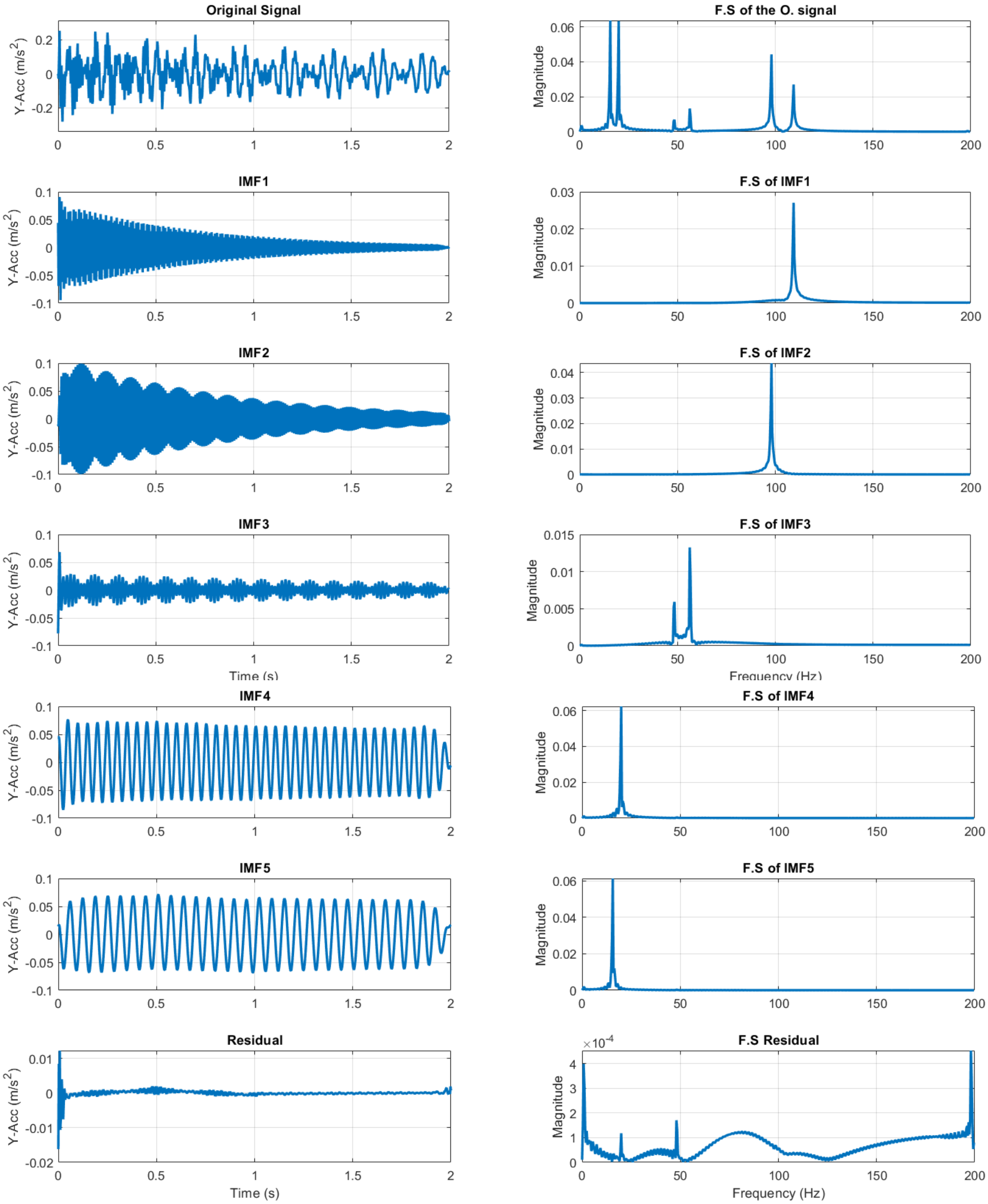
Original Signal
F.S of the O. signal
IMF1
F.S of IMF1
IMF2
F.S of IMF2
IMF3
F.S of IMF3
IMF4
F.S of IMF4
IMF5
F.S of IMF5
Residual
F.S Residual
Y-Acc (m/s^2)
Magnitude
Time (s)
Frequency (Hz)

S03

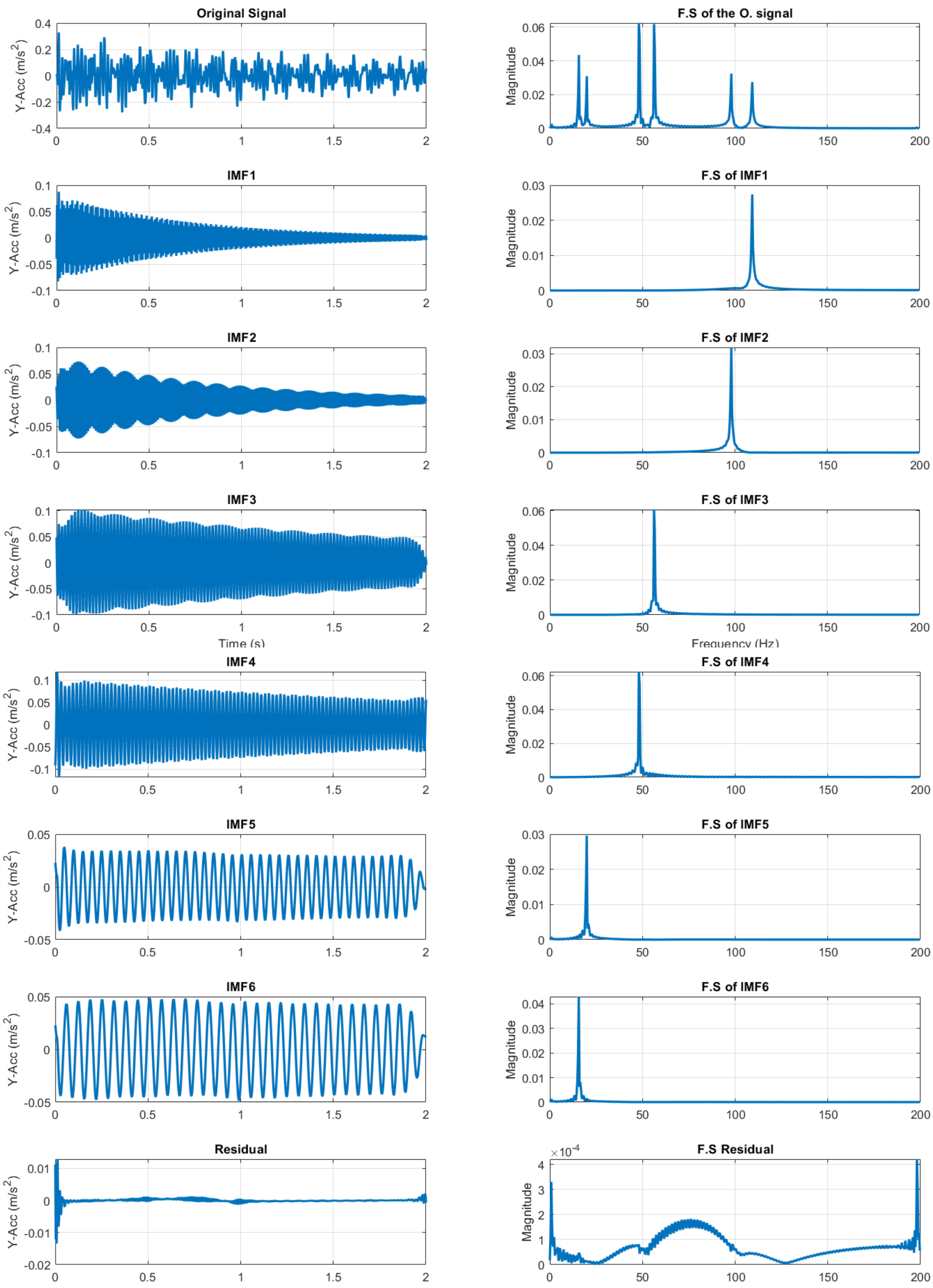
Original Signal
F.S of the O. signal
IMF1
F.S of IMF1
IMF2
F.S of IMF2
IMF3
F.S of IMF3
IMF4
F.S of IMF4
IMF5
F.S of IMF5
IMF6
F.S of IMF6
Residual
F.S Residual
Y-Acc (m/s^2)
Magnitude
Time (s)
Frequency (Hz)
$\times 10^{-4}$

S04

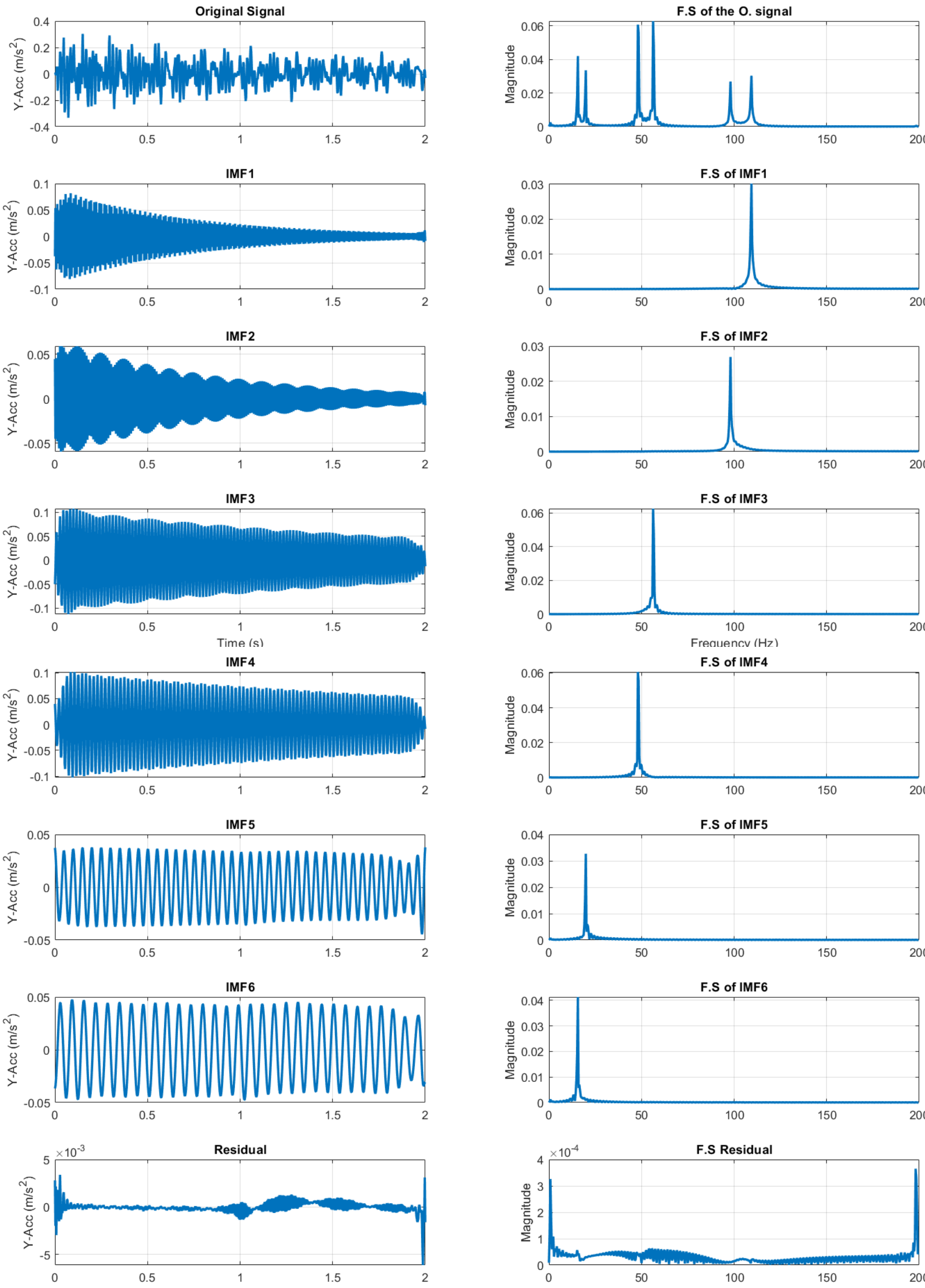
Original Signal
F.S of the O. signal
IMF1
F.S of IMF1
IMF2
F.S of IMF2
IMF3
F.S of IMF3
IMF4
F.S of IMF4
IMF5
F.S of IMF5
IMF6
F.S of IMF6
Residual
F.S Residual
Y-Acc (m/s^2)
Magnitude
Time (s)
Frequency (Hz)
×10^{-3}
×10^{-4}

S05

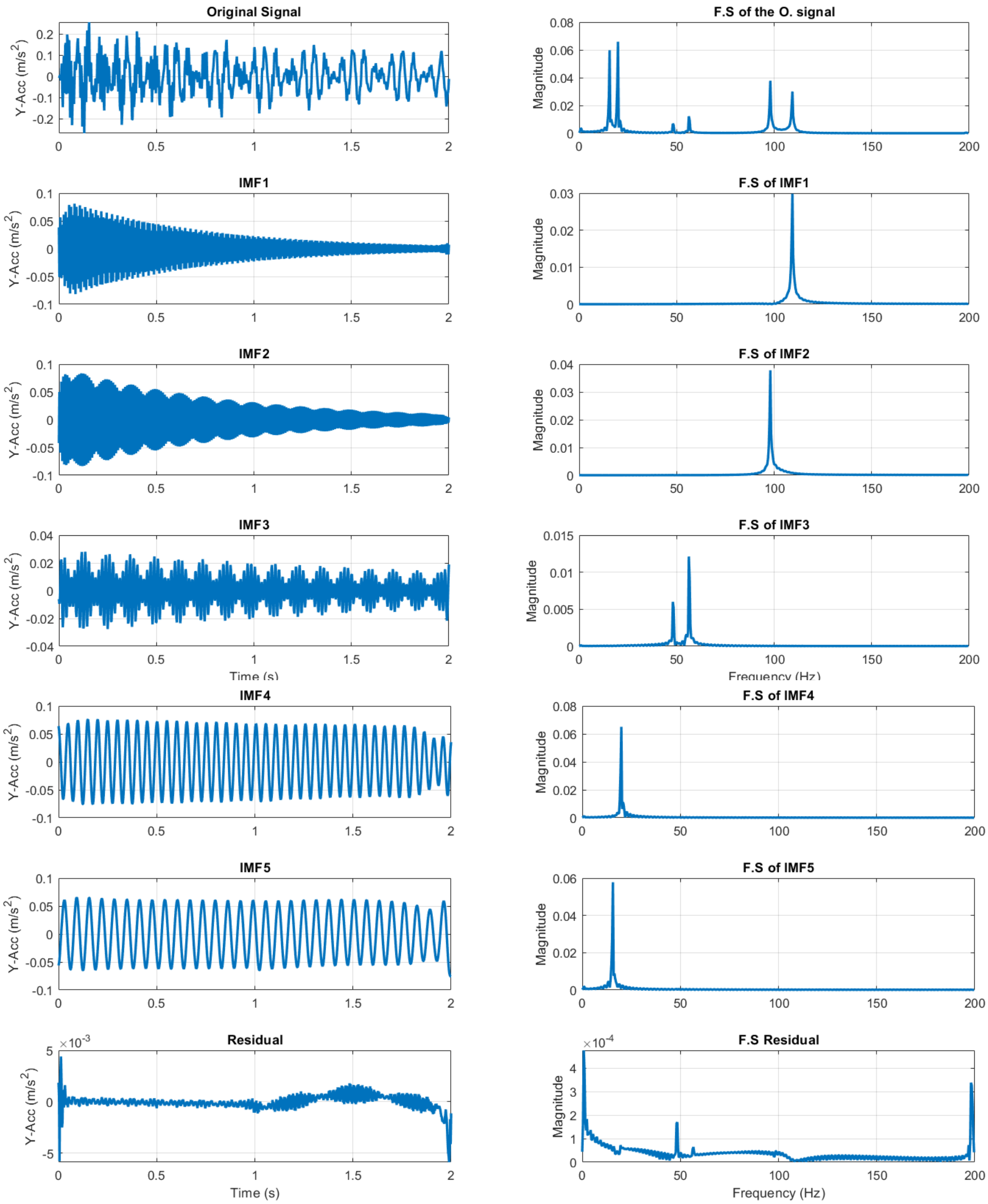

Original Signal
F.S of the O. signal
IMF1
F.S of IMF1
IMF2
F.S of IMF2
IMF3
F.S of IMF3
IMF4
F.S of IMF4
IMF5
F.S of IMF5
Residual
F.S Residual
Y-Acc (m/s^2)
Magnitude
Time (s)
Frequency (Hz)

S06

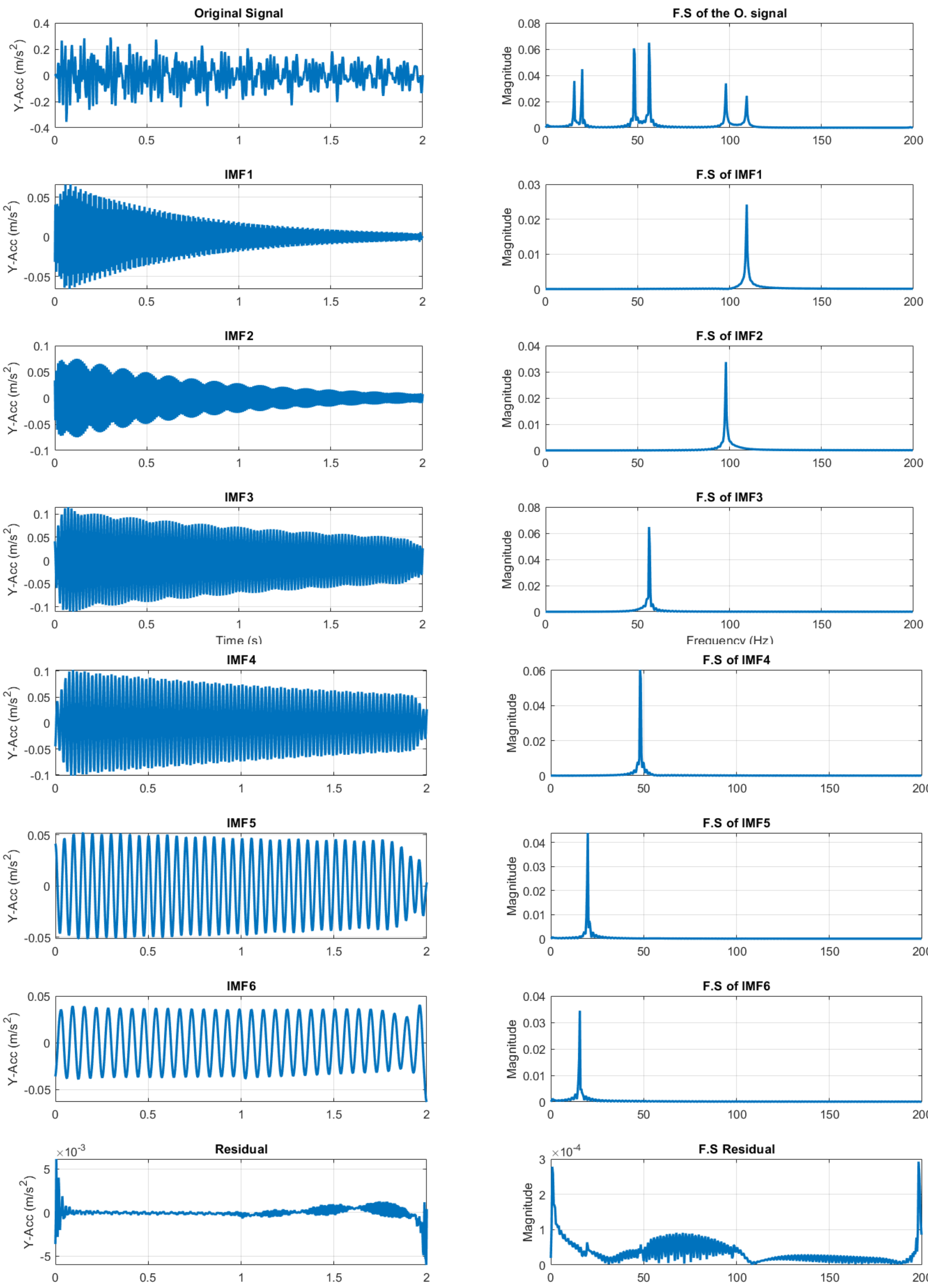
Original Signal
Y-Acc (m/s^2)
F.S of the O. signal
Magnitude
IMF1
F.S of IMF1
IMF2
F.S of IMF2
IMF3
F.S of IMF3
Time (s)
Frequency (Hz)
IMF4
F.S of IMF4
IMF5
F.S of IMF5
IMF6
F.S of IMF6
Residual
F.S Residual
×10^{-3}
×10^{-4}

Appendix C

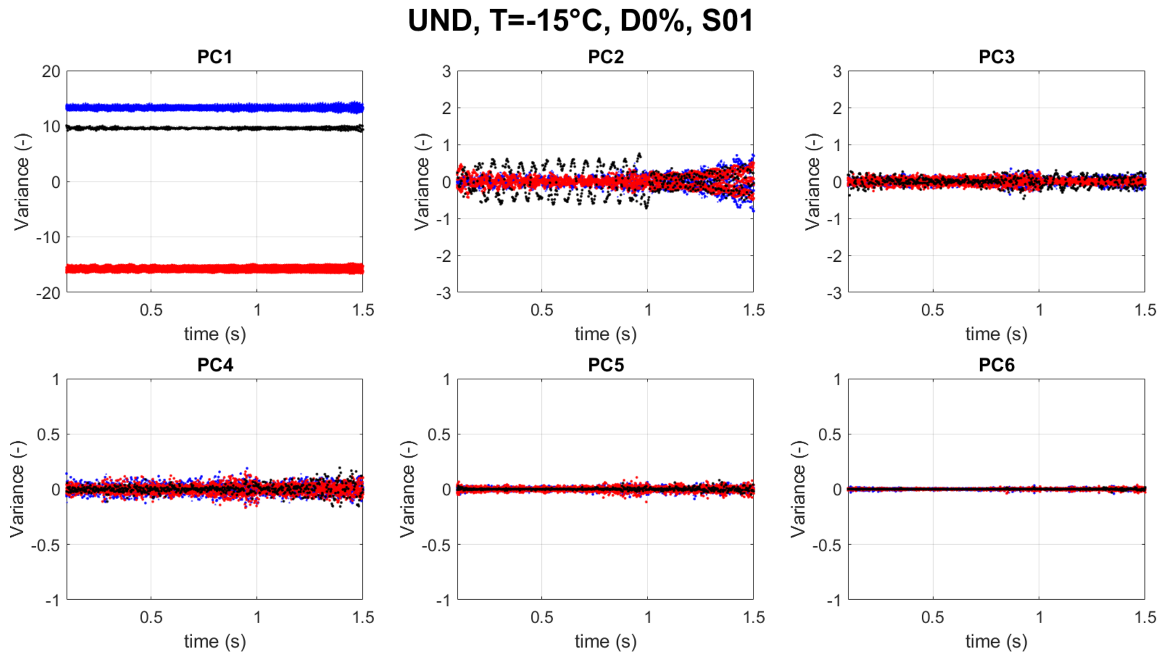
UND, T=-15°C, D0%, S01
PC1
PC2
PC3
PC4
PC5
PC6
Variance (-)
time (s)

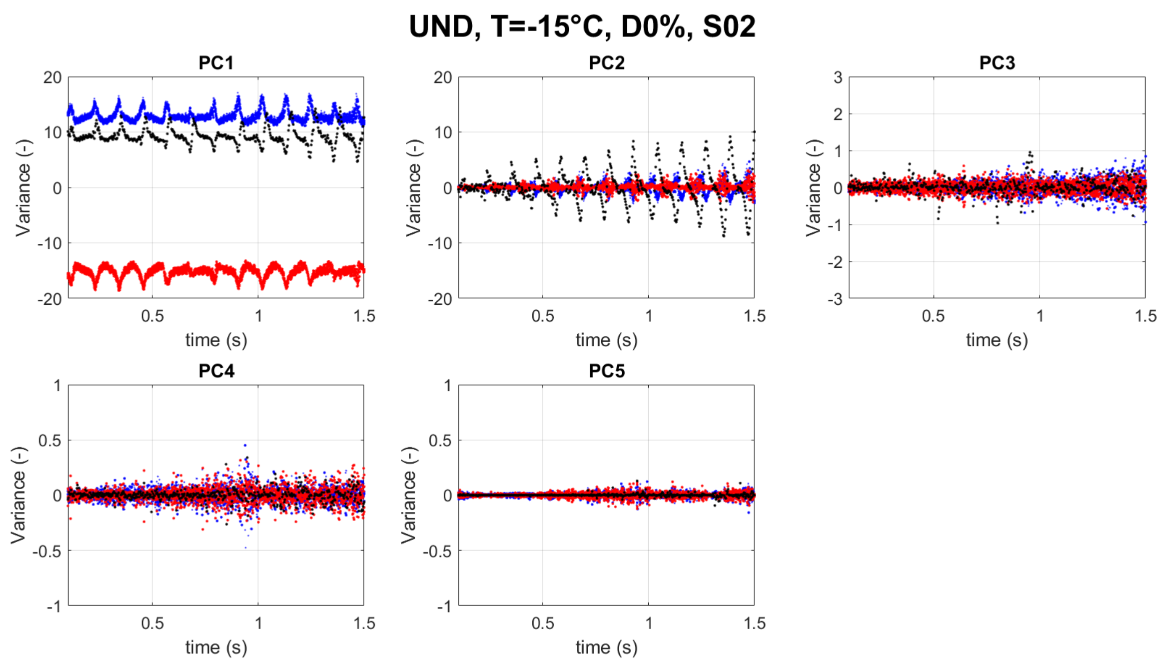
UND, T=-15°C, D0%, S02
PC1
PC2
PC3
PC4
PC5
Variance (-)
time (s)

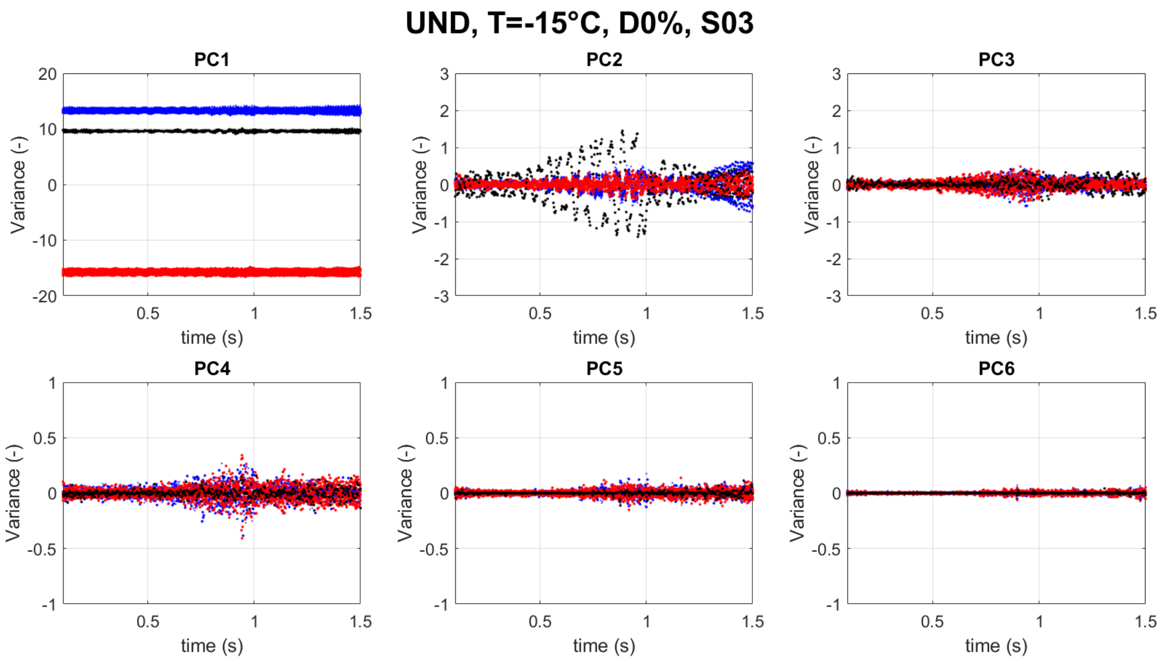

UND, T=-15°C, D0%, S03
PC1
PC2
PC3
PC4
PC5
PC6
Variance (-)
time (s)

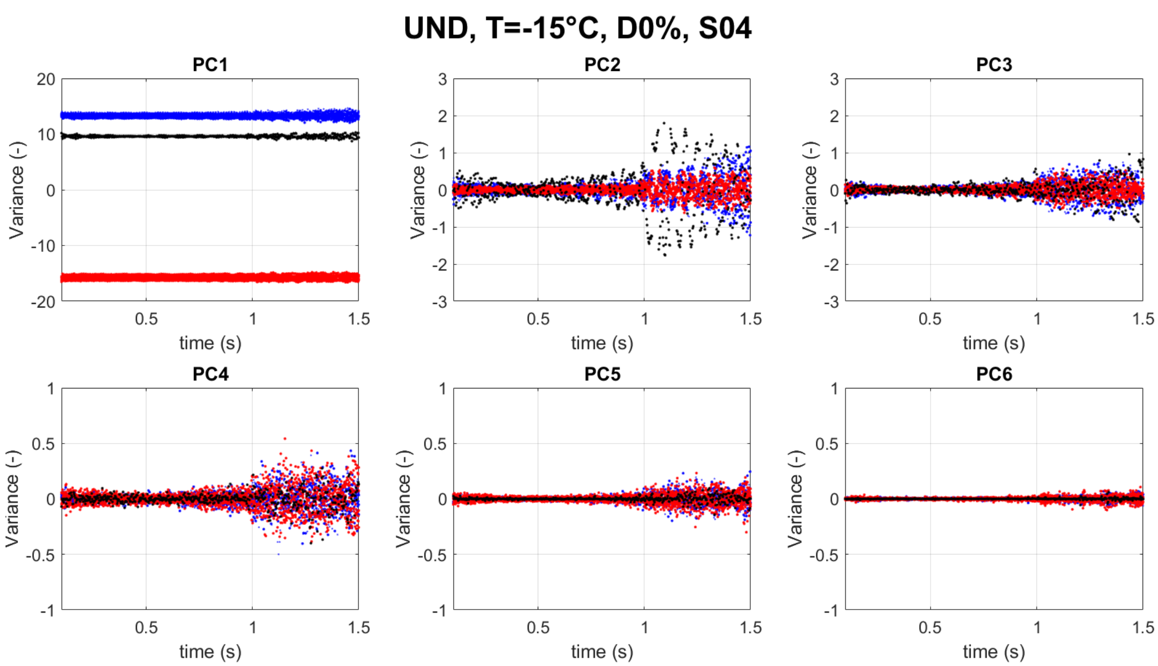

UND, T=-15°C, D0%, S04
PC1
PC2
PC3
PC4
PC5
PC6
Variance (-)
time (s)

UND, T=-15°C, D0%, S05

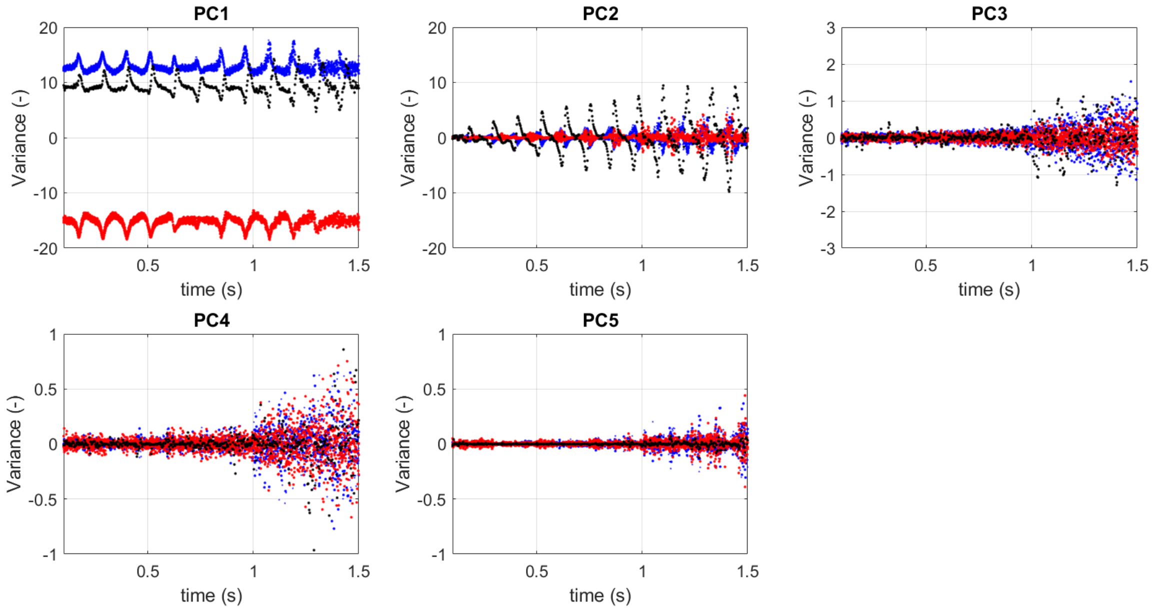

UND, T=-15°C, D0%, S06

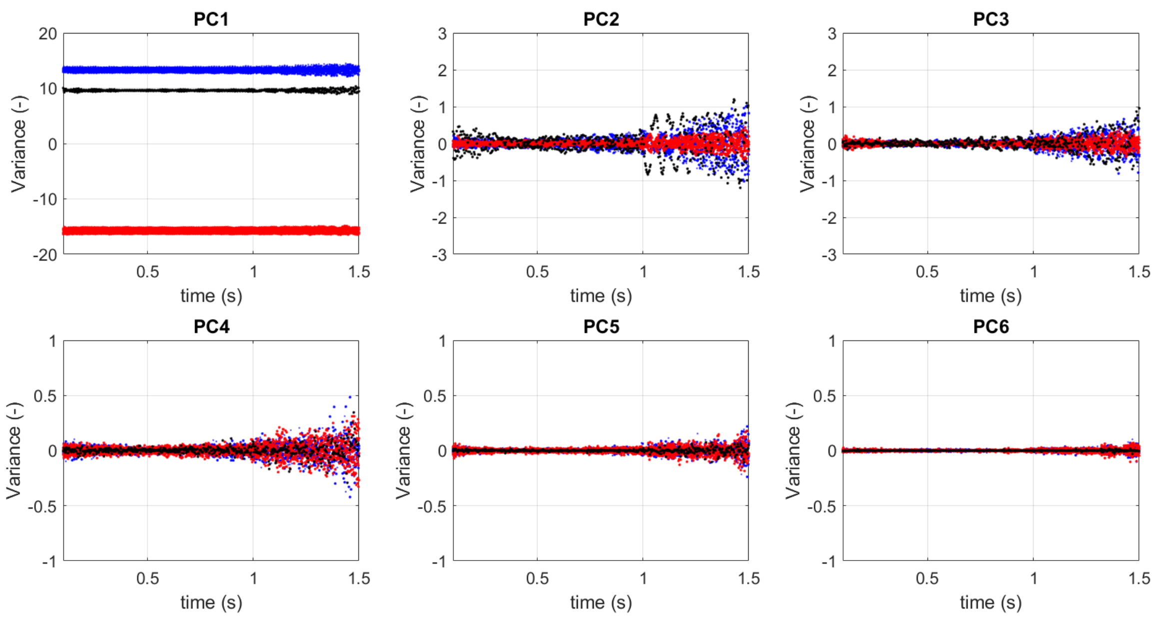

UND, T=20°C, D0%, S01

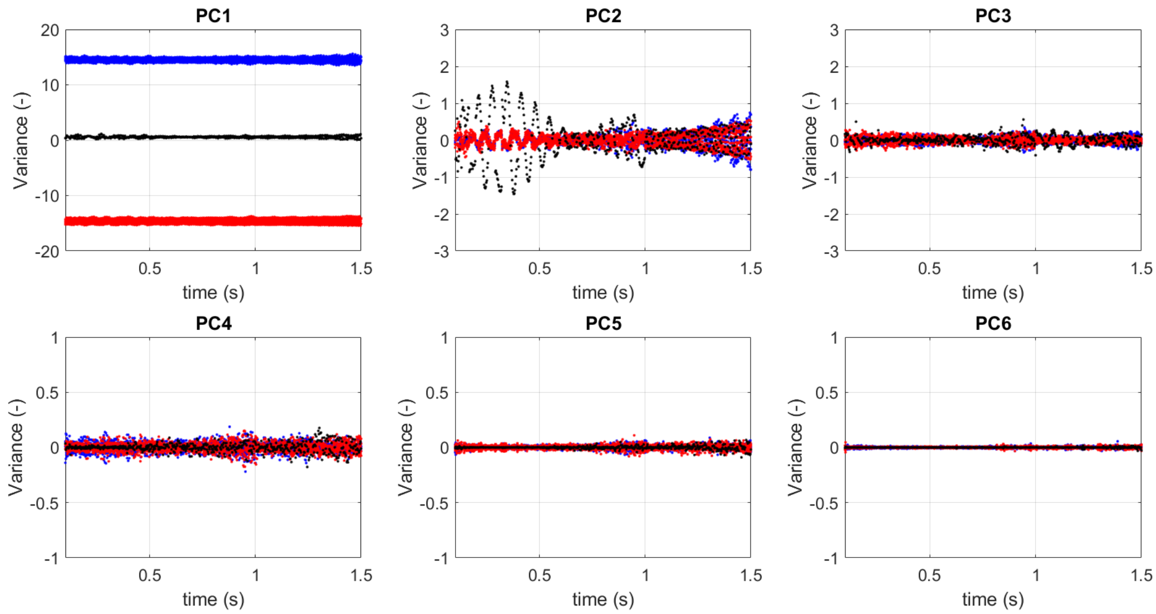

UND, T=20°C, D0%, S02

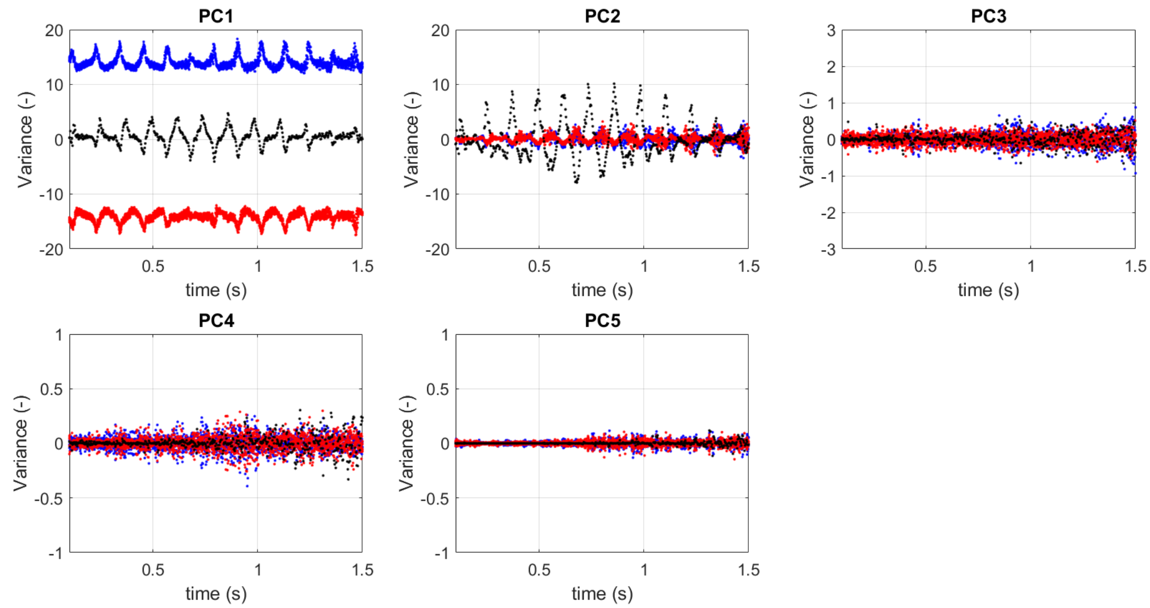

UND, T=20°C, D0%, S03

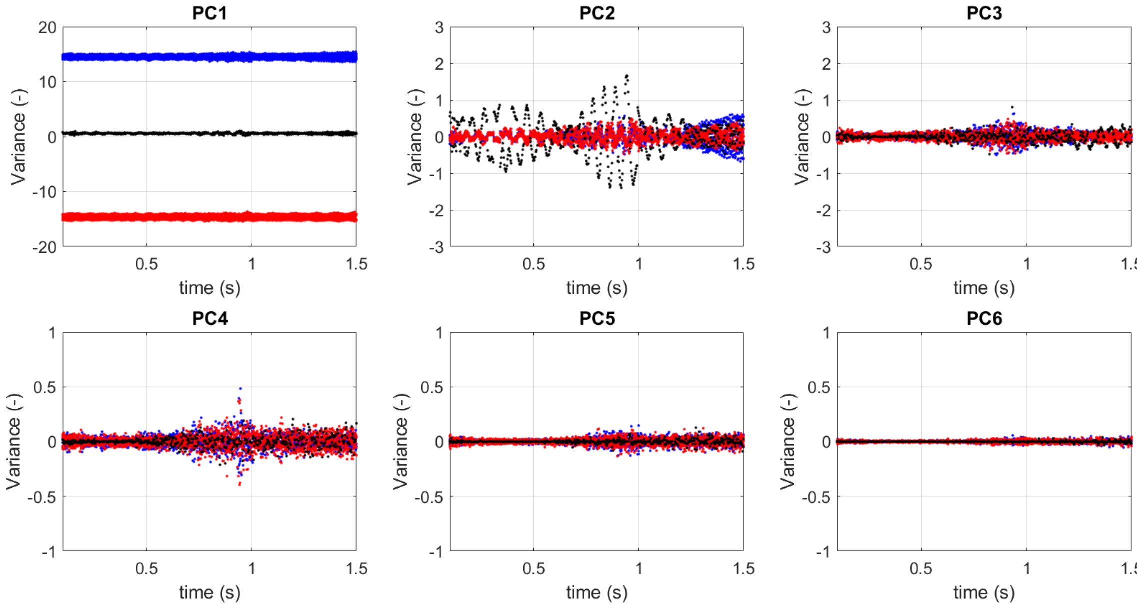

UND, T=20°C, D0%, S04

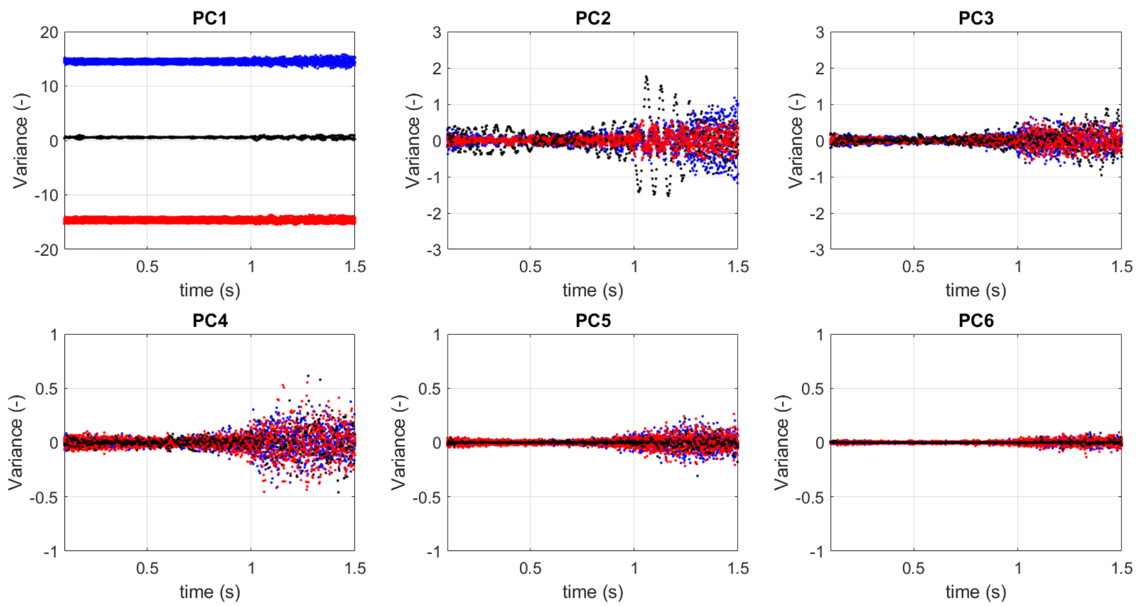

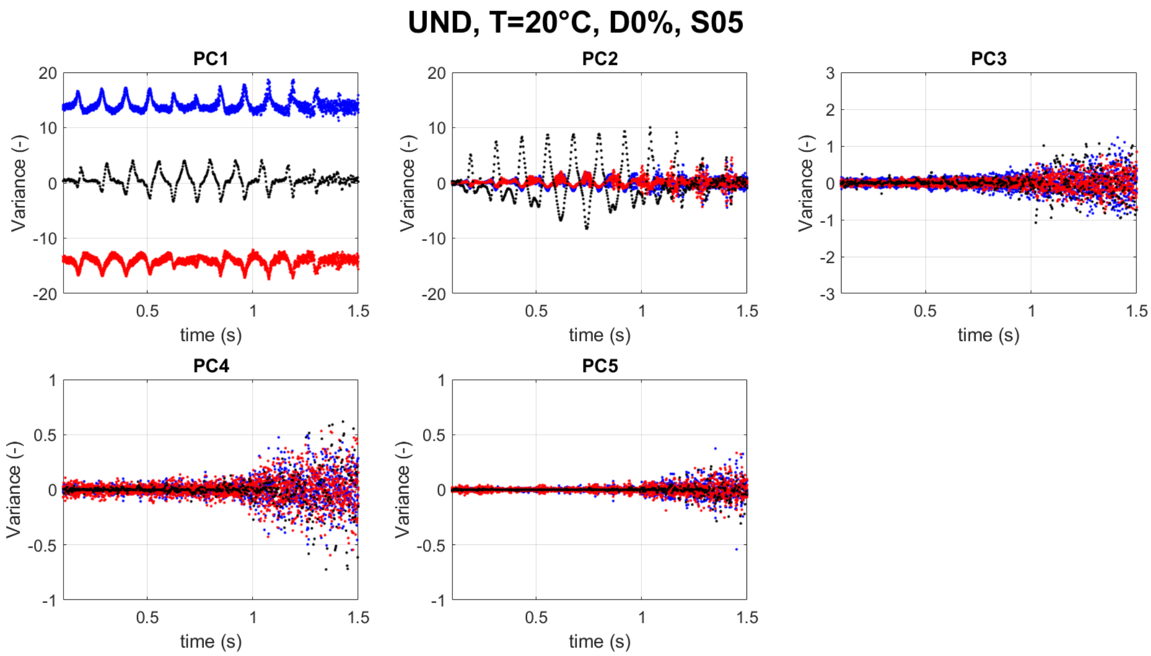
UND, T=20°C, D0%, S05
PC1
PC2
PC3
PC4
PC5
Variance (-)
time (s)

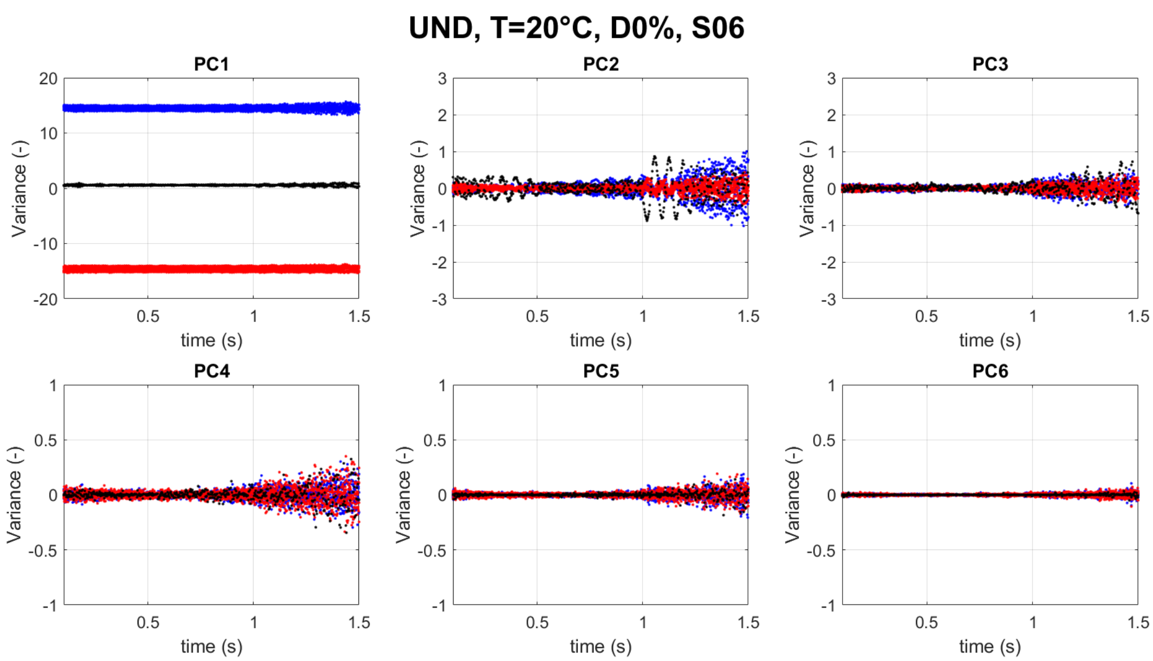
UND, T=20°C, D0%, S06
PC1
PC2
PC3
PC4
PC5
PC6
Variance (-)
time (s)

DMG3, T=20°C, D90%, S01

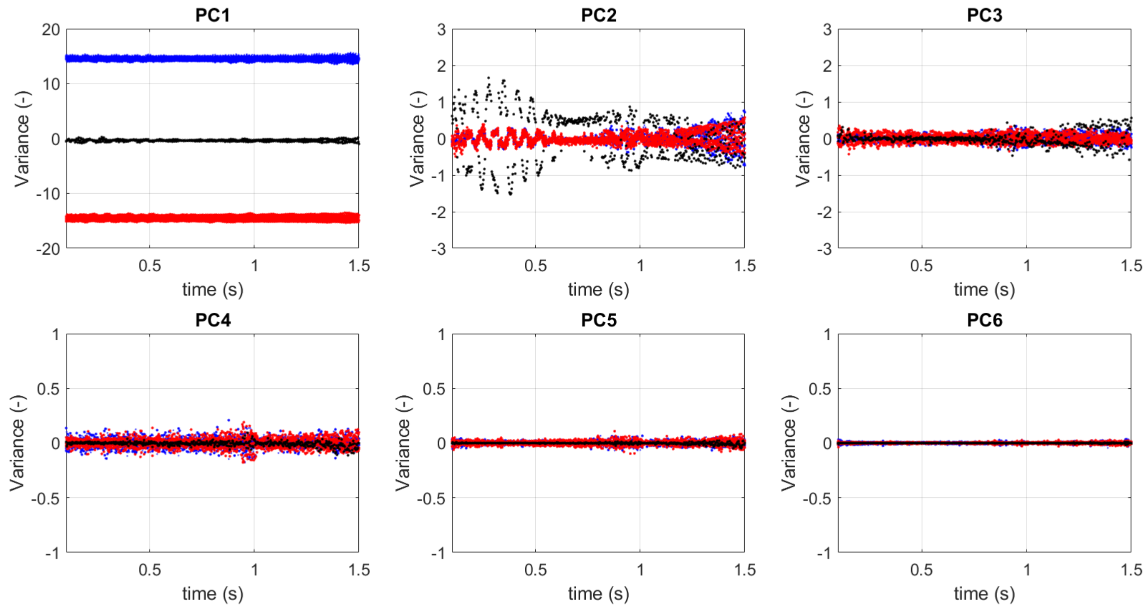

DMG3, T=20°C, D90%, S02

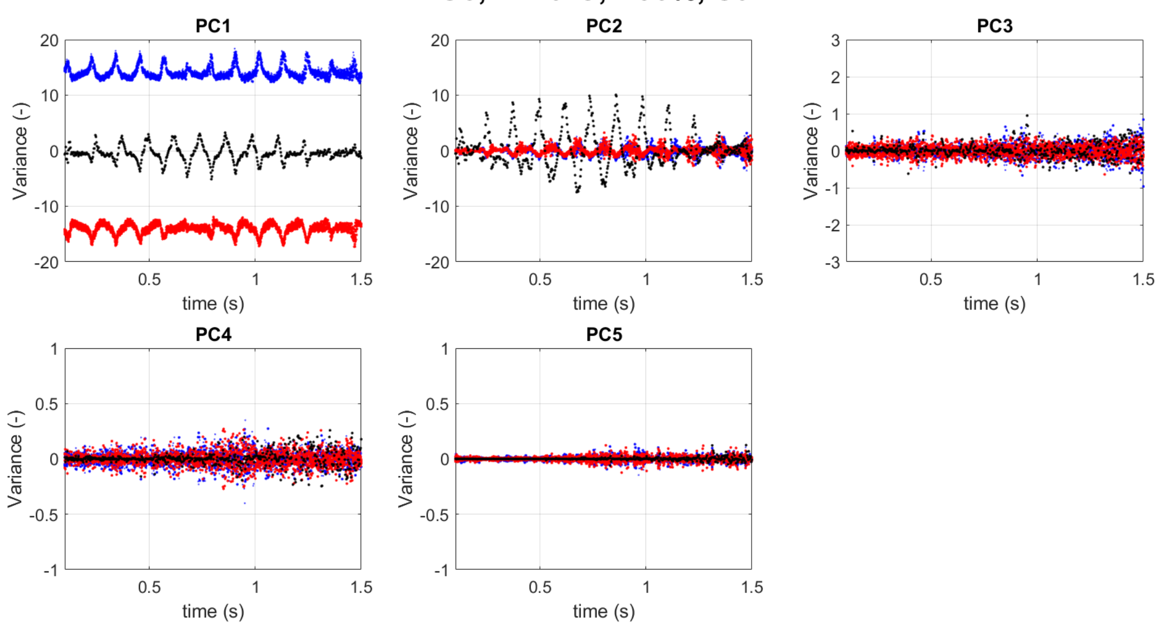

DMG3, T=20°C, D90%, S03

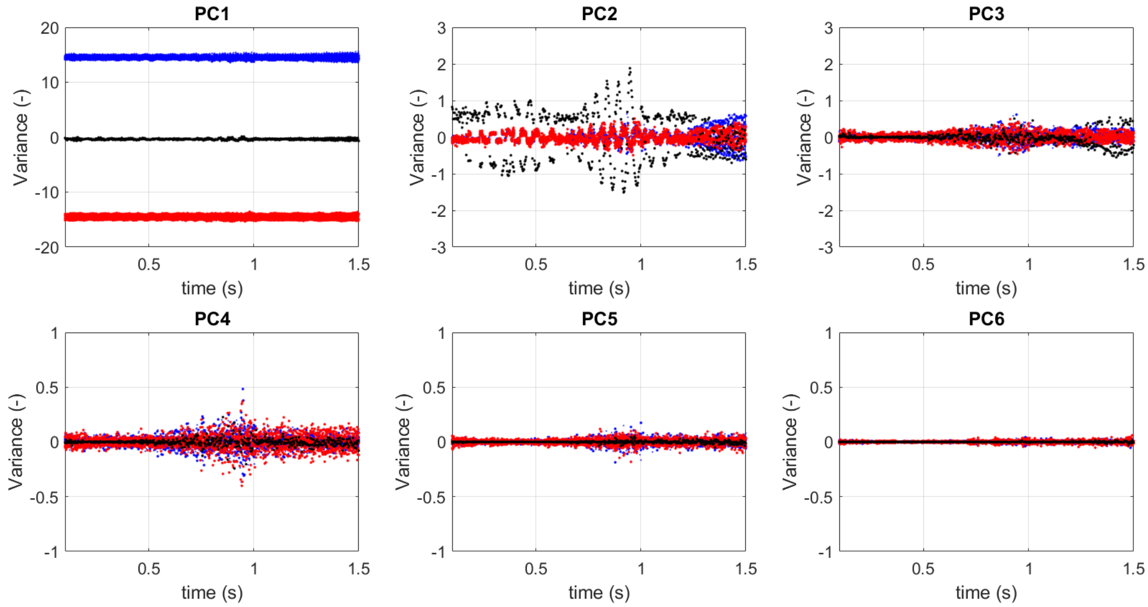

DMG3, T=20°C, D90%, S04

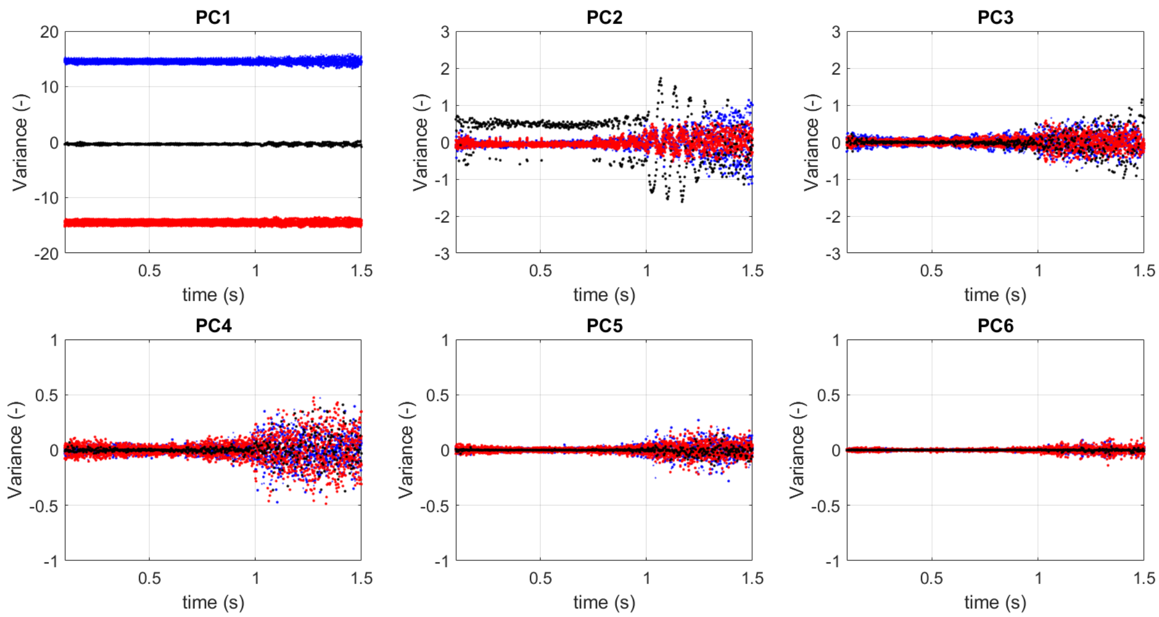

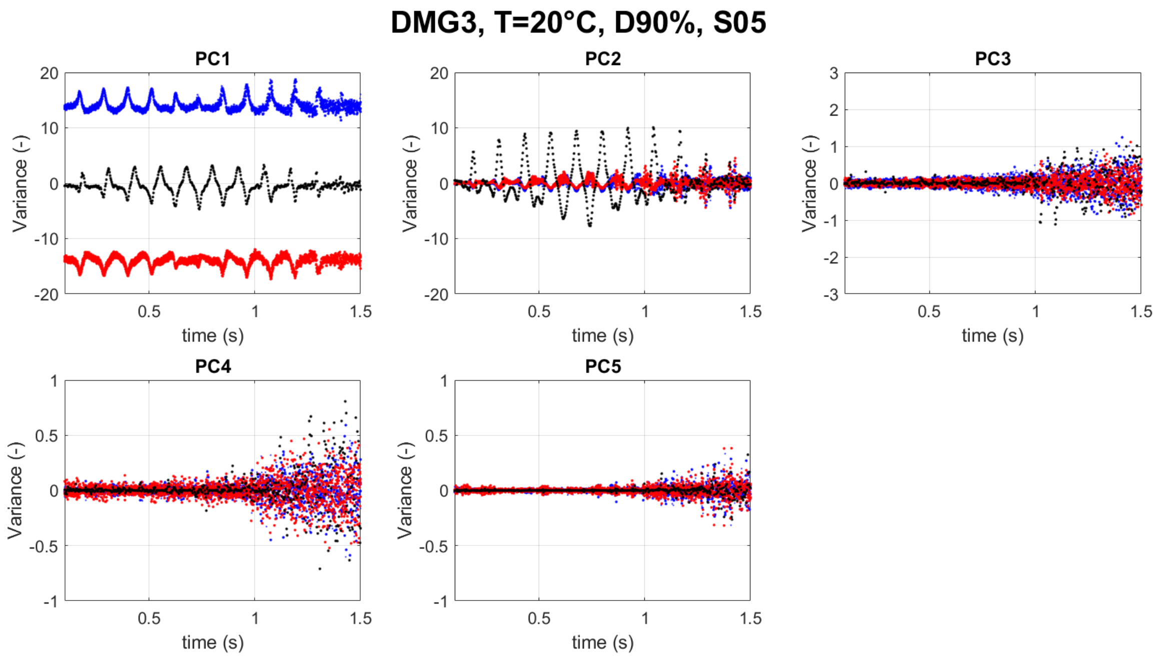
DMG3, T=20°C, D90%, S05
PC1
PC2
PC3
PC4
PC5
Variance (-)
time (s)

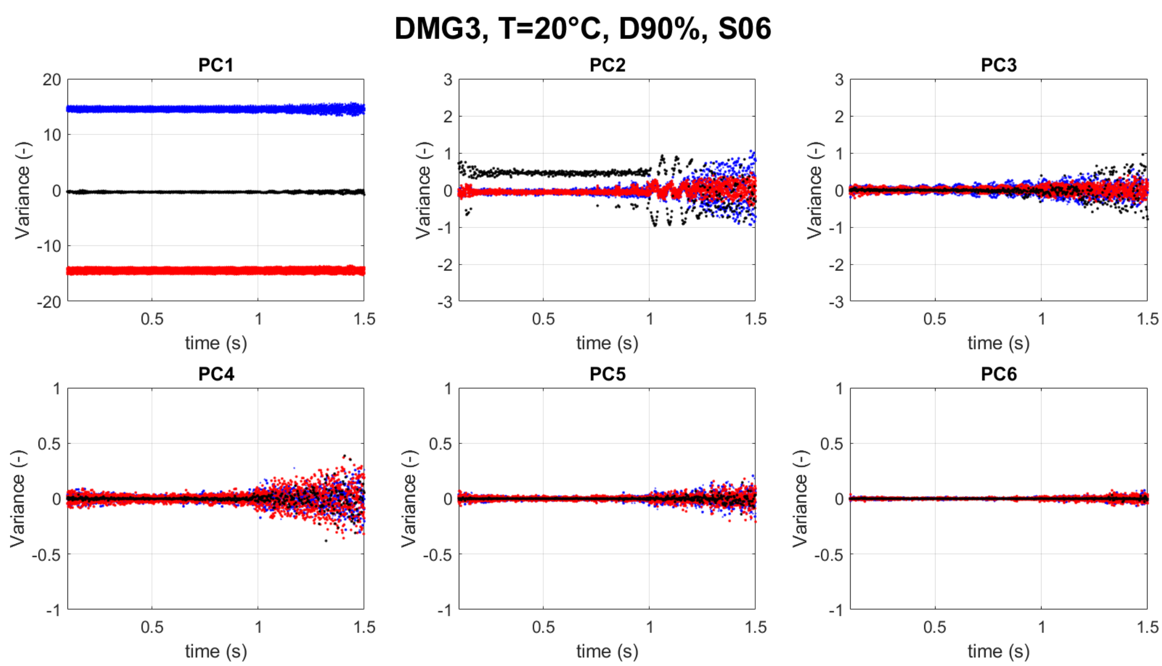
DMG3, T=20°C, D90%, S06
PC1
PC2
PC3
PC4
PC5
PC6
Variance (-)
time (s)

DMG3, T=-15°C, D90%, S01

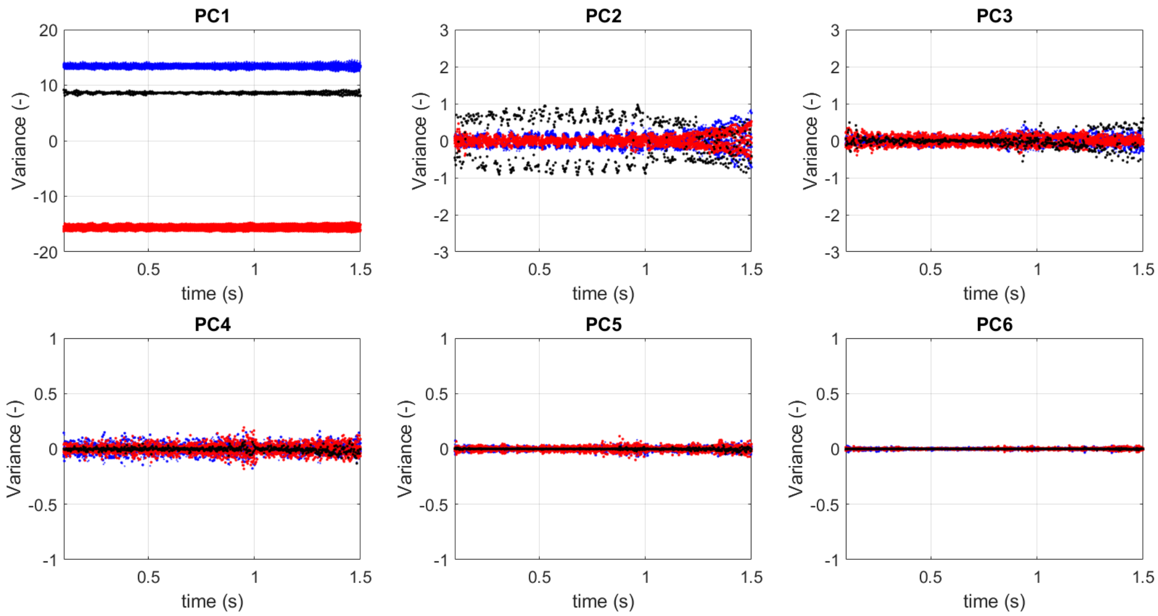

DMG3, T=-15°C, D90%, S02

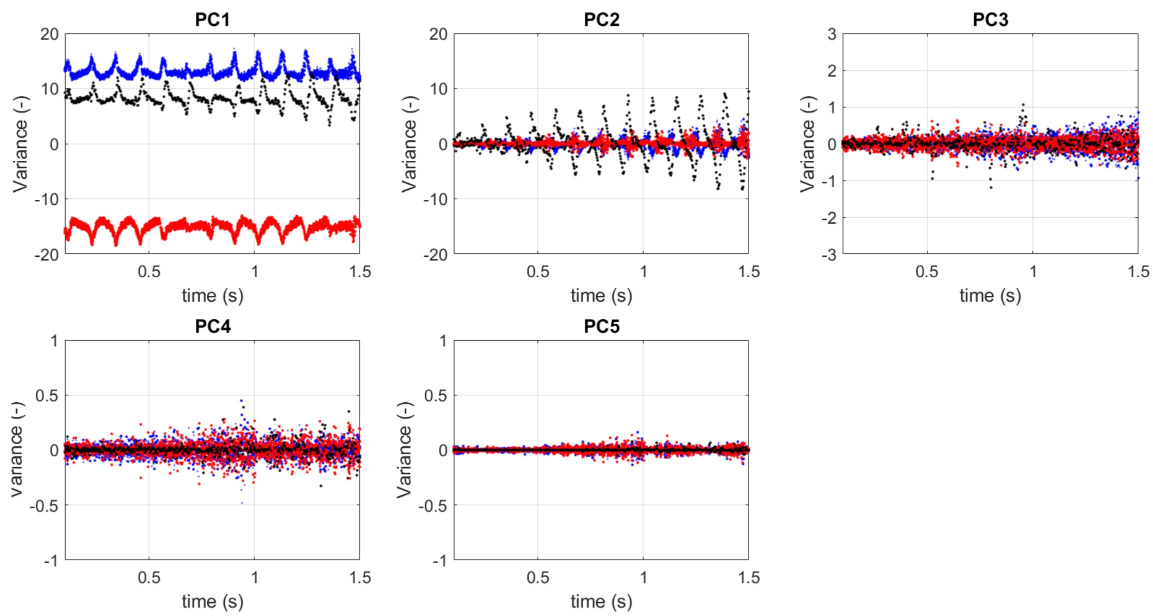

DMG3, T=-15°C, D90%, S03

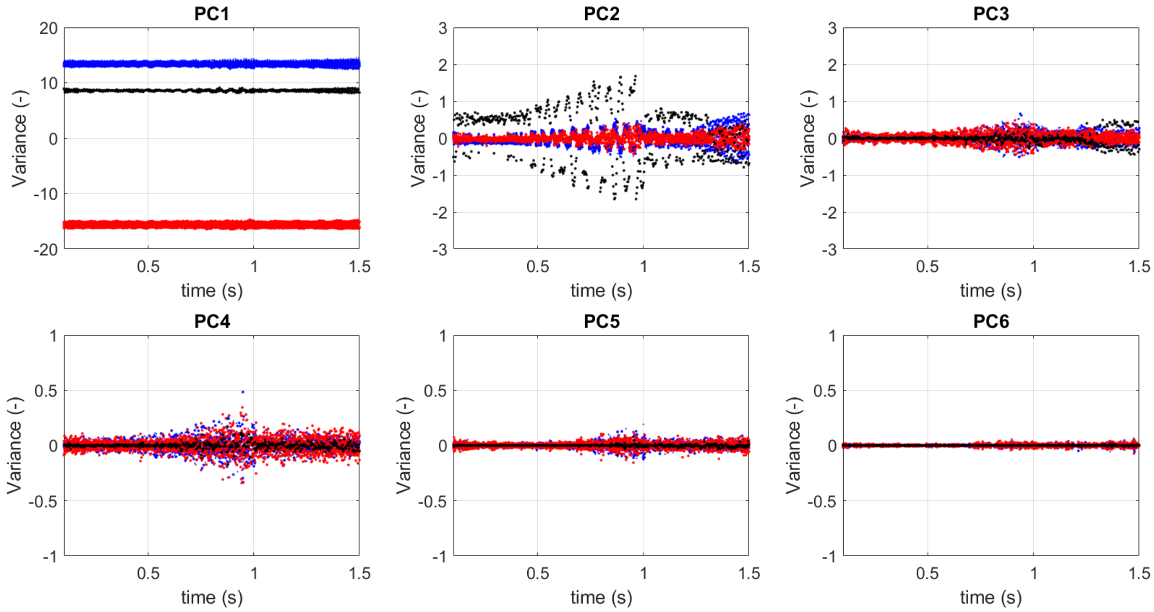

DMG3, T=-15°C, D90%, S04

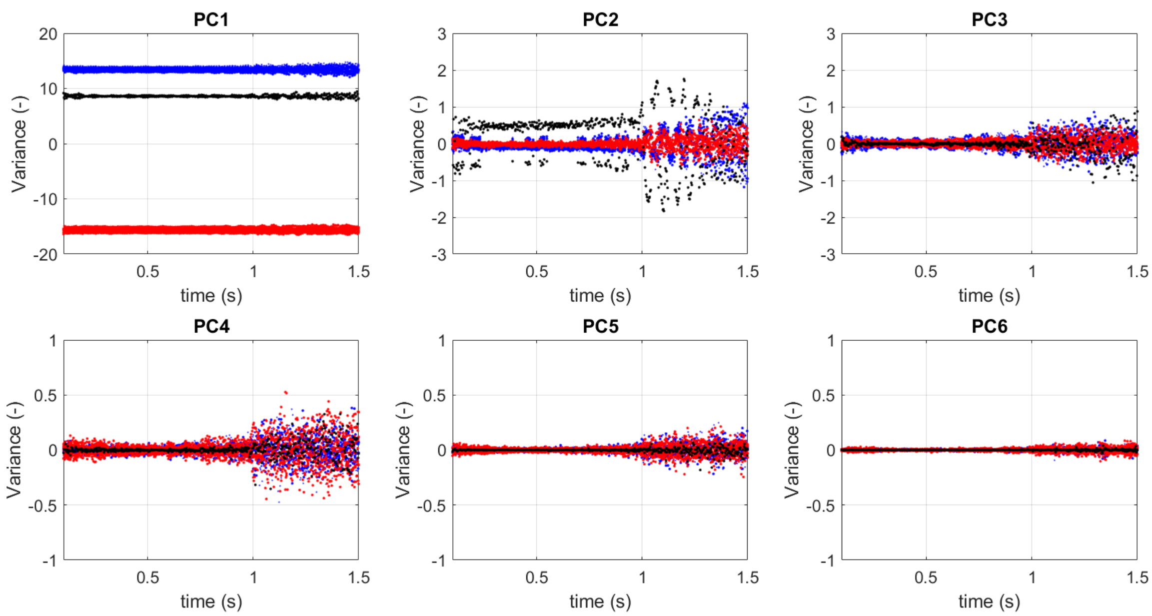

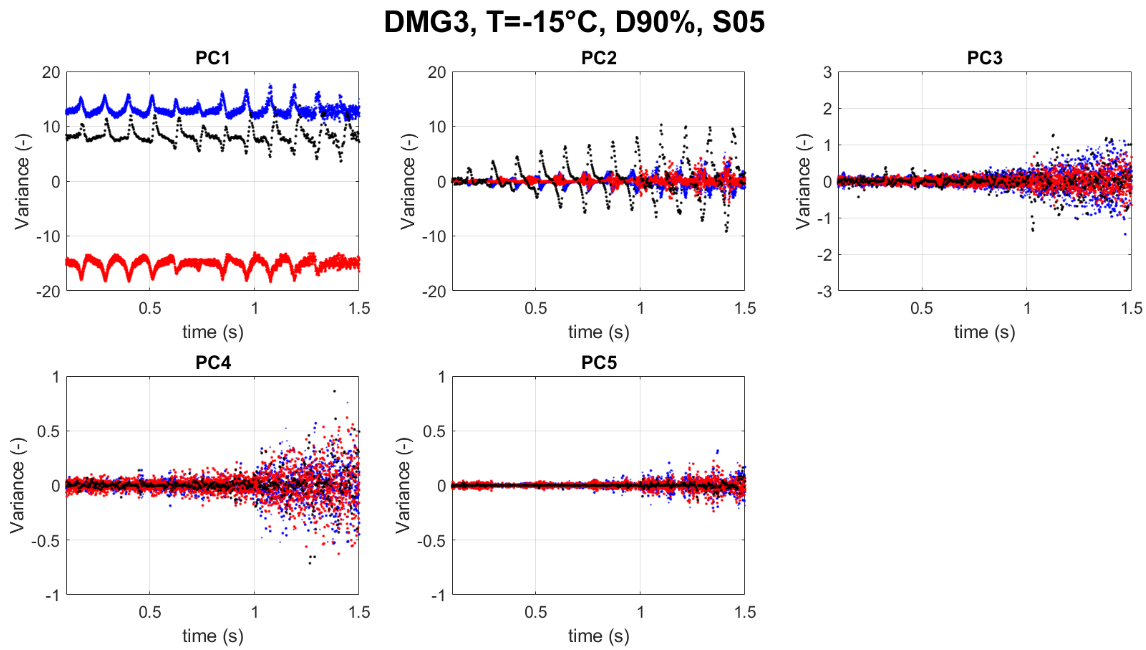
DMG3, T=-15°C, D90%, S05
PC1
PC2
PC3
PC4
PC5
Variance (-)
time (s)

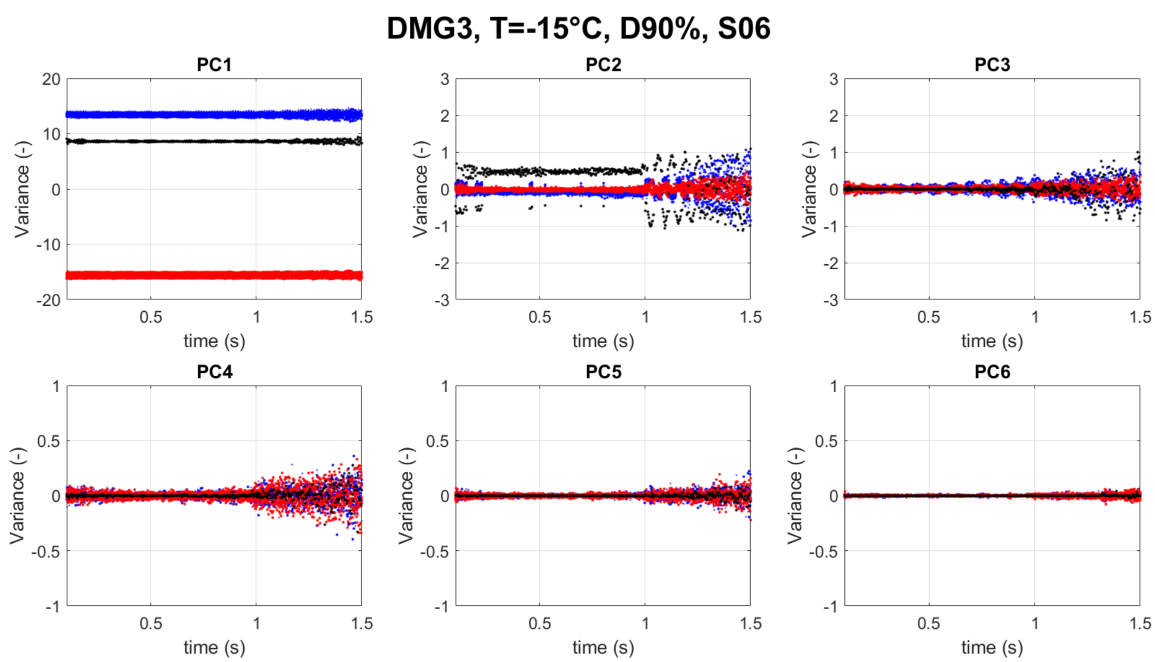
DMG3, T=-15°C, D90%, S06
PC1
PC2
PC3
PC4
PC5
PC6
Variance (-)
time (s)

Appendix D

UND, T=-15°C, D0%, S01

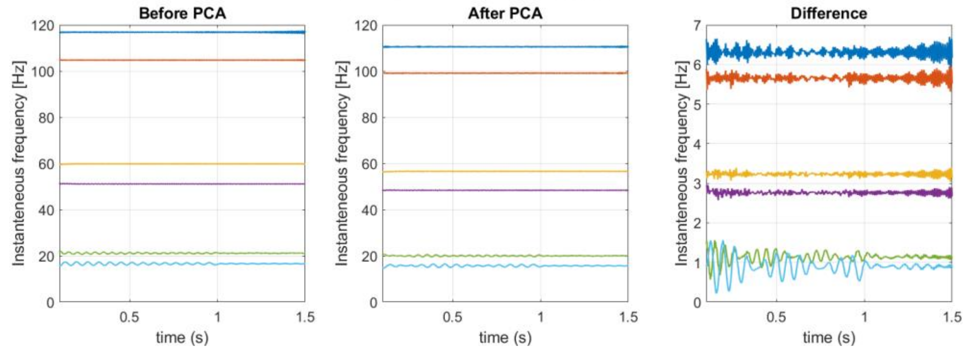

UND, T=-15°C, D0%, S02

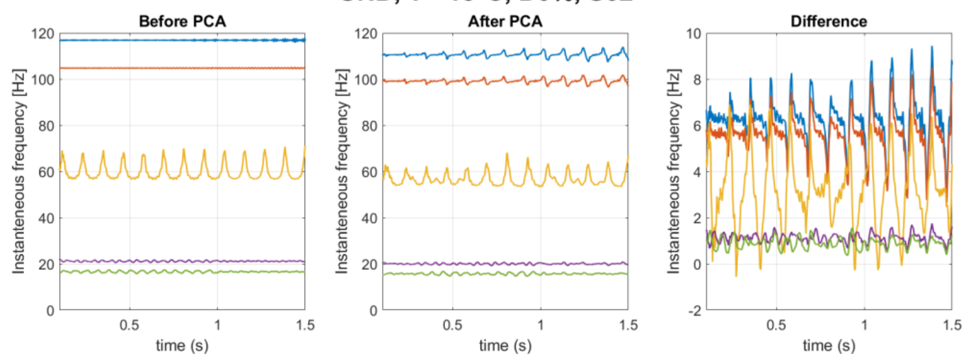

UND, T=-15°C, D0%, S03

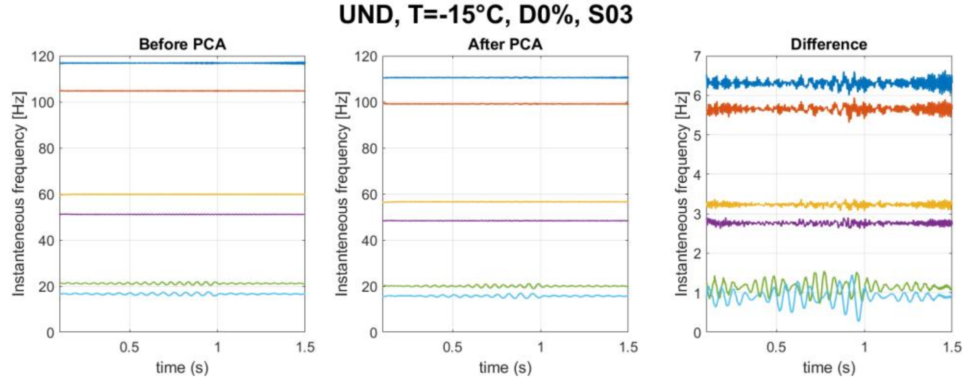

UND, T=-15°C, D0%, S04

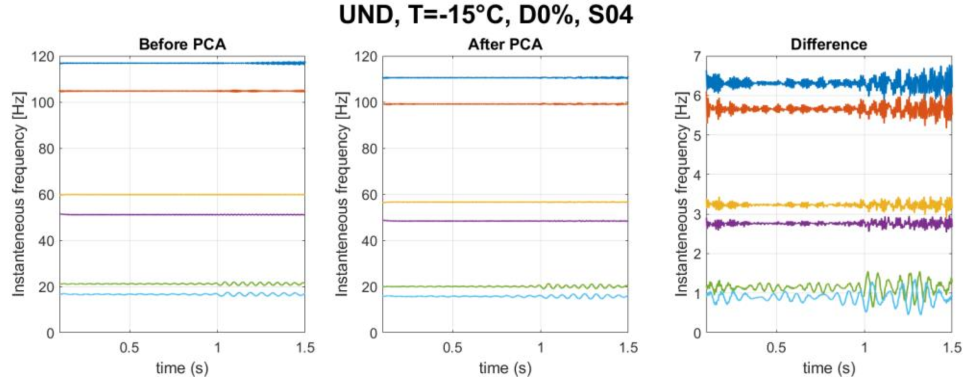

UND, T=-15°C, D0%, S05

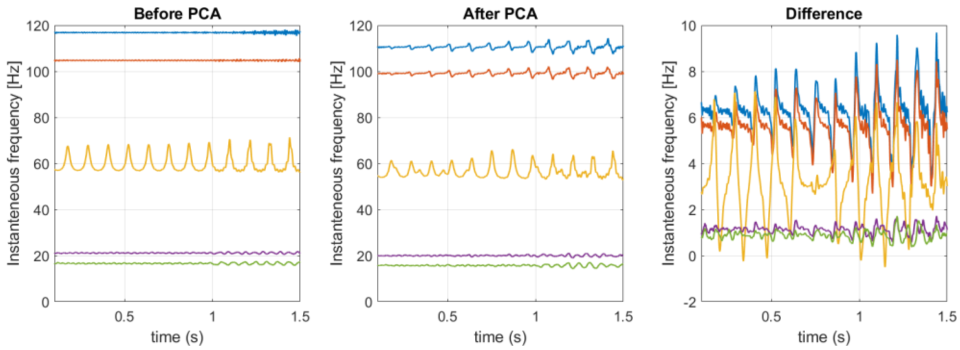

UND, T=-15°C, D0%, S06

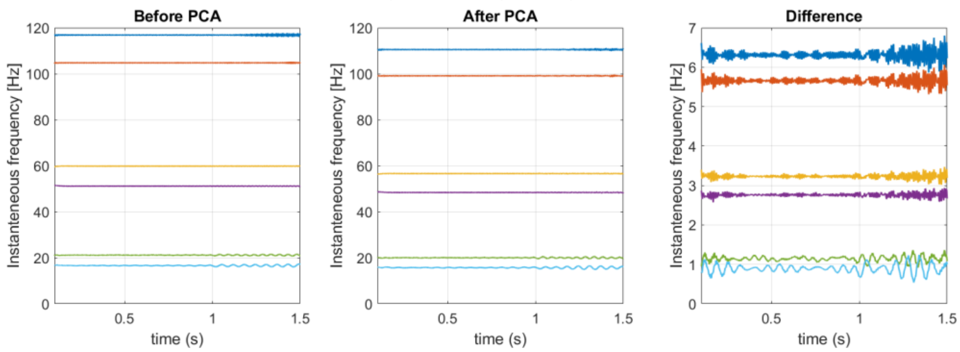

UND, T=20°C, D0%, S01

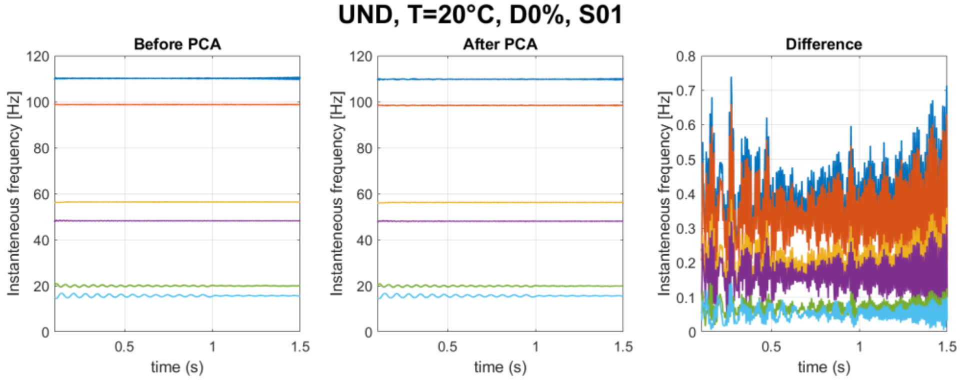

UND, T=20°C, D0%, S02

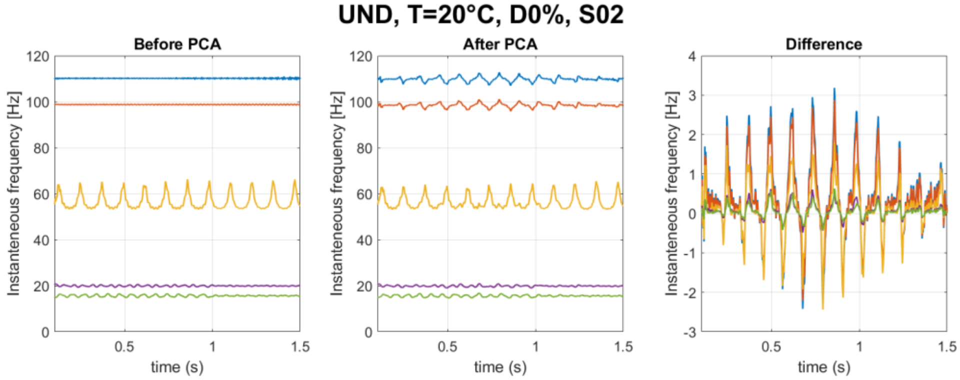

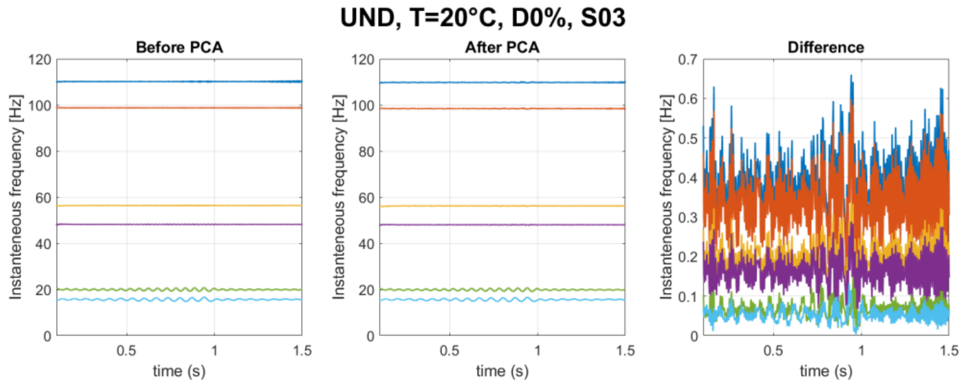
UND, T=20°C, D0%, S03
Before PCA
After PCA
Difference
Instanteneous frequency [Hz]
time (s)

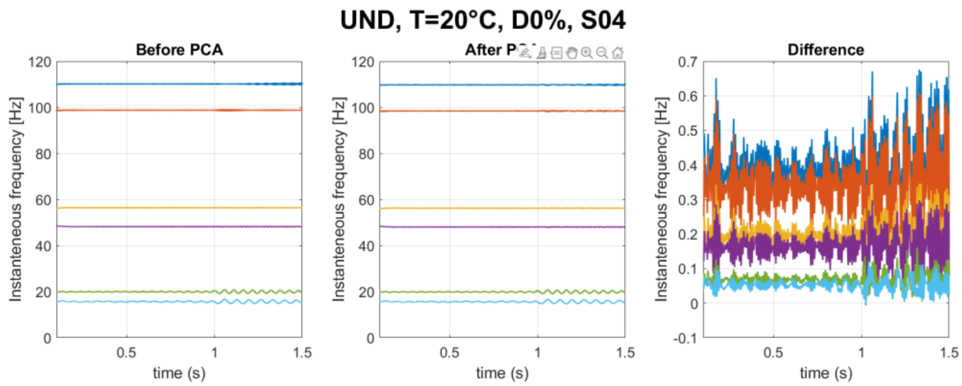
UND, T=20°C, D0%, S04
Before PCA
Difference
Instanteneous frequency [Hz]
time (s)

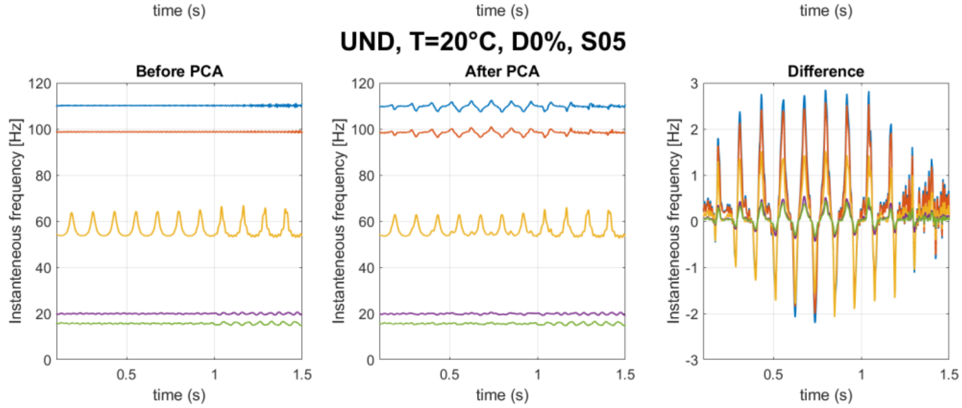
UND, T=20°C, D0%, S05
Before PCA
After PCA
Difference
Instanteneous frequency [Hz]
time (s)

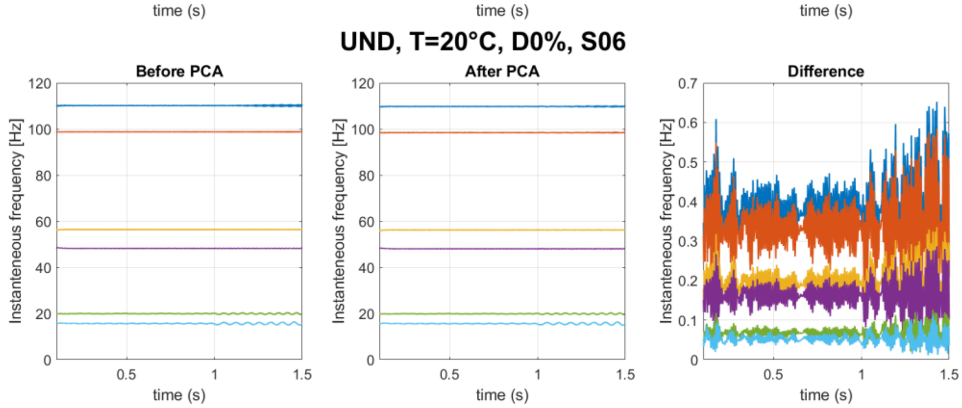
UND, T=20°C, D0%, S06
Before PCA
After PCA
Difference
Instanteneous frequency [Hz]
time (s)

DMG3, T=20°C, D90%, S01

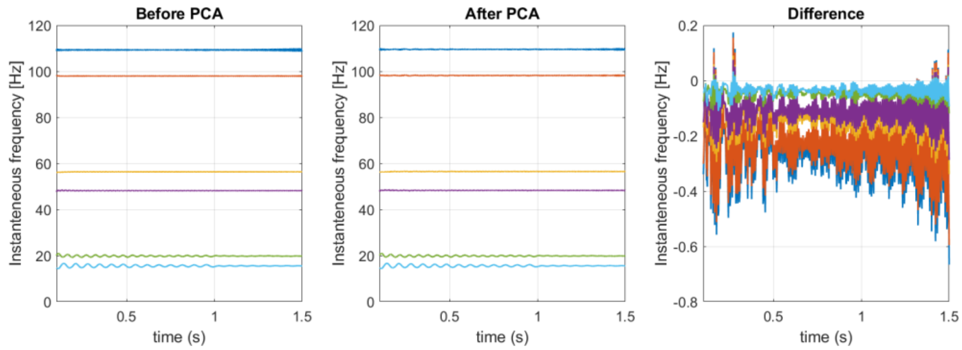

DMG3, T=20°C, D90%, S02

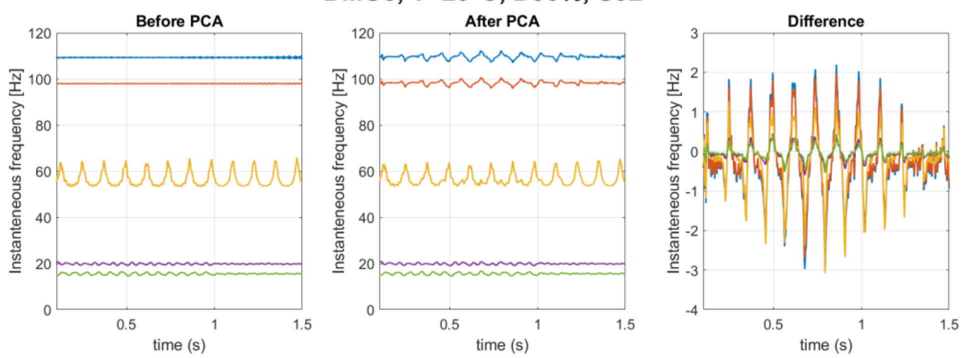

DMG3, T=20°C, D90%, S03

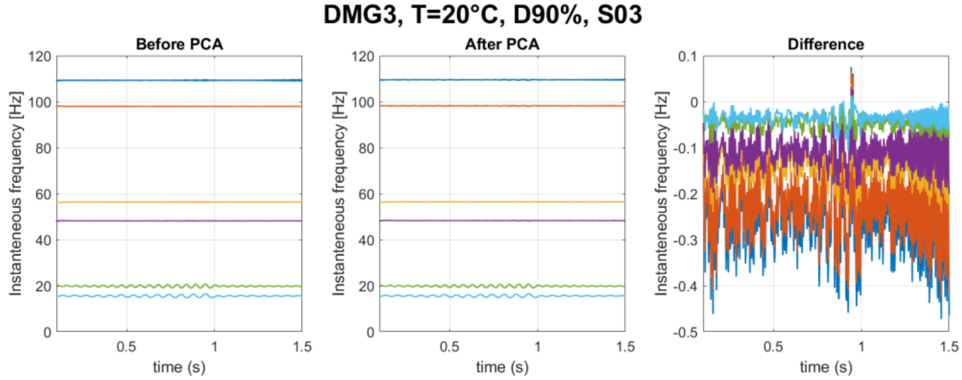

DMG3, T=20°C, D90%, S04

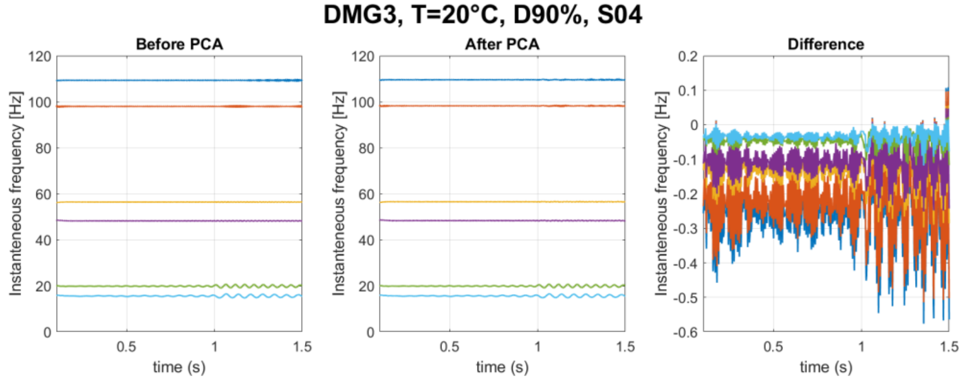

DMG3, T=20°C, D90%, S05

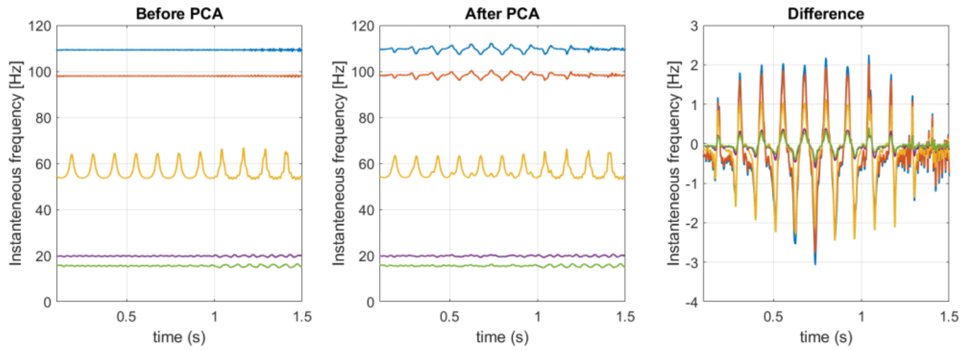

DMG3, T=20°C, D90%, S06

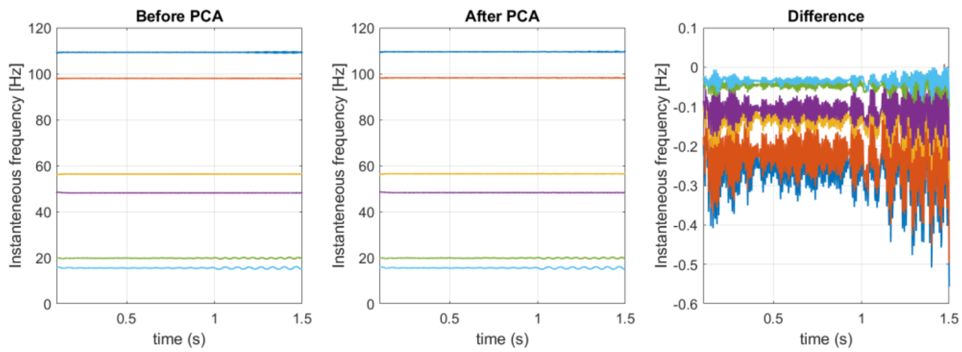

DMG3, T=-15°C, D90%, S01

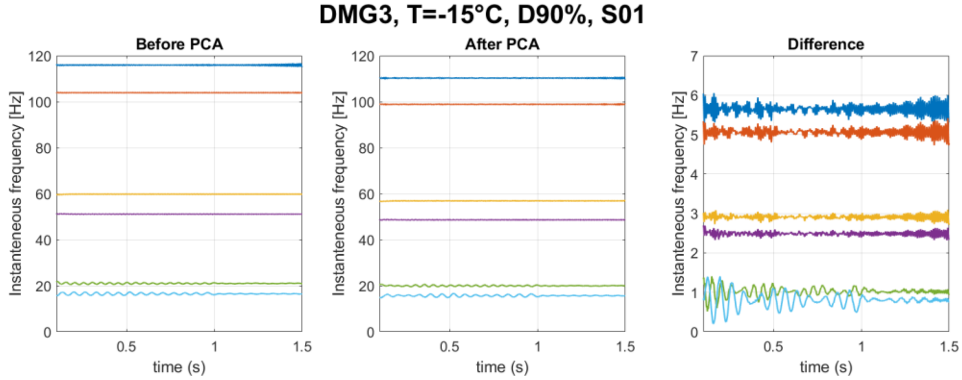

DMG3, T=-15°C, D90%, S02

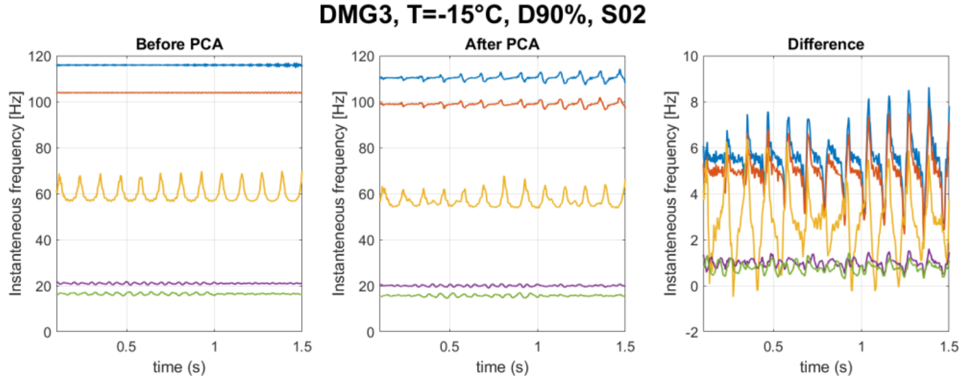

DMG3, T=-15°C, D90%, S03

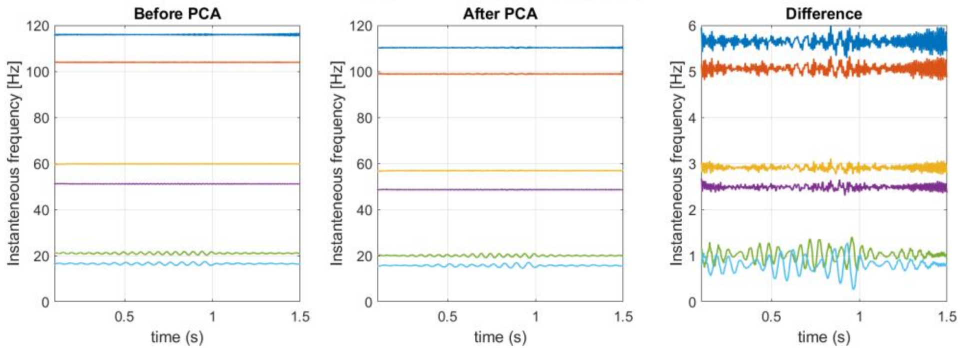

DMG3, T=-15°C, D90%, S04

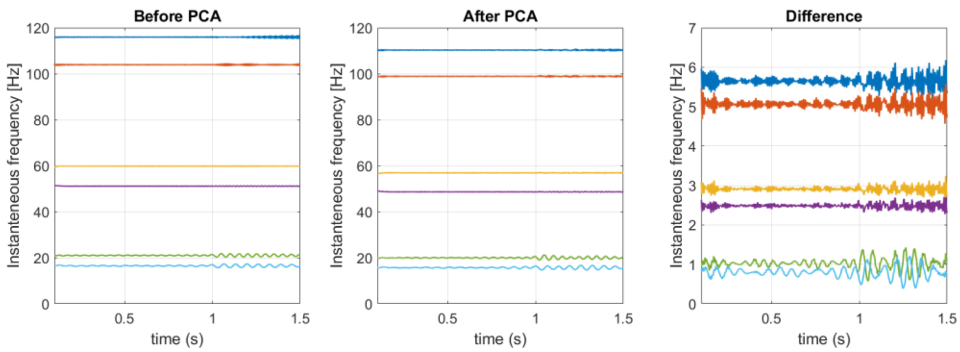

DMG3, T=-15°C, D90%, S05

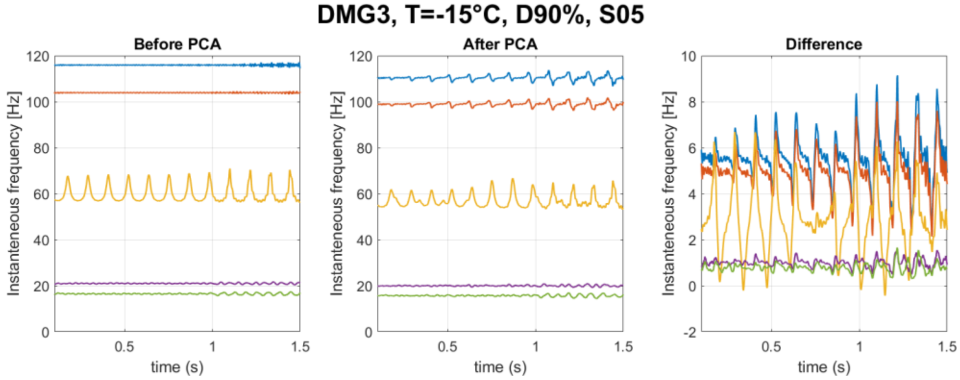

DMG3, T=-15°C, D90%, S06

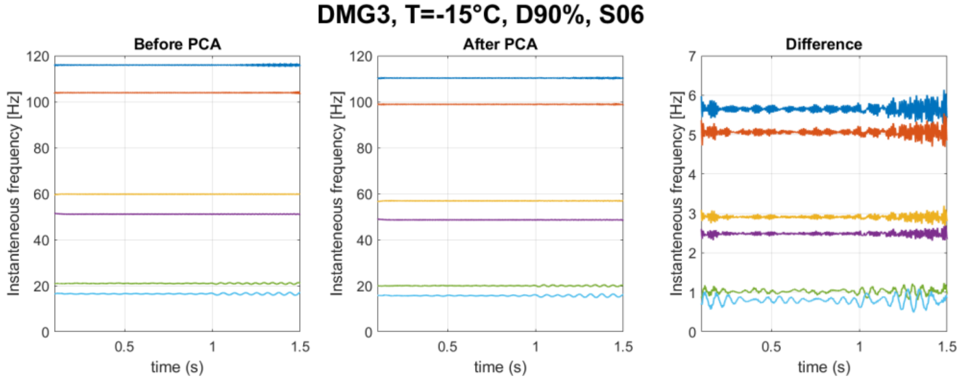

Appendix E

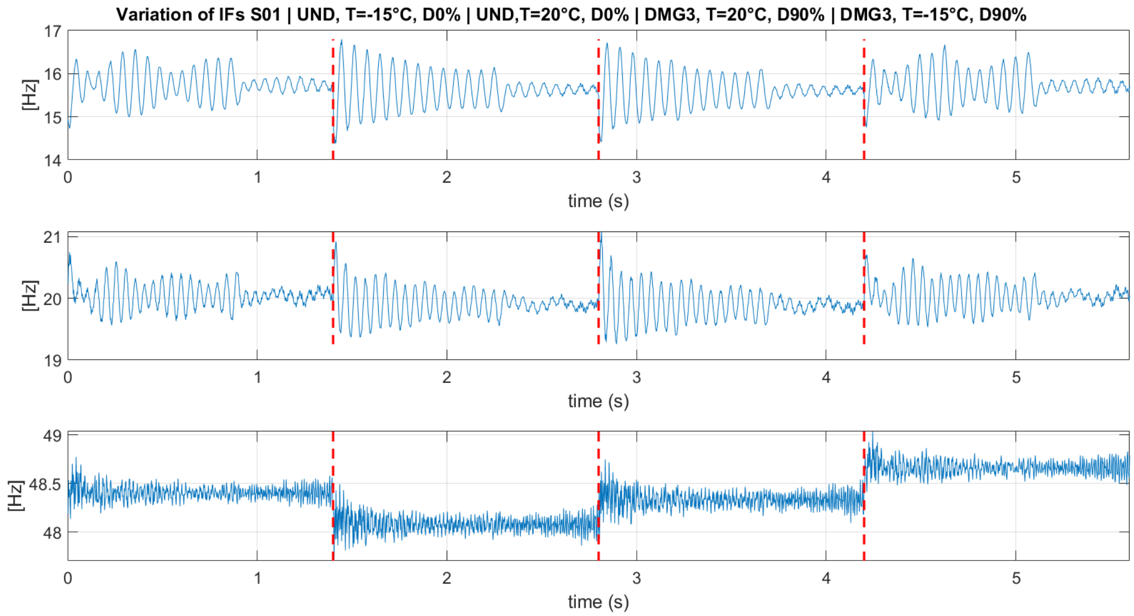

Variation of IFs S01 | UND, T=-15°C, D0% | UND,T=20°C, D0% | DMG3, T=20°C, D90% | DMG3, T=-15°C, D90%
[Hz]
time (s)

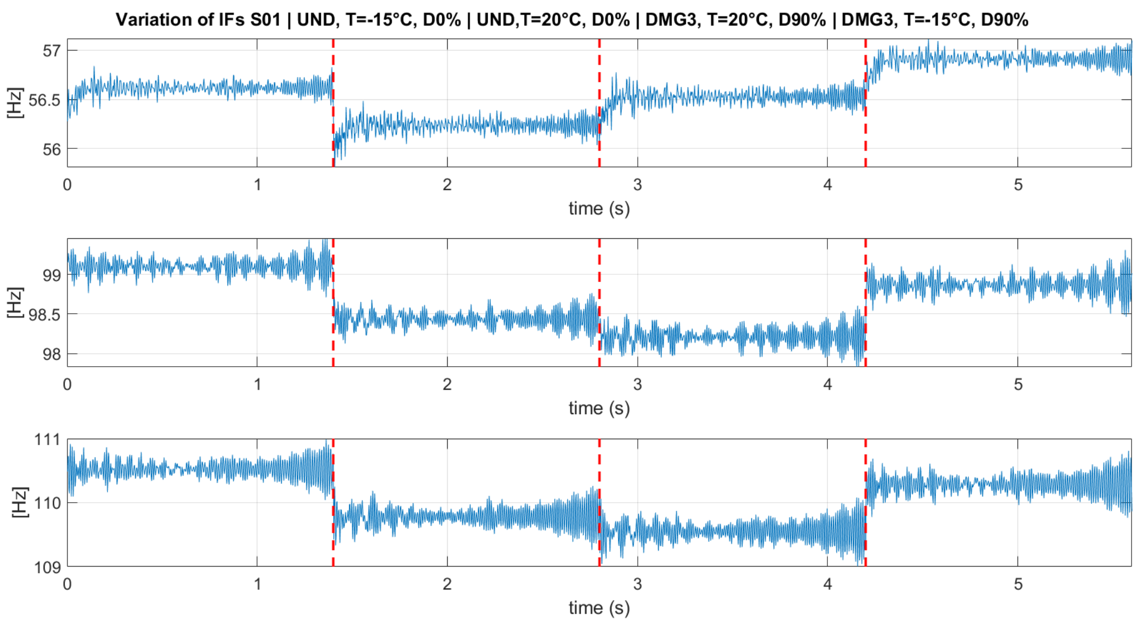

Variation of IFs S01 | UND, T=-15°C, D0% | UND,T=20°C, D0% | DMG3, T=20°C, D90% | DMG3, T=-15°C, D90%
[Hz]
time (s)

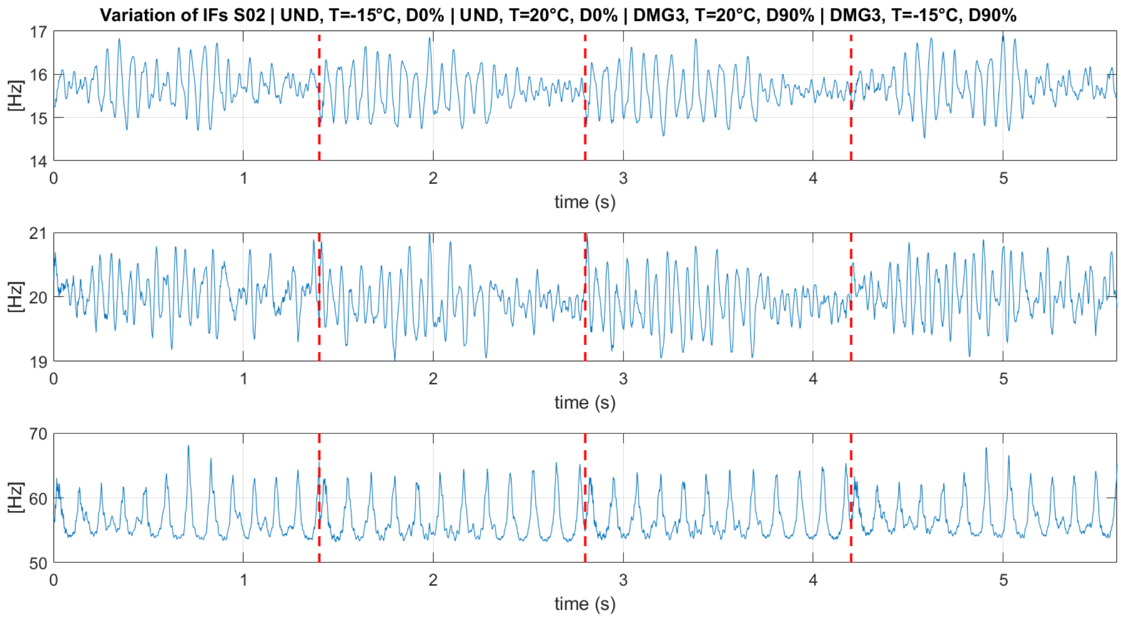
Variation of IFs S02 | UND, T=-15°C, D0% | UND, T=20°C, D0% | DMG3, T=20°C, D90% | DMG3, T=-15°C, D90%
[Hz]
time (s)

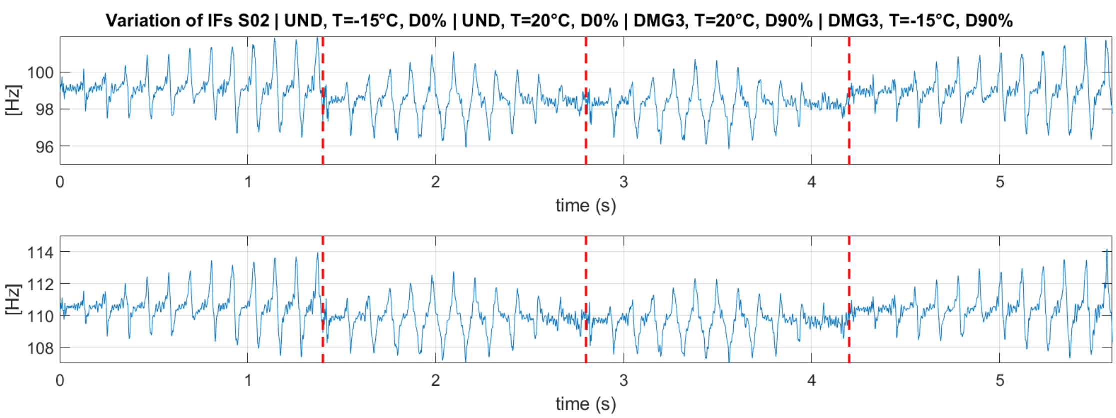
Variation of IFs S02 | UND, T=-15°C, D0% | UND, T=20°C, D0% | DMG3, T=20°C, D90% | DMG3, T=-15°C, D90%
[Hz]
time (s)

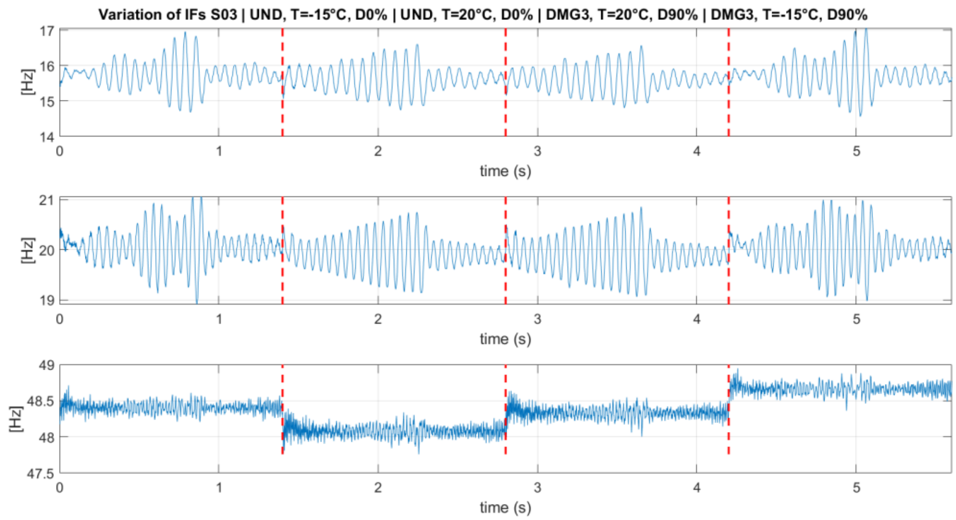
Variation of IFs S03 | UND, T=-15°C, D0% | UND, T=20°C, D0% | DMG3, T=20°C, D90% | DMG3, T=-15°C, D90%
[Hz]
time (s)
[Hz]
time (s)
[Hz]
time (s)

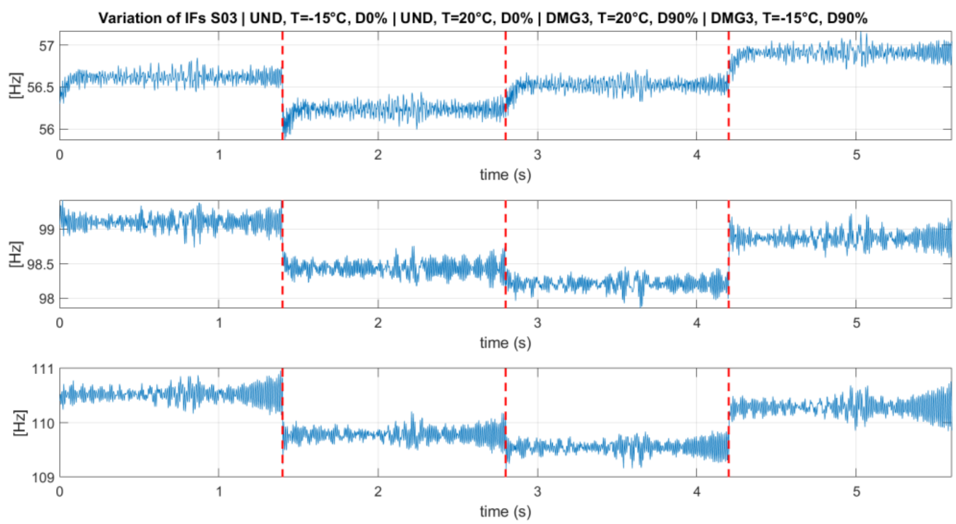
Variation of IFs S03 | UND, T=-15°C, D0% | UND, T=20°C, D0% | DMG3, T=20°C, D90% | DMG3, T=-15°C, D90%
[Hz]
time (s)
[Hz]
time (s)
[Hz]
time (s)

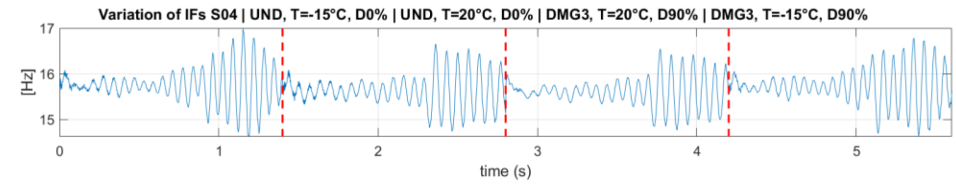

Variation of IFs S04 | UND, T=-15°C, D0% | UND, T=20°C, D0% | DMG3, T=20°C, D90% | DMG3, T=-15°C, D90%
[Hz]
time (s)

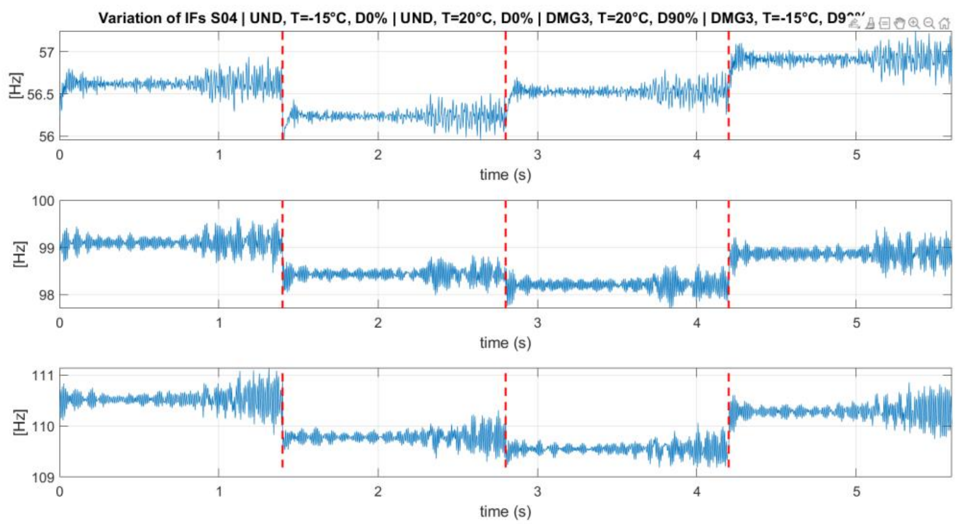

Variation of IFs S04 | UND, T=-15°C, D0% | UND, T=20°C, D0% | DMG3, T=20°C, D90% | DMG3, T=-15°C, D9
[Hz]
time (s)

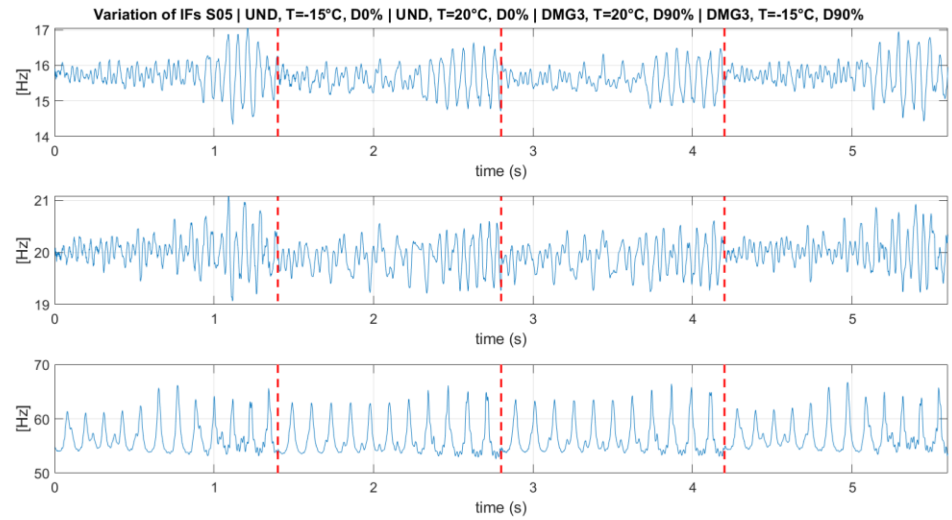
Variation of IFs S05 | UND, T=-15°C, D0% | UND, T=20°C, D0% | DMG3, T=20°C, D90% | DMG3, T=-15°C, D90%
[Hz]
time (s)

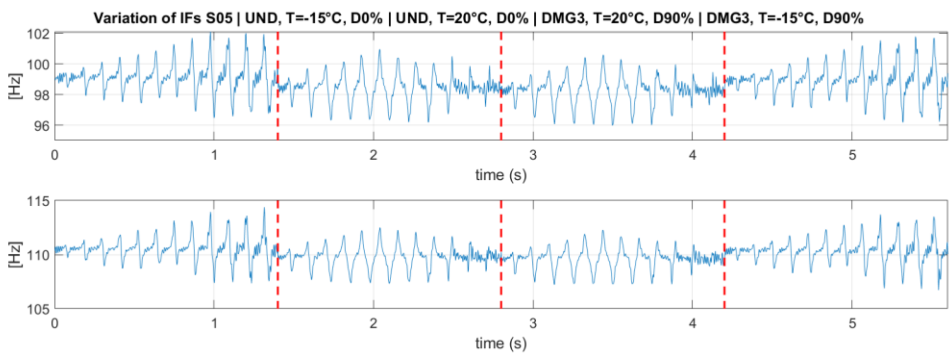
Variation of IFs S05 | UND, T=-15°C, D0% | UND, T=20°C, D0% | DMG3, T=20°C, D90% | DMG3, T=-15°C, D90%
[Hz]
time (s)

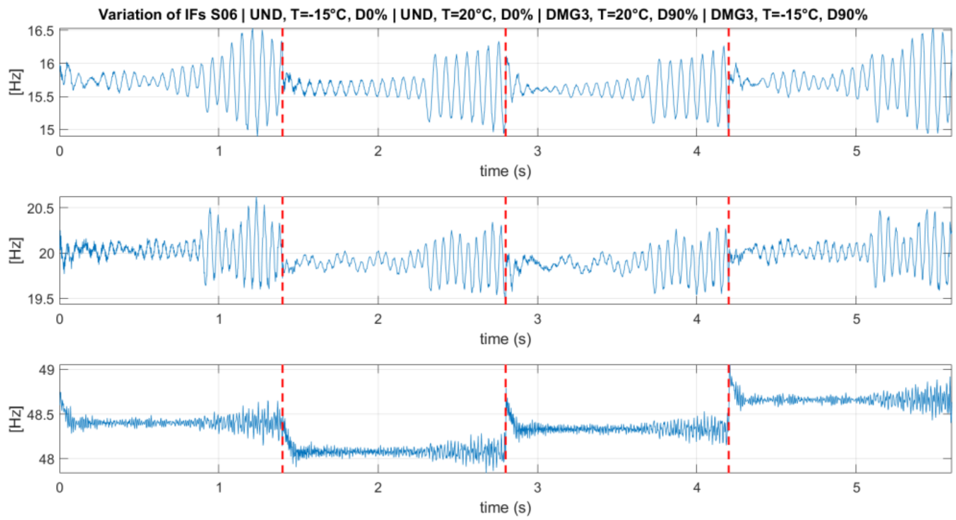
Variation of IFs S06 | UND, T=-15°C, D0% | UND, T=20°C, D0% | DMG3, T=20°C, D90% | DMG3, T=-15°C, D90%
[Hz]
time (s)

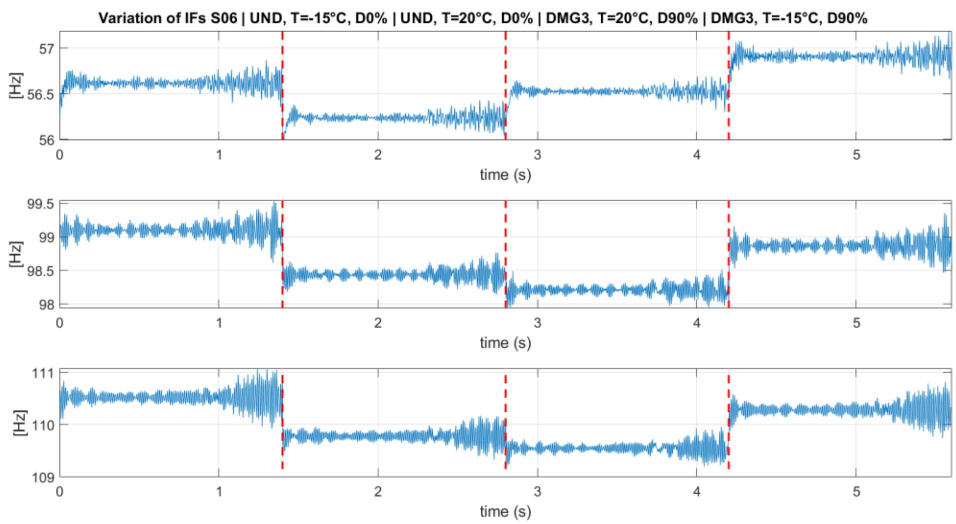
Variation of IFs S06 | UND, T=-15°C, D0% | UND, T=20°C, D0% | DMG3, T=20°C, D90% | DMG3, T=-15°C, D90%
[Hz]
time (s)